

Universidade Federal de Juiz de Fora
Instituto de Ciências Exatas
Programa de Pós-Graduação em Modelagem Computacional

Andrés Julián Castrillón Vásquez

The traveling wavefront for foam flow in multilayered porous media

Juiz de Fora

2023

Andrés Julián Castrillón Vásquez

The traveling wavefront for foam flow in multilayered porous media

Tese apresentada ao Programa de Pós-Graduação em Modelagem Computacional da Universidade Federal de Juiz de Fora como requisito parcial para obtenção do grau de Doutor em Modelagem Computacional.

Orientador: Grigori Chapiro

Coorientador: Luis F. Lozano Guerrero

Juiz de Fora

2023

Ficha catalográfica elaborada através do programa de geração automática da Biblioteca Universitária da UFJF, com os dados fornecidos pelo(a) autor(a)

Castrillón Vásquez, Andrés Julián.

The traveling wavefront for foam flow in multilayered porous media / Andrés Julián Castrillón Vásquez. -- .
106 f.

Orientador: Grigori Chapiro

Coorientador: Luis Fernando Lozano Guerrero

Tese (doutorado) - Universidade Federal de Juiz de Fora, Instituto de Ciências Exatas. Programa de Pós-Graduação em Modelagem Computacional, .

1. Porous media. 2. Traveling waves. 3. Riemann problem. 4. Multilayer. 5. Crossflow. I. Chapiro, Grigori, orient. II. Lozano Guerrero, Luis Fernando, coorient. III. Título.

Andrés Julián Castrillón Vásquez

The traveling wavefront for foam flow in multilayered porous media

Tese apresentada
ao Programa de Pós-
Graduação em
Modelagem
Computacional
da Universidade Federal
de Juiz de Fora como
requisito parcial à
obtenção do título de
Doutor em Modelagem
Computacional. Área de
concentração: Modelagem
Computacional.

Aprovada em 24 de novembro de 2023.

BANCA EXAMINADORA

Prof. Dr. Grigori Chapiro - Orientador

Universidade Federal de Juiz de Fora

Prof. Dr. Luis Fernando Lozano Guerrero - Coorientador

Universidade Federal de Juiz de Fora

Prof. Dr. Aparecido Jesuino de Souza

Universidade Federal da Paraíba

Prof. Dr. Juan Carlos Muñoz Grajales

Universidad del Valle, Colômbia

Prof. Dr. Rodrigo Weber dos Santos

Universidade Federal de Juiz de Fora

Prof.Dr. Pavel Zenon Sejas Paz
Universidade Federal de Juiz de Fora

Juiz de Fora, 20/11/2023.



Documento assinado eletronicamente por **Grigori Chapiro, Professor(a)**, em 24/11/2023, às 15:46, conforme horário oficial de Brasília, com fundamento no § 3º do art. 4º do [Decreto nº 10.543, de 13 de novembro de 2020](#).



Documento assinado eletronicamente por **Juan Carlos Muñoz Grajales, Usuário Externo**, em 24/11/2023, às 15:46, conforme horário oficial de Brasília, com fundamento no § 3º do art. 4º do [Decreto nº 10.543, de 13 de novembro de 2020](#).



Documento assinado eletronicamente por **LUIS FERNANDO LOZANO GUERRERO, Usuário Externo**, em 24/11/2023, às 15:47, conforme horário oficial de Brasília, com fundamento no § 3º do art. 4º do [Decreto nº 10.543, de 13 de novembro de 2020](#).



Documento assinado eletronicamente por **Rodrigo Weber dos Santos, Professor(a)**, em 24/11/2023, às 15:47, conforme horário oficial de Brasília, com fundamento no § 3º do art. 4º do [Decreto nº 10.543, de 13 de novembro de 2020](#).



Documento assinado eletronicamente por **Aparecido Jesuino de Souza, Usuário Externo**, em 24/11/2023, às 15:48, conforme horário oficial de Brasília, com fundamento no § 3º do art. 4º do [Decreto nº 10.543, de 13 de novembro de 2020](#).



Documento assinado eletronicamente por **Pavel Zenon Sejas Paz, Usuário Externo**, em 24/11/2023, às 15:49, conforme horário oficial de Brasília, com fundamento no § 3º do art. 4º do [Decreto nº 10.543, de 13 de novembro de 2020](#).



A autenticidade deste documento pode ser conferida no Portal do SEI-Ufjf (www2.ufjf.br/SEI) através do ícone Conferência de Documentos, informando o código verificador **1585188** e o código CRC **34C00D95**.

Dedico este trabajo a mis amadas Alejandra, Martina y mi madre, que está conmigo espiritualmente.

ACKNOWLEDGMENTS

I extend my deepest gratitude to my family, with special recognition to my mother for her unwavering support. I am profoundly thankful to my wife, Alejandra, for choosing me as her life partner and for being my unwavering source of strength. My beautiful daughter, Martina, is my constant motivation, instilling in me the desire to be a better person each day.

To my advisor, Grigori Chapiro, I express my heartfelt thanks for fearlessly taking on this challenging project and immersing me in the world of applied mathematics, sharing his knowledge, and demonstrating exceptional patience. To my co-advisor, Luis Fernando Lozano Guerrero, I owe my gratitude for his trust, for imparting his techniques, and for being my mathematical anchor. Pavel Zenon Sejas Paz, your motivation, clarity in explanations, and unwavering collaboration are deeply appreciated.

To Jhuan Cedro, I am thankful for sharing your knowledge in computational techniques, especially when everything seemed perplexing. To Wesley Pereira, thank you for your support at the beginning of this dream. To my colleague, Jan Pierre Agenciano da Silva Rocha, for our insightful discussions on programming techniques.

Professors Iury Higor Aguiar da Igreja and Bernardo Martins Rocha, I am grateful for your clarity in classroom teaching and your conceptual guidance throughout the research process.

To Professor Flávia de Souza Bastos, I thank you for being there during the most challenging moments.

To all the other professors who contributed their expertise and knowledge to my professional growth, and to my colleagues in the Applied Mathematics Laboratory, you have formed an extraordinary team, demonstrating remarkable strength in every aspect we have tackled.

I thank FAPEMIG and SHELL Brasil LTDA, without financial support, without which this work would not be possible.

This work was carried out in association with the P&D project registered as ANP 23518-4, “Advancing mathematical and computational modeling to support the implementation of “Foam-assisted WAG” technology in pre-salt reservoirs” (Federal University of Juiz de Fora - UFJF / Shell Brasil / ANP), supported by Shell Brasil under ANP P&D as a “Commitment to Invest in Research and Development”.

“We can only see a short distance ahead, but we can see plenty there
that needs to be done”.

Alan Turing.

ABSTRACT

This work proposes the study of a system of partial differential equations (mass balance and foam transport) describing the phenomenon of foam transport in stratified porous media. The problem is approached in one-dimensional and two-dimensional forms. We use the linear kinetic model and a simplified version of the bubble population equilibrium model to investigate foam transport in both cases.

First, we study foam flow in a two-layer system using the linear kinetic model. The mass exchange between layers is estimated from numerical and analytical results. By varying both the absolute permeability and porosity of the medium in both layers, we explore how mass exchange between the layers changes, marking the first analytical study of the crossflow phenomenon in the foam injection process.

The existence of a significant problem of “viscous fingering” and preferential pathways is well-known in various applications of foam in fractured media. Specifically, due to the high permeability of the fracture, when gas is injected, it tends to move much faster through the fracture, affecting the uniform sweep of the medium. It is known that foam injection helps reduce gas mobility, thereby improving sweep uniformity. In this work, we address this issue in fractured media. To do so, we implement an n-layer model, allowing us to study traveling wave solutions in fractured media, treating it as a medium with three layers, where the fracture is identified as the intermediate layer with higher permeability and thinner thickness.

Keywords: Layered Porous Media · Traveling Wave · Riemann Problem

RESUMO

Este trabalho propõe o estudo de um sistema de equações diferenciais parciais (balanço de massa e transporte de espuma) que descreve o fenômeno de transporte de espuma em meios porosos estratificados. O problema é abordado em formas unidimensionais e bidimensionais. Utilizamos o modelo cinético linear e uma versão simplificada do modelo de equilíbrio de população de bolhas para investigar o transporte de espuma em ambos os casos.

Primeiro, estudamos o fluxo de espuma em um sistema de duas camadas usando o modelo cinético linear. A troca de massa entre as camadas é estimada a partir de resultados numéricos e analíticos. Variando tanto a permeabilidade absoluta quanto a porosidade do meio em ambas as camadas, exploramos como a troca de massa entre as camadas muda, marcando o primeiro estudo analítico do fenômeno de fluxo cruzado no processo de injeção de espuma.

É conhecida a existência de um problema significativo de “viscous fingering” e de caminhos preferenciais em várias aplicações de espuma em meios fraturados. Especificamente, devido à alta permeabilidade da fratura, quando gás é injetado, ele tende a se mover muito mais rapidamente pela fratura, afetando a varredura uniforme do meio. Sabe-se que a injeção de espuma ajuda a reduzir a mobilidade do gás, melhorando assim a uniformidade da varredura. Neste trabalho, abordamos esse problema em meios fraturados. Para fazer isso, implementamos um modelo de n camadas, o que nos permite estudar soluções de ondas viajantes em meios fraturados, tratando-o como um meio com três camadas, onde a fratura é identificada como a camada intermediária com maior permeabilidade e menor espessura.

Palavras-chave: Meios porosos em camadas · Ondas Viajantes · Problema de Riemann

LIST OF FIGURES

Figure 1 – Gas injection vs. foam injection in a reservoir. Taken from [20]	18
Figure 2 – Layered or fractured media schemes. Taken from [33].	19
Figure 3 – Schematic representation of the domain $\Omega := (0, L) \times (-d, d)$ composed of two layers with permeabilities k_i	31
Figure 4 – Schematic representation of water saturation S_w along the vertical cross section of the two layer porous medium.	33
Figure 5 – Stable traveling water saturation profile obtained through two-dimensional numerical simulations at 3000s (upper plot), 4000s (middle plot) and at 5000s (lower plot).	37
Figure 6 – Stable traveling foam texture profile obtained through two-dimensional numerical simulations at 3000s (upper plot), 4000s (middle plot) and at 5000s (lower plot).	38
Figure 7 – Average cross-section water saturation profile inside the wave front obtained numerically for $t = 5000s$	38
Figure 8 – Moving average of the velocities v_1 (left) and v_2 (right) of the two-dimensional model compared to the analytically estimated v from (4.40).	39
Figure 9 – The Standard Deviation $SD(v_1)$ and $SD(v_2)$ of the moving average of velocities v_1 and v_2 in two-dimensional simulation.	39
Figure 10 – Moving average of the velocities v_1 (left) and v_2 (right) of the one-dimensional model compared to the analytically estimated v from (4.40).	40
Figure 11 – The standard deviation $SD(v_1)$ and $SD(v_2)$ of the average velocities v_1 and v_2 from one-dimensional simulations.	40
Figure 12 – Water saturation S_w and foam texture n_D profiles in the first layer, in the one-dimensional and two-dimensional models, at cross section $z = -2.5mm$. The dashed curves represent the behavior at time $t = 4000s$ and the continuous curves for $t = 5000s$	41
Figure 13 – Water saturation S_w and foam texture n_D profiles in the second layer, in the one-dimensional and two-dimensional models, at cross section $z = 2.5mm$. The dashed curves represent the behavior at time $t = 4000s$ and the continuous curves for $t = 5000s$	42
Figure 14 – Numerical domain for the two-dimensional simulation using FOSSIL.	43
Figure 15 – Example of front tracking vectors x_1^{front} and x_2^{front}	43
Figure 16 – Schematic representation of a three-layered porous medium as a domain $\Omega := (0, L) \times (-d, d_3)$; where, k_i is the permeabilities of the layer i , respectively.	48
Figure 17 – Numerical domain for the three-layer problem.	51

Figure 18 – Stable traveling water saturation profile obtained through two-dimensional numerical simulations at 2500 s (upper plot), 3750 s (middle plot) and 5000 s (lower plot).	51
Figure 19 – Position on the horizontal axis of the water saturation front x_i^{front} in each of the i -layers.	52
Figure 20 – Velocities v_i in the layer i ; and standard deviation of each velocity $SD(v_i)$ in the layer i . Simulated using the moving average for groups of 240 data in the 2D-model.	52
Figure 21 – Comparison of the profiles using the calculated velocity $v = 6.8e \times 10^{-5}m/s$. The dotted curves are generated by FOSSIL at times $t_0 = 2500s$, $t_1 = 3000s$, $t_2 = 3500s$, $t_3 = 4000s$, and $t_4 = 4500s$. S_{w_0} is the profile generated by FOSSIL at time 2500s. (a) In layer 1, (b) layer 2 and (c) layer 3. The distance between $S_{w_0} + v\Delta t$ and $S_w(t)$ are shown in Table 3.	53
Figure 22 – Schematic representation of a n-layered porous media.	57
Figure 23 – Schematic representation of a three-layered porous medium as a rectangular domain Ω ; where, $c \in (0, 1)$ is constant, and k_i is the permeability of the layer i	63
Figure 24 – Schematic representation of the water saturation S_w along the vertical cross-section of the three-layered porous medium, where $c \in (0, 1)$ is constant. The dotted red curve represents the cross-section of S_w calculated at $t = 5000 s$ in the 2D simulations. The continuous black curve S_w is a quadratic approximation, symmetric with respect to the line $z = 0$. Coefficients R_i represent the total mass variation in each layer i , S_{w_L} is the saturation value at the interface, and S_{w_i} is the average value in each region of the domain i with permeability k_i	64
Figure 25 – Stable traveling water saturation profile (symmetric case), obtained through two-dimensional numerical simulations at 6000 s (upper plot), 12000 s (middle plot), and at 18000 s (lower plot).	66
Figure 26 – Comparison of the water saturation profiles for the symmetric case. The dotted curves are obtained from FOSSIL simulations for times $t_0 = 2500s$, $t_1 = 3000s$, $t_2 = 3500s$, $t_3 = 4000s$, and $t_4 = 4500s$. Continuous curves represent the displacement of the water saturation profile at $t_0 = 2500s$ using the estimated velocity $v_F = 1.671 \times 10^{-4}m/s$	67
Figure 27 – Comparing velocities in the symmetric case. The theoretical velocity is estimated using Eq. (6.38).	68
Figure 28 – Simulations in the one-dimensional model (symmetric case) for $t = 12000 s$, $t = 16000 s$ and $t = 20000 s$, using the parameters of Table 4.	68

Figure 29 – Distance between the water saturation fronts S_{w_i} ($i = 1, 2, 3$), symbolized as Dis , for the symmetric case.	69
Figure 30 – Velocities simulated (symmetric case), using RCD and standard deviation of velocities, estimated using a moving average regularization for groups of 200 data.	69
Figure 31 – Schematic representation of the saturation of water S_w along the vertical cross-section of the porous medium of three layers, where $c \in (0, 1)$ is constant. The dotted red curve is the exact representation of S_w calculated at $t = 10000$ s in the two-dimensional simulations. The continuous blue curve S_w is an approximation with respect to z . Coefficients R_i represent the total mass variation in each layer i . The saturation value at the interface between layers 1 and 2 is $S_{w_L}^1$, and, $S_{w_L}^2$, between layers 2 and 3. S_{w_i} is the average value in each region of the domain i with permeability k_i	70
Figure 32 – Stable traveling water saturation profile (non-symmetric case), obtained through two-dimensional numerical simulations at 6000 s (upper plot), 12000 s (middle plot) and at 18000 s (lower plot).	72
Figure 33 – Comparison of the water saturation profiles for the symmetric case. The dotted curves are obtained from FOSSIL simulations for times $t_0 = 5000s$, $t_1 = 5500s$, $t_2 = 6000s$, $t_3 = 6500s$, and $t_4 = 7000s$. Continuous curves represent the displacement of the water saturation profile at $t_0 = 5000s$ using the estimated velocity $v_F = 1.723 \times 10^{-4}m/s$	72
Figure 34 – Comparing velocities in the non-symmetric case. The theoretical velocity is estimated using Eq. (6.38)	72
Figure 35 – Simulations in the one-dimensional model (non-symmetric case) for $t = 17000$ s, $t = 18000$ s and $t = 19000$ s, using the parameters of Table 4.	73
Figure 36 – Distance between the water saturation fronts S_{w_i} ($i = 1, 2, 3$), symbolized as Dis , for the non-symmetric case.	73
Figure 37 – Velocities simulated (non-symmetric case), using RCD and standard deviation of velocities, estimated using a moving average regularization for groups of 1200 data.	74
Figure 38 – Schematic representation of the two-layered communicating porous medium.	79
Figure 39 – The water saturation profile obtained simulating Eq. (4.1)-(7.4) for Case I: $\mathcal{K} < \mathcal{P}$ for three times: $t = 1000$ [s] (top), $t = 2000$ [s] (middle), and $t = 3000$ [s] (bottom).	82

Figure 40 – Vertical velocity field (left panel) and water saturation (right panel) around the traveling wave front at $t = 2000$ [s] for Case I: $\mathcal{K} < \mathcal{P}$. White arrows indicate the mass exchange between layers. The black dashed curve represents the approximate front position.	83
Figure 41 – The water saturation profile obtained simulating Eq. (4.1)-(7.4) for Case II: $\mathcal{K} = \mathcal{P}$ for three times: $t = 1000$ [s] (top), $t = 2000$ [s] (middle), and $t = 3000$ [s] (bottom).	83
Figure 42 – Vertical velocity field (left panel) and water saturation (right panel) around the traveling wave front at $t = 2000$ [s] for Case II: $\mathcal{K} = \mathcal{P}$. White arrows indicate the mass exchange between layers. The black dashed curve represents the approximate front position.	84
Figure 43 – The water saturation profile obtained simulating Eq. (4.1)-(7.4) for Case III: $\mathcal{K} > \mathcal{P}$ for three times: $t = 3000$ [s] (top), $t^* = 4000$ [s] (middle), and $t = 5000$ [s] (bottom).	84
Figure 44 – Vertical velocity field (left panel) and water saturation (right panel) around the traveling wave front at $t = 4000$ [s] for Case III: $\mathcal{K} > \mathcal{P}$. White arrows indicate the mass exchange between layers. The black dashed curve represents the approximate front position.	85
Figure 45 – Schematic representation of the pressure behavior and crossflow regime of both layers in the presence of foam. The top panels compare the total pressure in layers 1 and 2 (p_1 and p_2). In the bottom panels, the arrows represent the direction of mass exchange between the layers, and the continuous curves represent the wavefront shape.	86
Figure 46 – Average cross-section water saturation profile inside the wavefront obtained from the two-dimensional simulation of Eqs. (4.1)-(7.4) at $t = 5000$ [s], to guarantee that the three fronts are stabilized for Case I (left panel), Case II (middle panel), Case III (right panel). Grey rectangles represent Layer 2 (on the left) and Layer 1 (on the right).	88
Figure 47 – Case I: $\mathcal{K} < \mathcal{P}$. The water saturation profile of each layer for a time 2000 [s] (left), and the horizontal position of the water saturation front (right).	89
Figure 48 – Case I: $\mathcal{K} < \mathcal{P}$. Numerical estimation of the velocities v_1 and v_2 of the water saturation fronts in each layer (left). The black straight line represents the theoretical velocity v_T calculated using Eq. (7.27). The standard deviation of the velocities in each layer (right). The estimated time when these curves stabilize is t^*	90
Figure 49 – Case II: $\mathcal{K} = \mathcal{P}$. The saturation profile of each layer for a time 2000 [s] (left), and the horizontal position of water saturation front (right).	90

Figure 50 – Case II: $\mathcal{K} = \mathcal{P}$. Numerical estimation of the velocities v_1 and v_2 of the water saturation fronts in each layer (left). The black straight line represents the theoretical velocity v_T calculated using Eq. (7.27). The standard deviation of each of the velocities (right). The time when these curves stabilize is t^*	90
Figure 51 – Case III: $\mathcal{K} > \mathcal{P}$. The saturation profile of each layer for a time 4000 [s] (left), and horizontal position of water saturation front (right).	91
Figure 52 – Case III $\mathcal{K} > \mathcal{P}$. Numerical estimation of the velocities v_1 and v_2 of the water saturation fronts in each layer (left). The black straight line represents the theoretical velocity v_T calculated using Eq. (7.27). The standard deviation of each of the velocities (right). The time when these curves stabilize is t^*	91
Figure 53 – Schematic discretization of the numerical domain used to configure the numerical foam flow simulator FOSSIL.	92
Figure 54 – Nose size (N_s tip of water saturation front) in the most permeable layer, depending on the ratio of permeabilities of each layer.	106
Figure 55 – Nose size N_S (tip of water saturation front) in the most permeable layer, depending on the ratio of permeabilities of each layer.	106

CONTENTS

1	INTRODUCTION	18
2	THEORETICAL FOUNDATION	20
2.1	Fractional flow theory	20
2.1.1	Foam flow in porous media	20
2.2	Conservation laws	21
2.3	Traveling wave solution	23
3	MODEL	24
3.1	Foam flow models	24
3.1.1	First order kinetic model	25
3.1.2	Stochastic bubble population model	25
4	THE TRAVELING WAVEFRONT FOR FOAM FLOW IN TWO-LAYER POROUS MEDIA	27
4.1	Introduction	27
4.2	Linear Kinetic Model	28
4.3	Foam flow in two-layers	30
4.3.1	Estimating the mass exchange between layers	32
4.4	Traveling waves solution	34
4.4.1	Equilibria states and the traveling wave velocity	35
4.4.2	Necessary conditions for the existence of the traveling wave connection .	36
4.5	Numerical results	37
4.5.1	Two-dimensional simulations (FOSSIL)	37
4.5.2	Front velocities for 2D model	38
4.5.3	Front velocities for 1D model	39
4.5.4	Characteristic time for the traveling front stabilization	40
4.5.5	Comparing front profiles	41
4.6	Computational simulators and procedures	41
4.6.1	FOSSIL	41
4.6.2	Reaction Convection Diffusion Equations Solver	42
4.6.3	Post-processing the numerical solution	44
4.6.4	Derivation of the ODE system	44
4.7	Quadratic profile	45
4.8	Partial conclusions	46

5	WAVEFRONT VELOCITY FOR FOAM FLOW IN THREE-LAYER POROUS MEDIA	47
5.1	Introduction	47
5.2	Model	48
5.3	Numerical Results	49
5.4	Partial conclusions	53
6	THE TRAVELING FOAM WAVEFRONT IN FRACTURED POROUS MEDIUM	54
6.1	Introduction	54
6.2	Model	55
6.3	Foam flow in n-layers	57
6.3.1	One-dimensional multi-layer simplification	58
6.3.2	Traveling wave velocity	59
6.4	Application of the presented analysis to foam flow in the fractured porous medium.	62
6.5	Symmetric foam front in fractured porous medium	63
6.5.1	Numerical results	66
6.5.1.1	Two-dimensional simulations	66
6.5.1.2	One-dimensional simulations	67
6.6	Non-symmetric foam front in fractured porous medium	69
6.6.1	Numerical results	71
6.6.1.1	Two-dimensional simulations	71
6.6.1.2	One-dimensional simulations	73
6.7	Partial conclusions	74
7	ON THE VISCOUS CROSSFLOW DURING THE FOAM DISPLACEMENT IN TWO-LAYERED POROUS MEDIA	76
7.1	Introduction	76
7.2	Mathematical model	77
7.3	Estimating the wavefront internal structure	79
7.4	Numerical simulation results	81
7.4.1	Case I: $\mathcal{K} < \mathcal{P}$	82
7.4.2	Case II: $\mathcal{K} = \mathcal{P}$	83
7.4.3	Case III: $\mathcal{K} > \mathcal{P}$	84
7.5	Discussion	85
7.6	Traveling wavefront	87
7.6.1	Case I: $\mathcal{K} < \mathcal{P}$	89
7.6.2	Case II: $\mathcal{K} = \mathcal{P}$	89
7.6.3	Case III: $\mathcal{K} > \mathcal{P}$	91

7.7	Foam flow simulator	91
7.8	Partial conclusions	92
8	CONCLUSIONS	94
8.1	Academic contributions	95
	REFERENCES	97
	APPENDIX A - Effect of permeabilities on the nose size . . .	106

1 INTRODUCTION

One of the main challenges in the oil recovery process is fluid dynamics in porous media. When injecting a fluid (water or gas) into the reservoir, the different permeabilities of the medium result in the appearance of preferential paths in the flow, forming a non-uniform front in the sweep of the reservoir, which does not allow piston-type behavior in the wavefront of the injected fluid. This phenomenon is known as “viscous fingering” (see [37]) and schematically can be seen on the left side of Fig. 1. To avoid this, some techniques have been developed that reduce the mobility of the injected fluid. One of these techniques is Water Alternating Gas (WAG) injection, which consists of alternately injecting denser and less dense fluids.

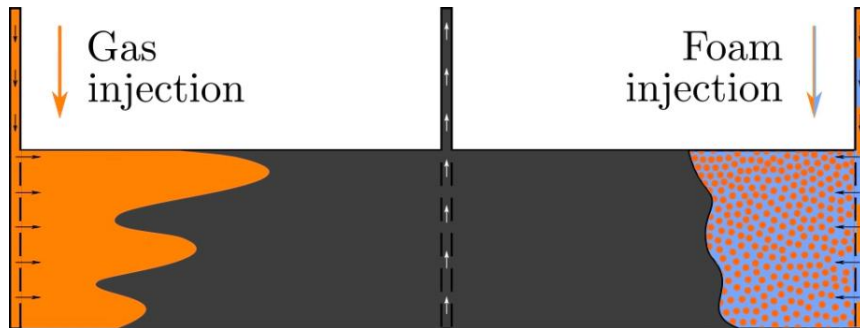


Figure 1 – Gas injection vs. foam injection in a reservoir. Taken from [20]

Although this technique is very effective, it has poor sweep efficiency (see [46, 49]). The reasons for this are mobility contrast between injected gas and displaced phase, channeling (gas prefers to flow through high-permeability layers, so low-permeability layers remain unswept), and gravity override (injected gas has a lower density than existing oil, so it flows to the top of the reservoir), causing a lower unswept region in the reservoir [15].

Another widely used technique is Surfactant Alternated Gas (SAG) injection, which improves the sweep efficiency in the reservoir by trapping the gas in bubbles (foam), thus reducing its mobility. Schematically it can be seen on the right side of Fig. 1. Modeling foam flow in porous media is challenging due to non-Newtonian properties, dependence on foam texture, and the complex process of bubble creation and coalescence [111]. We follow the literature [111, 8, 75] and use a simplification to consider the foam as a Newtonian fluid, thus managing to relate the mobility of the injected phase with the texture of the foam.

In various foam applications in fractured media, a significant challenge involves the issue of “viscous fingering” and the development of preferential flow paths. More precisely, due to the high permeability of the fracture, gas injection often leads to significantly faster movement through the fracture zone, consequently impeding the even displacement of the medium.

An approach to address fractured media, as described in the work of [61], involves treating a fracture as a layer with much smaller thickness and higher absolute permeability compared to the adjacent layers. This allows the use of a simplified model considering a two-dimensional domain with regular geometry (see Fig. 2) to locally study the behavior of foam in fractured porous media.

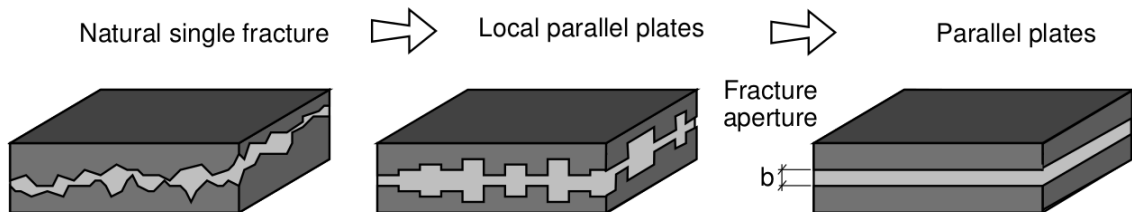


Figure 2 – Layered or fractured media schemes. Taken from [33].

In Fig. 2, the left panel shows the typical form of fractured reservoirs. The other two figures show two different approaches to the problem [33]. In this work, foam flow in layered media is approached as a parallel plate model.

One phenomenon present in layered porous media is the mass exchange between layers, generally known as crossflow. This can occur due to capillary forces or viscous forces [110, 108]. In the case study of the existence of a traveling wave, this phenomenon can either aid or hinder the formation.

This work is organized as follows. In Chapter 2, we present the theoretical foundation, specifically traveling wave type solutions and conservation laws. In Chapter 3, we discuss the mathematical modeling of foam flow in porous media, explaining the linear kinetic [8] and population balance models [116]. In Chapter 4, we present the study of foam displacement in a two-layered porous medium. We investigate the existence of a traveling wave profile and calculate its velocity using mathematical estimates of mass exchange between layers. In Chapter 5, we conduct a numerical study on a three-layered porous medium, simulating a fractured medium. In Chapter 6, we generalize the previous studies to n layers, addressing analytically and numerically the behavior of the foam front in a fractured porous medium. In Chapter 7, we explore the influence of varying absolute permeabilities and porosities on crossflow behavior between layers and the shape of the traveling wave profile. Finally, in Chapter 8, we present the general conclusions and academic contributions of our work.

2 THEORETICAL FOUNDATION

In this chapter, we present the fundamental concepts of fractional flow theory, traveling wave solutions, conservation laws, and dynamical systems, which serve as theoretical support for the main results of this thesis proposal. We refer the reader to [9, 27, 42, 66, 71, 88, 106] for a detailed study of these topic.

2.1 Fractional flow theory

To describe the dynamics of fluids in porous media, the fractional flow theory is commonly used, which calculates the fraction of the total flow of a certain phase in a multiphase flow at any point in the reservoir, assuming that the water saturation at that point is known [27, 66]. This chapter introduces the theory of multiphase fluids in porous media.

2.1.1 Foam flow in porous media

Based on [9], we say that a porous medium is constituted by a solid phase called “porous matrix” and by internal spaces called “pores”. The porosity ϕ of the rock is defined as the ratio between the volume of the pores (symbolized by V_{porous}) and the total volume of the rock (symbolized by V), i.e.

$$\phi = V_{porous}/V.$$

The saturation S_j of each phase j is defined as the fraction occupied by phase j :

$$S_j = V_j/V_{porous}.$$

A porous medium is considered to be fully saturated if the total space is occupied by the phases present, in other words:

$$\sum_j S_j = 1. \quad (2.1)$$

The equations describing two-phase flow in porous media are obtained from the principle of conservation of mass [9]:

$$\frac{\partial}{\partial t}(\phi\rho_j S_j) + \nabla \cdot (\rho_j u_j) = Q, \quad j = w \text{ or } g, \quad (2.2)$$

where ρ_j represents the fluid density of phase j , Q is a source term, ϕ the porosity, and u_j the velocity of phase j . The subindices w and g symbolize the water and gas phases. Assuming incompressible fluids, zero source terms, the equation (2.2) is written in the form:

$$\frac{\partial}{\partial t}(\phi S_j) + \nabla \cdot u_j = 0, \quad j = w \text{ or } g. \quad (2.3)$$

The total surface velocity u is the Darcy's velocity given in [9], and can be written as $u = \sum_j u_j$. Specifically, velocity of phase j can be calculated as follows:

$$u_w = u f_w + \lambda_g f_w \nabla P_c, \quad (2.4)$$

$$u_g = u f_g - \lambda_w f_g \nabla P_c; \quad (2.5)$$

here P_c represents the capillary pressure, λ_j is the relative mobility of phase j . The fractional flow function is given as:

$$f_j = \frac{\lambda_j}{\lambda}, \quad j = w, g.$$

where λ is the total mobility. We present formulas for the relative mobilities and capillary pressure in Chapter 4 and 5.

As the foam texture $n_D(x, t)$ measures the density of lamellae in the gas phase, then the following balance law [8] is considered for foam transport:

$$\frac{\partial}{\partial t}(\phi S_g n_D) + \nabla \cdot (u_g n_D) = \phi S_g \Phi, \quad (2.6)$$

where the function Φ represents foam generation and coalescence.

2.2 Conservation laws

Following [51, 101], we present the general form of conservation laws in spaces of several variables. A system of conservation laws is a system of partial differential equations in the form:

$$\frac{\partial}{\partial t} u + \frac{\partial}{\partial x} f(u) = 0, \quad t > 0, \quad (2.7)$$

where the vector function $u : \Omega \subset \mathbb{R} \times \mathbb{R}^+ \rightarrow \mathbb{R}$ represents the conserved quantities, such as mass, momentum, and energy; and the function $f : \mathbb{R} \rightarrow \mathbb{R}$ is called a flow function. As in [101], the system in (2.7) can be put in the quasilinear form

$$\frac{\partial}{\partial t} u + A(u) \frac{\partial}{\partial x} u = 0, \quad t > 0, \quad (2.8)$$

where $A(u)$ is the $n \times n$ Jacobian matrix of $f(u)$.

Definition 2.2.1. The system (2.7) is called hyperbolic if, for any $u \in \Omega$, the matrix $A(u)$ has n real eigenvalues

$$\lambda_1(u) \leq \lambda_2(u) \leq \dots \leq \lambda_n(u), \quad (2.9)$$

with a complete family (linearly independent) of eigenvectors $r_k(u)$

$$A(u)r_k(u) = \lambda_k(u)r_k(u). \quad (2.10)$$

Let D be an arbitrary domain of \mathbb{R}^n and \vec{n} be the outward unit normal to the boundary ∂D of D . Then, from (2.7) we have that:

$$\frac{d}{dt} \int_D u \, dx + \int_{\partial D} f \vec{n} \, ds = 0. \quad (2.11)$$

The interpretation of this new equation is that the time variation of the integral of u with respect to x in the domain D , is equal to the loss across the boundary ∂D .

From this point, all studies will be done in one dimension, given that we are interested in the *Riemann problem*, which is an initial value problem whose solution u satisfies the initial condition:

$$u_0(x) = \begin{cases} u^- & \text{if } x < 0, \\ u^+ & \text{if } x > 0, \end{cases} \quad (2.12)$$

where the constant vectors u^- and u^+ are the left and right states, respectively.

In general, problems involving conservation laws can present discontinuous solutions (see [101]). When a solution of class C^1 for the problem (2.7) exists, it is called a strong solution. In order to find solutions that are not necessarily C^1 , we look for generalized solutions known as weak solutions [101].

Following [51], we say that u is a *generalized (weak) solution* of the conservation law (2.7) and (2.12), if

$$\int_0^\infty \int_{-\infty}^\infty [u \phi_t + f(u) \phi_x] dx dt + \int_{-\infty}^\infty u_0(x) \phi(x, 0) dx = 0, \quad (2.13)$$

for all test function $\phi \in C^\infty(\mathbb{R} \times [0, \infty))$ with compact support.

In general, if the weak solution of a conservation law problem is not unique, then the use of additional criteria is necessary to find physically relevant solutions.

One way to find a physically relevant solution is to add a small diffusion in the conservation law (2.7), which results in the so-called viscous form

$$u_t + \nabla f(u) = \epsilon u_{xx}, \quad (2.14)$$

where ϵ is a positive constant. A solution to this equation is known as a *viscous profile* and denoted by u^ϵ [91]. The viscous form has better results of existence and uniqueness than the inviscid form, in addition to its solutions being smooth. The physically relevant solutions of the conservation law (2.7) are defined by the following limit

$$u = \lim_{\epsilon \rightarrow 0} u^\epsilon. \quad (2.15)$$

This solutions are called *entropic solutions*.

2.3 Traveling wave solution

A traveling wave solution of Partial Differential Equation (PDE) is characterized geometrically as a wave that moves with a constant velocity maintaining its profile over time. These solutions depend only on the variable $\eta = x - vt$, which implies that the system of PDEs is transformed into a system of ODEs. Such waves appear in several physical problems; as a reference, we can cite [106], where several examples have been developed. Formally, this solution is defined as:

Definition 2.3.1 (Traveling wave solution, [106]). Let us first consider a PDE that involves two variables $x \in \mathbb{R}$, $t \in \mathbb{R}$. A solution $u(x, t)$ is a traveling wave solution, if there is a constant velocity $v \in \mathbb{R}$, an left state u^- , an right state u^+ and a function \hat{u} , such that

$$u(x, t) = \hat{u}(\eta), \quad x \in \mathbb{R}, \quad t \in \mathbb{R}, \quad \eta = x - vt, \quad (2.16)$$

$$\lim_{\eta \rightarrow \pm\infty} \hat{u}(\eta) = \hat{u}_{\pm}, \quad u_- \neq u_+.$$

3 MODEL

In this chapter, we present the fundamental concepts of modeling foam flow in porous media. In addition to this, we present the population balance model presented in [116] and the linear kinetic model presented in [8] used in this research.

3.1 Foam flow models

The models proposed along the years are focused on the gas relative permeability k_{rg} , water relative permeability k_{rw} , the modification of the gas mobility λ_g , and mainly the net foam generation term Φ , that actively models the dynamic of foam generation and coalescence.

The foam displacement in a porous medium can be modeled by the conservation of the mass equation for the water phase (first equation of Eq. (3.1)) and a population-balance equation for foam texture (second equation of Eq. (3.1))

$$\begin{cases} \frac{\partial}{\partial t}(\phi S_w) + \nabla \cdot u_w = 0, \\ \frac{\partial}{\partial t}(\phi S_g n_D) + \nabla \cdot (u_g n_D) = \phi S_g \Phi, \end{cases} \quad (3.1)$$

where S_w is the water saturation as in Chapter 2, $n_D = n_f/n_{max}$ is the dimensionless foam texture, n_f is the dimensional foam texture, Φ represents the net foam source, u_w is the water surface velocity, and u_g is the gas surface velocity, considering $u = u_w + u_g$ as the total surface velocity given by Darcy as:

$$u = -\lambda \nabla P, \quad (3.2)$$

where P is the total pressure; in our case, it is considered a constant pressure gradient, $\lambda = \lambda_w + \lambda_g$ is the total mobility, λ_w and λ_g are mobility of water and gas phases, respectively.

$$\lambda_w = k \frac{k_{rw}}{\mu_w} \quad \text{and} \quad \lambda_g = k \frac{k_{rg}}{\mu_g}. \quad (3.3)$$

The absolute permeability of the medium is defined as k , the relative permeability of water and gas phases are functions defined as in [24] denoted by k_{rw} and k_{rg} , specifically as in [8, 111]

$$k_{rw}(S_w) = \begin{cases} 0, & 0 \leq S_w \leq S_{wc}, \\ C_{krw}^0 \left(\frac{S_w - S_{wc}}{1 - S_{wc} - S_{gr}} \right)^{n_w}, & S_{wc} < S_w \leq 1, \end{cases} \quad (3.4)$$

$$k_{rg}^0(S_w) = \begin{cases} C_{krw}^0 \left(\frac{1 - S_w - S_{gr}}{1 - S_{wc} - S_{gr}} \right)^{n_g}, & 0 \leq S_w < 1 - S_{gr}, \\ 0, & 1 - S_{gr} \leq S_w \leq 1, \end{cases} \quad (3.5)$$

where C_{krw}^0 , C_{krg}^0 are the end-points in the permeabilities curves of water and gas respectively, and n_w , n_g are exponents of Corey for water and gas phase. The gas relative permeability k_{rg} as follows:

$$k_{rg}(S_w, n_D) = \frac{k_{rg}^0(S_w)}{MRF(n_D)}, \quad (3.6)$$

where $MRF(n_D)$ is the mobility reduction factor function in the presence of foam.

The viscosity of water and gas are given by μ_w and μ_g . The medium is assumed to be homogeneous, and the fluids are incompressible. The porous medium is considered to be fully saturated, i.e., $S_w + S_g = 1$.

3.1.1 First order kinetic model

This foam model, proposed in [8], is based on the well-known steady-state foam behavior in porous media. It considers a large, nearly constant, reduction in gas mobility at high water saturation and an abrupt weakening or collapse of foam at a limiting capillary pressure (or, equivalently, at a limiting water saturation S_w^*). Foam texture in local-equilibrium (n_D^{LE}) depends on the water saturation (S_w):

$$n_D^{LE}(S_w) = \begin{cases} \tanh(A(S_w - S_w^*)), & S_w > S_w^* \\ 0, & S_w \leq S_w^*, \end{cases} \quad (3.7)$$

with constant A . The dynamic foam net generation in (3.1) is given in the first-order approach to local-equilibrium bubble texture at any saturation, with a time constant $1/K_c$, as follows

$$\Phi = \frac{r_g - r_c}{n_{max}}, \quad r_g - r_c = K_c n_{max} (n_D^{LE}(S_w) - n_D). \quad (3.8)$$

where r_g and r_c are the generation and coalescence functions, respectively.

In this model, $MRF(n_D)$ is considered as a linear function of n_D .

3.1.2 Stochastic bubble population model

The model proposed by Zitha and Du in [116] is based on foam rheology and stochastic bubble generation ideas. Here, the gas mobility is based on the premise that the foam mobility depends on the degree of foaming of the gas-liquid mixture, measured by the bubble density. The net bubble generation and destruction is considered as

$$\Phi = \frac{\partial n_D}{\partial t} = K_g(n_{max} - n_f) - K_d n_f, \quad (3.9)$$

where K_g and K_d are the bubble generation and bubble destruction or coalescence rate coefficients, respectively, and n_{max} is obtained when $K_d \rightarrow 0$ and $t \rightarrow \infty$. The foam is

considered to be in equilibrium when the generation and coalescence of foam coincide yielding $\Phi = 0$, and

$$n_D^{\text{LE}} = \frac{K_g}{K_g + K_d}. \quad (3.10)$$

Since at [116] considering the bubble and pore volumes are approximately equal near steady state, a close estimate of n_{max} is obtained by fitting the number of pores occupied by the gas, i.e. $n_{\text{max}} = S_g \phi / r^3$, where r is the mean pore radius.

In addition to the generation and coalescence function, the main difference between the models in Sections 3.1.1 and 3.1.2 is that the stochastic model allows working under Newtonian foam conditions, modifying the gas viscosity according to Hirasaki and Lawson's equation given in [49].

4 THE TRAVELING WAVEFRONT FOR FOAM FLOW IN TWO-LAYER POROUS MEDIA

This chapter is a reprint of work published in *Computational Geosciences*, 2022 by Springer, [104]. DOI: 10.1007/s10596-022-10169-z.

The multilayer structure of the porous medium raises a question on its efficiency in dealing with layers of different permeabilities. The present chapter shows the existence of a single traveling wavefront in a two-layer porous medium for a simplified model of foam flow, which was derived from a realistic two-dimensional one. Besides the necessary conditions for the solution's existence, we prove that the traveling wave velocity is a weighted average of the velocities as if both layers were isolated. All theoretical estimates were validated through one- and two-dimensional simulations. Finally, we estimated the order of magnitude of the characteristic time the traveling wavefront needs to stabilize.

4.1 Introduction

The study of foam flow in porous media is of growing interest and has been addressed by many authors, including [96, 77, 46, 48, 59, 14]. Possible applications include oil recovery [46, 41, 2] and pollutant removal [50, 82]. The concept of foam injection processes was introduced in 1958 [77] in the context of hydrocarbon recovery. The key idea is that the presence of foam reduces gas mobility decreasing the fingering effects and improving sweep efficiency.

Several models describing foam flow in porous media have been proposed in the last decades [8, 59, 98, 56]. They can be classified into empirical, semi-empirical, and mechanistic models. Within these, there are two main types: local equilibrium and population balance models [46]. The later type models the foam texture similarly to mass balance equations with particular attention to the physical properties of foam generation and coalescence. Mechanistic population balance models most closely approximate the foam behavior observed in experiments [46] and present advantages when compared to equilibrium models [56].

One of the main reported properties of foam is its destruction at critical pressures [57]. The mechanistic population balance model proposed in [8] accounts for this property in a simple way using a capillary pressure equation. That is why we use this model in the present work.

Geological formations are generally heterogeneous and are often made up of layers of different materials [9]. Several authors investigate multi-phase flow in layered porous media. In [81], the heat transfer between layers with different porosities is studied analytically. In [69, 74, 44, 94, 19, 18] the authors obtain approximate analytical solutions for two-phase flow in two-layered porous medium using the Laplace transform. A different framework

is used in [61], where authors approach fractures in a porous medium as layers and then investigate the two-phase flow in a limit case when the layer width tends to zero.

In the context of foams, the importance of porosity and fluid velocity on foam mobility has been reported in [58]. In [5] the authors use the microfluidic experimental setup to investigate the two-phase flow in the presence of foam. The authors in [95] apply the three-phase fractional flow model to study the velocities and water saturations in a two-layer porous media computationally. Our goal is to mathematically investigate the foam flow in the porous medium formed by two non-isolated layers with different permeabilities.

Several works present experiments and numerical simulations with stable water saturation profiles moving at constant velocity [59, 22, 98, 53]. These results incentive the mathematical investigation of traveling wave solutions, see for example [8, 76]. In particular, in [8] the authors investigated traveling wave solution for three injection conditions during foam injection in the drainage process. These results were further extended in [76], where all possible injection conditions were investigated and classified. From this perspective, the current work shows that this type of solution appears in a two-layer configuration, with the traveling wave velocity being the weighted average of the traveling wave velocities of each layer in case of no mass exchange between them.

This chapter is structured as follows. Section 4.2 presents the two-dimensional version of the linear kinetic model. In Section 4.3, we simplify the original model to a one-dimensional case at the cost of doubling the number of equations, including estimating the mass exchange coefficient between layers. In Section 4.4 investigates the traveling wave solution. Section 4.5 presents the main results, including validating the traveling wave velocity for both two- and one-dimensional models and estimating the time the traveling wavefront needs to stabilize. Finally, Section 4.8 summarize our conclusions.

4.2 Linear Kinetic Model

In the present section we use the extension of the original linear kinetic model [7] proposed in [29]. The model describes incompressible and immiscible two-phase foam flow in a saturated isotropic porous medium using the water mass conservation equation (4.1), the foam population balance equation (4.2), Darcy equation (4.3), and incompressibility condition (4.4):

$$\phi \frac{\partial}{\partial t} S_w + \nabla \cdot u_w = 0; \quad (4.1)$$

$$\phi \frac{\partial}{\partial t} (S_g n_D) + \nabla \cdot (u_g n_D) = \phi S_g \Phi; \quad (4.2)$$

$$u = -\lambda \nabla P; \quad (4.3)$$

$$\nabla \cdot u = 0, \quad (4.4)$$

where ϕ represent the porosity, S_w and S_g are saturations of water and gas ($S_w + S_g = 1$), u_w and u_g are partial velocities of water and gas, $u = u_w + u_g$ is the total surface velocity, the total pressure P is considered as the sum of all pressures P_i for each phase i [66, 27], and λ is the total mobility defined below. The number of lamellae per unit volume in the gas phase is defined as the foam texture, usually denoted as n_f [8, 46]. In this work $n_D = n_f/n_{max}$ as in [7, 8, 111], represents the normalized foam texture in relation to the maximum number of lamellae n_{max} in the medium.

The foam generation/coalescence source term is $\Phi = K_c(n_D^{LE}(S_w) - n_D)$ with the foam texture in local equilibrium given by:

$$n_D^{LE}(S_w) = \begin{cases} \tanh(A(S_w - S_w^*)), & S_w > S_w^*; \\ 0, & S_w \leq S_w^*, \end{cases} \quad (4.5)$$

where S_w^* represents the critical water saturation below which foam is unstable and A is a constant model parameter.

The model is completed with equations from the standard fractional flow theory [9, 113]. Fractional flow functions (f_w and f_g), total mobility λ , and relative mobilities (λ_w and λ_g) for water and gas are given by

$$\lambda_w = k \frac{k_{rw}}{\mu_w}, \quad \lambda_g = k \frac{k_{rg}}{\mu_g}, \quad f_w = \frac{\lambda_w}{\lambda_w + \lambda_g}, \quad f_g = \frac{\lambda_g}{\lambda_w + \lambda_g}, \quad \lambda = \lambda_w + \lambda_g, \quad (4.6)$$

where μ_w and μ_g are viscosities of water and gas, and k is a scalar permeability (depends on the space variables x and z). Relative permeabilities of water and gas (k_{rw} and k_{rg}) are defined following [8], considering that foam does not affect the relative permeability of water but affects the one of gas (see [35] for details):

$$k_{rw}(S_w) = \begin{cases} 0, & 0 \leq S_w \leq S_{wc}, \\ 0.2 \left(\frac{S_w - S_{wc}}{1 - S_{wc} - S_{gr}} \right)^{4.2}, & S_{wc} < S_w \leq 1, \end{cases} \quad (4.7)$$

$$k_{rg}^0(S_w) = \begin{cases} 0.94 \left(\frac{1 - S_w - S_{gr}}{1 - S_{wc} - S_{gr}} \right)^{1.3}, & 0 \leq S_w < 1 - S_{gr}, \\ 0, & 1 - S_{gr} \leq S_w \leq 1, \end{cases} \quad (4.8)$$

$$k_{rg}(S_w, n_D) = \frac{k_{rg}^0(S_w)}{\text{MRF}(n_D)}, \quad (4.9)$$

where the mobility reduction factor is given by

$$\text{MRF}(n_D) = 18500n_D + 1. \quad (4.10)$$

Finally, assuming that the total mass inflow is prescribed, the total surface velocity $u = u_g + u_w$ is given. The water partial velocity (see [23]) is

$$u_w = u f_w + \lambda_g f_w \nabla P_c, \quad (4.11)$$

Table 1 – Parameter values for the problem of two layers.

Symbol	Value	Parameter
S_{wc}	0.2 [-]	connate water saturation
S_{gr}	0.18 [-]	residual gas saturation
μ_w	10^{-3} [Pa s]	water viscosity
μ_g^0	$2 \cdot 10^{-5}$ [Pa s]	gas viscosity in absence of foam
k_1	$2 \cdot 10^{-12}$ [m ²]	permeability of medium in layer 1
k_2	10^{-12} [m ²]	permeability of medium in layer 2
n_{max}	$8 \cdot 10^{13}$ [m ⁻³]	maximum foam texture
u_1	$2.93 \cdot 10^{-6}$ [m s ⁻¹]	total superficial velocity of layer 1
u_2	$1.465 \cdot 10^{-6}$ [m s ⁻¹]	total superficial velocity of layer 2
S_w^*	0.37 [-]	critical water saturation
S_w^-	0.372 [-]	injected water saturation
S_w^+	0.72 [-]	initial water saturation
n_D^-	0.664 [-]	injected foam texture
n_D^+	1 [-]	initial foam texture
K_c	200 [s ⁻¹]	foam creation/coalescence constant
A	400 [-]	foam model parameter
ϕ	0.25 [-]	porosity
c	0.01 [-]	capillary pressure power parameter
d	$5 \cdot 10^{-3}$ [m]	depth of layers 1 and 2
σ	0.03 [N m ⁻¹]	gas-water interfacial tension

and the capillary-pressure P_c , which is the difference between the phase pressures ($P_c = P_w - P_g$), is defined as in [71]:

$$P_c = \sigma \sqrt{\frac{\phi}{k}} \frac{0.022 (1 - S_w - S_{gr})^c}{(S_w - S_{wc})}. \quad (4.12)$$

The final system contains four partial differential equations (4.1)-(4.4) (considering that we substituted (4.5)-(4.12)) and four main variables S_w , n_D , u , and P .

4.3 Foam flow in two-layers

Our goal is to mathematically investigate what happens with two-dimensional foam displacement in a simple two-layer configuration, common in porous media applications [9]. Thus, we consider a rectangular domain $\Omega := (0, L) \times (-d, d)$ with total length L along the axis x and the height $2d$ along the axis z , see Fig. 3. We use x and z notation for the horizontal and vertical axes, respectively, as is common in the literature (see [31, 32]). The value of d is taken from [5].

Following the literature [11, 82, 87, 114], we consider a constant pressure gradient yielding constant superficial velocity at each layer. This assumption also makes unnecessary equations (4.3) and (4.4). In this way, the complete model (4.1)-(4.4) becomes one-dimensional at the cost of doubling the number of equations (and four variables S_{w1} , S_{w2} ,

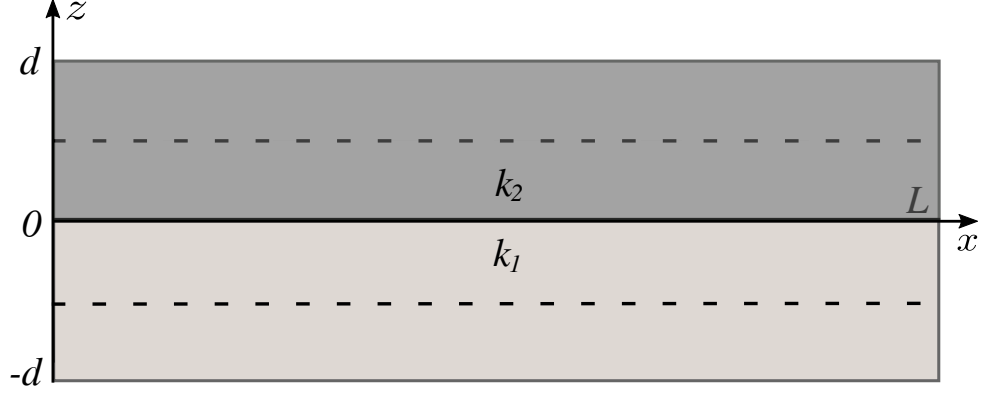


Figure 3 – Schematic representation of the domain $\Omega := (0, L) \times (-d, d)$ composed of two layers with permeabilities k_i .

n_{D_1} , and n_{D_2}):

$$\begin{cases} \phi \frac{\partial}{\partial t} S_{w_1} + \frac{\partial}{\partial x} u_{w_1} & = -\theta_{s_1} (S_{w_1} - S_{w_2}), \\ \phi \frac{\partial}{\partial t} (S_{g_1} n_{D_1}) + \frac{\partial}{\partial x} u_{g_1} n_{D_1} & = \phi S_{g_1} \Phi_1, \\ \phi \frac{\partial}{\partial t} S_{w_2} + \frac{\partial}{\partial x} u_{w_2} & = \theta_{s_2} (S_{w_1} - S_{w_2}), \\ \phi \frac{\partial}{\partial t} (S_{g_2} n_{D_2}) + \frac{\partial}{\partial x} u_{g_2} n_{D_2} & = \phi S_{g_2} \Phi_2, \end{cases} \quad (4.13)$$

where constants k_i , θ_{s_i} , variables S_{w_i} , S_{g_i} , n_{D_i} , and functions Φ_i , u_{w_i} , P_{c_i} are defined for each layer $i \in \{1, 2\}$. Using the volume average technique, similar to [28, 68], the water saturations in each layer are given by:

$$S_{w_1} = \frac{1}{d} \int_{-d}^0 S_w(z) dz, \quad S_{w_2} = \frac{1}{d} \int_0^d S_w(z) dz. \quad (4.14)$$

In this work, we consider constant superficial velocities u_i in each layer, the velocities u_{w_i} and u_{g_i} are defined as in Eq. (4.11):

$$u_{w_i} = u_i f_{w_i} + \lambda_g f_{w_i} \nabla P_{c_i}, \quad (4.15)$$

where $u_i = u_{w_i} + u_{g_i}$.

The constant θ_{s_i} corresponds to the mass exchange between both layers and will be addressed in the next section. The system of PDEs (4.1)-(4.4) is solved as a Riemann problem, i.e., a problem with the initial conditions in the form of a step function:

$$(S_{w_1}, n_{D_1}, S_{w_2}, n_{D_2})(x, 0) = \begin{cases} (S_{w_1}^-, n_{D_1}^-, S_{w_2}^-, n_{D_2}^-), & \text{if } x < 0 \\ (S_{w_1}^+, n_{D_1}^+, S_{w_2}^+, n_{D_2}^+), & \text{if } x \geq 0 \end{cases}. \quad (4.16)$$

When compared to the complete model (4.1)-(4.4) with domain Ω (Fig. 3) the boundary with superscript “+” corresponds to the initial reservoir condition and superscript “-” corresponds to the injection condition. The values of $n_{D_1}^-$ and $n_{D_2}^+$ are calculated using Equation (4.5) and are reported in Table 1.

4.3.1 Estimating the mass exchange between layers

In this section, we estimate the mass exchange terms by assuming some oversimplifying hypotheses: (1) fast mass exchange between layers leading to a simplified mass balance equation in the vertical direction ($\partial_t(\phi S_w) + \partial_z u_w = 0$), and (2) assuming that this mass exchange between layers is mainly due to diffusion ($u = 0$). This estimate procedure is common in the literature; see [114] for similar cases. Considering only vertical flow (z direction), the surface velocity of water in z direction is:

$$u_w^z = u f_w + \lambda_g f_w \frac{\partial P_c}{\partial S_w} \frac{\partial S_w}{\partial z}. \quad (4.17)$$

Using the oversimplifying hypotheses above with Eq. (4.17) yields

$$\frac{\partial}{\partial t}(\phi_i S_w) = -\frac{\partial}{\partial z} \left(\lambda_{g_i} f_{w_i} \frac{\partial P_{c_i}}{\partial S_w} \frac{\partial S_w}{\partial z} \right), \quad i = 1, 2. \quad (4.18)$$

Let us consider a representative part of the original porous medium as depicted in Fig. 3. Assuming there are no external mass losses, the mass exchange rate between layers inside this volume can be regarded as a total variation of mass in each layer:

$$R_1 = \frac{1}{d} \frac{\partial}{\partial t} \int_{-d}^0 \phi S_w dz, \quad R_2 = \frac{1}{d} \frac{\partial}{\partial t} \int_0^d \phi S_w dz, \quad (4.19)$$

where the total mass conservation is given by $R_1 = -R_2$. Notice that by substituting the definition of terms R_1, R_2 (Eqs. (4.19)) and S_{w_1} and S_{w_2} (Eqs. (4.14)) into the system (13) and using the oversimplifying hypothesis $u = 0$, we obtain that $R_1 = -\theta_{s_1} (S_{w_1} - S_{w_2})$, and $R_2 = \theta_{s_2} (S_{w_1} - S_{w_2})$.

Assuming that there is no flow on the outside boundary, we calculating integrals for each layer separately:

$$R_1 = \frac{\bar{D}_1}{d} \frac{\partial S_w}{\partial z} \Big|_{z \rightarrow 0^-}, \quad R_2 = -\frac{\bar{D}_2}{d} \frac{\partial S_w}{\partial z} \Big|_{z \rightarrow 0^+}, \quad (4.20)$$

with positive coefficients:

$$\bar{D}_1 = -\lim_{z \rightarrow 0^-} \lambda_{g_1} f_{w_1} \frac{\partial P_{c_1}}{\partial S_w}, \quad \bar{D}_2 = -\lim_{z \rightarrow 0^+} \lambda_{g_2} f_{w_2} \frac{\partial P_{c_2}}{\partial S_w}. \quad (4.21)$$

Notice that \bar{D}_1, \bar{D}_2 do not depend on z , but depend on water saturation value on the boundary between both layers S_{w_0} . For fractional flow functions given in (4.6) $f_{w_1} = f_{w_2}$.

The water saturation profile in each layer can be approached by the parabolic function (see Fig. 4):

$$S_w(z) = \begin{cases} a_1 z^2 + b_1 z + c_1, & \text{if } z < 0, \\ a_2 z^2 + b_2 z + c_2, & \text{if } z \geq 0, \end{cases} \quad (4.22)$$

where a_i, b_i, c_i for $i = 1, 2$ are constants.

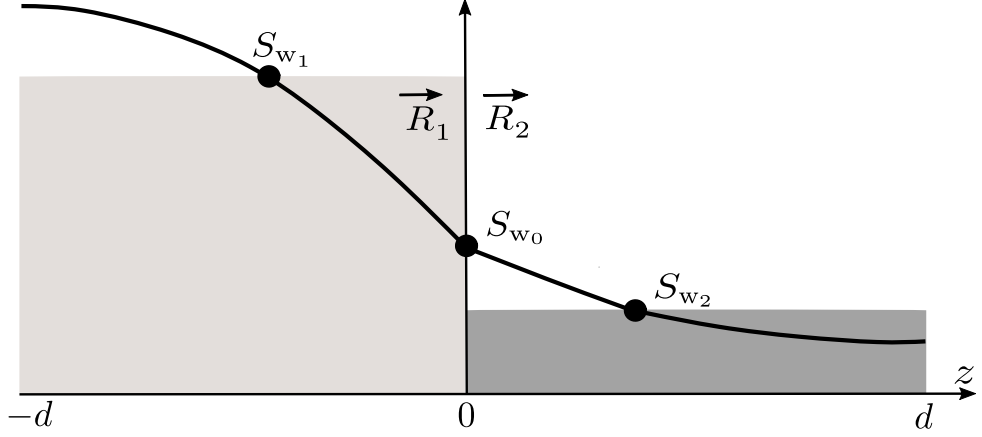


Figure 4 – Schematic representation of water saturation S_w along the vertical cross section of the two layer porous medium.

A brief derivation of this approximation is presented in Appendix Section 4.7 motivated by numerical simulations' results, see Fig. 7. Moreover, we assume that the average water saturation in each layer matches S_{w1} and S_{w2} and that $S_w(z)$ satisfies a no-flow condition at the external boundaries:

$$S_{w1} = \int_{-d}^0 \frac{S_w(z)}{d} dz, \quad S_{w2} = \int_0^d \frac{S_w(z)}{d} dz, \quad \left. \frac{\partial S_w}{\partial z} \right|_{\pm d} = 0, \quad S_w(0) = S_{w0}. \quad (4.23)$$

Substituting (4.23) into (4.22) results in $b_1 = 2a_1d$, $c_1 = S_{w1} + 2a_1d^2/3$, $b_2 = -2a_2d$, $c_2 = S_{w2} + 2a_2d^2/3$ and $S_{w0} = c_1 = c_2$. Using these coefficients in (4.20) we obtain

$$R_1 = 2\bar{D}_1 a_1, \quad R_2 = 2\bar{D}_2 a_2. \quad (4.24)$$

Using the mass conservation $R_1 = -R_2$ we obtain $\bar{D}_1 a_1 = -\bar{D}_2 a_2$, therefore $a_1 = -(\bar{D}_2/\bar{D}_1)a_2$. Using this relation yields:

$$a_1 = \frac{-3}{2d^2} \frac{\bar{D}_2}{\bar{D}_2 + \bar{D}_1} (S_{w1} - S_{w2}), \quad a_2 = \frac{3}{2d^2} \frac{\bar{D}_1}{\bar{D}_2 + \bar{D}_1} (S_{w1} - S_{w2}). \quad (4.25)$$

Substituting (4.25) into (4.24) we obtain the mass exchange rate between both layers:

$$R_1 = \frac{-3}{d^2} \frac{\bar{D}_2 \bar{D}_1}{\bar{D}_1 + \bar{D}_2} (S_{w1} - S_{w2}), \quad R_2 = \frac{3}{d^2} \frac{\bar{D}_2 \bar{D}_1}{\bar{D}_1 + \bar{D}_2} (S_{w1} - S_{w2}). \quad (4.26)$$

Thus the mass exchange coefficients in (4.13) can be estimated as

$$\theta_{s1} = \frac{-3\bar{D}_2 \bar{D}_1}{d^2 (\bar{D}_2 + \bar{D}_1)}, \quad \theta_{s2} = \frac{3\bar{D}_2 \bar{D}_1}{d^2 (\bar{D}_2 + \bar{D}_1)}. \quad (4.27)$$

For the parameter values from Table 1, $-\theta_{s1} = \theta_{s2} = 3.2 \times 10^{-4}$ and $S_{w0} = 0.4738$.

Remark 4.3.1. Notice that the approach in (4.22) is valid for the dynamic situation; in the steady case, we can use the stationary version of the equation, resulting in linear saturation profiles in z direction. The latter approach gives similar results; however, the former one provides better estimate for time the initial solution needs to assume a stable traveling wave profile, as presented in Section 4.5.1.

4.4 Traveling waves solution

In the context of the foam displacement in porous media, several experiments point to profiles similar to traveling waves [98, 53, 59] motivating to search for analytical solutions describing this phenomenon in the form of a traveling wave, see [8, 76] and references therein. One can regard a traveling wave as a stationary solution of the ODE resulting from specific variable substitution in the original system of PDEs [106].

Definition 4.4.1. A solution $S_{w_i}(x, t)$, $n_{D_i}(x, t)$, $i = 1, 2$ of system (4.13) is a traveling wave if there exists a speed $v \in \mathbb{R}$, a left state $(S_{w_1}^-, n_{D_1}^-, S_{w_2}^-, n_{D_2}^-) \in \mathbb{R}^4$, a right state $(S_{w_1}^+, n_{D_1}^+, S_{w_2}^+, n_{D_2}^+) \in \mathbb{R}^4$ and functions \widehat{S}_{w_i} and \widehat{n}_{D_i} , such that

$$\begin{aligned} S_{w_i}(x, t) &= \widehat{S}_{w_i}(\eta), \quad n_{D_i}(x, t) = \widehat{n}_{D_i}(\eta), \quad \eta = x - vt, \\ \lim_{\eta \rightarrow \pm\infty} \widehat{S}_{w_i}(\eta) &= S_{w_i}^\pm \quad \text{and} \quad \lim_{\eta \rightarrow \pm\infty} \widehat{n}_{D_i}(\eta) = n_{D_i}^\pm. \end{aligned} \quad (4.28)$$

In this case, the limit states $(S_{w_1}^\pm, n_{D_1}^\pm, S_{w_2}^\pm, n_{D_2}^\pm)$ of the Riemann problem become α - and ω -limits of the corresponding dynamical system [42]. In what follows, we abuse the notation and omit hats over the variables. Indicating the derivatives in η as primes, the traveling wave solution of the system (4.13) satisfies (Section 4.6.4 provides a full derivation):

$$\begin{cases} S'_{w_1} = Y_1, \\ n'_{D_1} = \Psi_1/F_1, \\ S'_{w_2} = Y_2, \\ n'_{D_2} = \Psi_2/F_2, \\ Y'_1 = \left[-\theta_{s_1} (S_{w_1} - S_{w_2}) + Z_1 Y_1 - u_1 \frac{\partial f_{w_1}}{\partial n_D} \frac{\Psi_1}{F_1} \right] / D_1, \\ Y'_2 = \left[\theta_{s_2} (S_{w_1} - S_{w_2}) + Z_2 Y_2 - u_2 \frac{\partial f_{w_2}}{\partial n_D} \frac{\Psi_2}{F_2} \right] / D_2, \end{cases} \quad (4.29)$$

where Ψ_i , F_i , D_i , and Z_i are functions of (S_{w_i}, n_{D_i}) given by

$$\Psi_i = (-1)^i \theta_{s_i} (S_{w_1} - S_{w_2}) n_{D_i} + \phi_i S_{g_i} \Phi_i, \quad (4.30)$$

$$F_i = u_i f_{g_i} - \phi_i v S_{g_i} - D_i Y_i, \quad (4.31)$$

$$D_i = \lambda_{g_i} f_{w_i} \frac{dP_{c_i}}{dS_w}, \quad (4.32)$$

$$Z_i = \phi_i v - u_i \frac{\partial f_{w_i}}{\partial S_w} - Y_i \frac{\partial D_i}{\partial S_w} - \frac{\Psi_i}{F_i} \frac{\partial D_i}{\partial n_D}. \quad (4.33)$$

Remark 4.4.1. In order to continue the analysis of System (4.29) one needs to verify that its flux terms are well defined. Consider $S_{w_i} \in (S_{wc}, 1 - S_{gr})$ and S_w^b to be the intersection point between the water fractional flow function in local equilibrium and the straight line that passes through points $(S_{wc}, 0)$ and $(1, 1)$ (see [75] for details). It follows that $D_i \neq 0$ and for $n_{D_i} \geq n_{D_i}^{LE}(S_w^b + 10^{-4})$, F_i is not null. Thus, all flux functions in System (4.29) are well defined. All numerical examples shown in this article use $S_w^- = 0.372$, $S_w^+ = 0.72$, and $K_c = 200$ (corresponding to region II of [76]) and satisfy these conditions.

4.4.1 Equilibria states and the traveling wave velocity

In order to verify the necessary conditions for the existence of traveling wave solutions of (4.13), we need to find the equilibria of the dynamical system (4.29). Equilibria (or stationary solutions) are roots of the right side of the system (4.29), i.e., they satisfy:

$$Y_i = 0, \quad (4.34)$$

$$\Psi_i/F_i = 0, \quad (4.35)$$

$$\left[(-1)^i \theta_{s_i} (S_{w_1} - S_{w_2}) + Z_i Y_i - u_i \frac{\partial f_{w_i}}{\partial n_D} \frac{\Psi_i}{F_i} \right] / D_i = 0. \quad (4.36)$$

Notice that if (4.34) and (4.35) are valid, then (4.36) is satisfied if and only if $S_{w_1} = S_{w_2}$. On the other hand, substituting (4.34)-(4.35) into (4.36) it follows that at equilibria points the following restrictions are satisfied:

$$S_{w_1} = S_{w_2}, \quad \text{and} \quad n_{D_i} = n_{D_i}^{LE}(S_{w_i}), \quad i = \{1, 2\}. \quad (4.37)$$

To locate the equilibrium point water saturation, we substitute the traveling coordinates in the water mass conservation law of the original PDE system (4.13) and integrate the resulting equation in η . After some manipulations (see [8, 76] for details) we arrive at

$$\begin{cases} S_{w_i} = \frac{\phi_i v_i (S_{w_i} - S_{w_i}^+) - u_i (f_{w_i} - f_{w_i}^+)}{\lambda_{g_i} f_{w_i} dP_{c_i} / dS_w}, \\ v_i = \frac{u_i}{\phi_i} v_{s_i} = \frac{u_i}{\phi_i} \frac{f_{w_i}^+ - f_{w_i}^-}{S_{w_i}^+ - S_{w_i}^-}, \end{cases} \quad (4.38)$$

where v_i would be the traveling wave velocity in the layer i if there was no mass exchange between layers. Notice that at equilibrium state $S'_{w_i} = 0$ meaning

$$f_{w_i}(S_{w_i}, n_{D_i}^{LE}(S_{w_i})) - v_{s_i} S_{w_i} - f_{w_i}^+ + v_{s_i} S_{w_i}^+ = 0. \quad (4.39)$$

For each layer, the equation (4.39) can be regarded as the intersection between the corresponding fractional flow function in local equilibrium and the straight line that passes through points $(S_{w_i}^-, f_{w_i}^-)$ and $(S_{w_i}^+, f_{w_i}^+)$ with slope $v_{s_i} = v_{s_i}(S_{w_i}^-, S_{w_i}^+)$. Thus, for each layer there can exist two or three as in one-layer model, see [76]. In particular $(S_{w_i}^-, n_{D_i}^-) \in \mathbb{R}^4$ and $(S_{w_i}^+, n_{D_i}^+) \in \mathbb{R}^4$ are equilibria of (4.29).

One of the key parts of this work is the traveling wave velocity given below.

Proposition 4.4.1. *Assuming that the system (4.13) possesses a traveling wave solution in the sense of Definition 4.4.1, traveling wave velocity v is:*

$$v = \frac{a_1 v_1 + a_2 v_2}{a_1 + a_2}, \quad a_1 = \phi_1 (S_{w_1}^+ - S_{w_1}^-) \theta_{s_2}, \quad a_2 = \phi_2 (S_{w_2}^+ - S_{w_2}^-) \theta_{s_1}, \quad (4.40)$$

where v_1 and v_2 are given in (4.38).

Proof. By hypothesis there exists a traveling wave solution of (4.37) with asymptotic boundary conditions (4.28). Substituting the traveling coordinates ($\eta = x - vt$) into the first and the third equations in (4.13) we obtain

$$\begin{cases} -v\phi_1 \frac{dS_{w_1}}{d\eta} + \frac{du_{w_1}}{d\eta} = -\theta_{s_1} (S_{w_1} - S_{w_2}), \\ -v\phi_2 \frac{dS_{w_2}}{d\eta} + \frac{du_{w_2}}{d\eta} = \theta_{s_2} (S_{w_1} - S_{w_2}). \end{cases} \quad (4.41)$$

Equating the source terms in (4.41), integrating the resultant relation in ξ from $-\infty$ to ∞ , and substituting the boundary conditions (4.28) we obtain

$$\begin{aligned} \theta_{s_2} (u_1 f_{w_1}^+ - v\phi_1 S_{w_1}^+) + \theta_{s_1} (u_2 f_{w_2}^+ - v\phi_2 S_{w_2}^+) = \\ \theta_{s_2} (u_1 f_{w_1}^- - v\phi_1 S_{w_1}^-) + \theta_{s_1} (u_2 f_{w_2}^- - v\phi_2 S_{w_2}^-). \end{aligned} \quad (4.42)$$

Isolating v we conclude that:

$$v = \frac{u_1(f_{w_1}^+ - f_{w_1}^-)\theta_{s_2} + u_2(f_{w_2}^+ - f_{w_2}^-)\theta_{s_1}}{\phi_1(S_{w_1}^+ - S_{w_1}^-)\theta_{s_2} + \phi_2(S_{w_2}^+ - S_{w_2}^-)\theta_{s_1}} = \frac{a_1 v_1 + a_2 v_2}{a_1 + a_2}, \quad (4.43)$$

where v_1, v_2 are defined in (4.38) and a_1, a_2 are in (4.40). \square

For the parameter values from Table 1, $v = 1.84 \times 10^{-5}$ [m/s], which is weighted average of the velocities of $v_1 = 2.46 \times 10^{-5}$ [m/s] and $v_2 = 1.23 \times 10^{-5}$ [m/s], which would be the traveling wave velocities if the layers were isolated. Notice that u_i in Table 1 is the superficial velocity, that is why the traveling wave velocity, connected to Darcy velocity is larger.

4.4.2 Necessary conditions for the existence of the traveling wave connection

Due to the high dimension of ODE system (4.29), we were not able to have a rigorous proof of the traveling wave existence connecting equilibria in (4.28). Such proof in the six-dimensional phase space is beyond the scope of the paper. However, we can use some tools from dynamical system analysis to verify the necessary conditions.

The existence of the traveling wave connection in the sense of Definition 4.4.1 is equivalent to the existence of the intersection between unstable manifold $W_U(U^-)$ of U^- and stable manifold $W_S(U^+)$ of U^+ , see [42] where, $U^- = (S_{w_1}^-, n_{D_1}^-, S_{w_2}^-, n_{D_2}^-, Y_1^-, Y_2^-)$, and $U^+ = (S_{w_1}^+, n_{D_1}^+, S_{w_2}^+, n_{D_2}^+, Y_1^+, Y_2^+)$. In the neighborhood of equilibria, the dimension of these manifolds can be estimated by using the Jacobian matrix of the flux in ODE (4.29). In the hyperbolic case (i.e., when all the eigenvalues of the Jacobian possess non-null real part), the Stable Manifold Theorem yields that the dimensions of $W_U(U^-)$ and $W_S(U^+)$ coincide with the number of eigenvalues with positive and negative real parts respectively.

From an applications point of view, we expect the traveling wave connection to exist for at least some range of parameter values; thus, it would be desirable that the sum

of the dimensions of $W_U(U^-)$ and $W_S(U^+)$ to be larger than the dimension of the phase space (in this case, six). In all examples presented in this paper, we verified numerically that all equilibria are hyperbolic and that the dimension condition is satisfied.

4.5 Numerical results

This section shows the relation between the two-dimensional model solutions, one-dimensional model solutions, and traveling wave estimates.

4.5.1 Two-dimensional simulations (FOSSIL)

We use FOSSIL (see Section 4.6.1 for more details) to solve System (4.1)-(4.4) numerically in the two-layer domain Ω (see Fig. 3) with initial conditions approaching the step function (4.16). We use no-flow boundary conditions at $z = -d$ and $z = d$. At the inlet ($x = 0$), we define constant velocities $u = u_i$ for each layer and fixed saturation $S_w = S_w^-$. On the output boundary ($x = L$), we consider $\partial S_w / \partial x = 0$.

Figures 5-6 show profiles for water saturation and foam texture at times 3000s, 4000s and 5000s. As one can see, these simulations suggest a traveling wave profile moving at the same velocity within both layers. The shape of this profile resembles a parabola and inspired the hypothesis used in Section 4.3.1.

Figure 7 presents an internal structure of the saturation front profile obtained through a post-processing of the wavefront at 5000s see Fig. 5. Considering only those x corresponding to the front, for each position z , we plot the average of the numerical values of $S_w(x, z, t)$ for $x \in [0.373, 0.719]$, and $t = 5000$ s. Using this technique, we can use a linear interpolation over the nodes of the curve to find the water saturation at the boundary between both layers: $S_{w_0} = 0.4732$. Notice that this value is in good agreement (less than 0.06%) with the one estimated theoretically in Section 4.3.1.

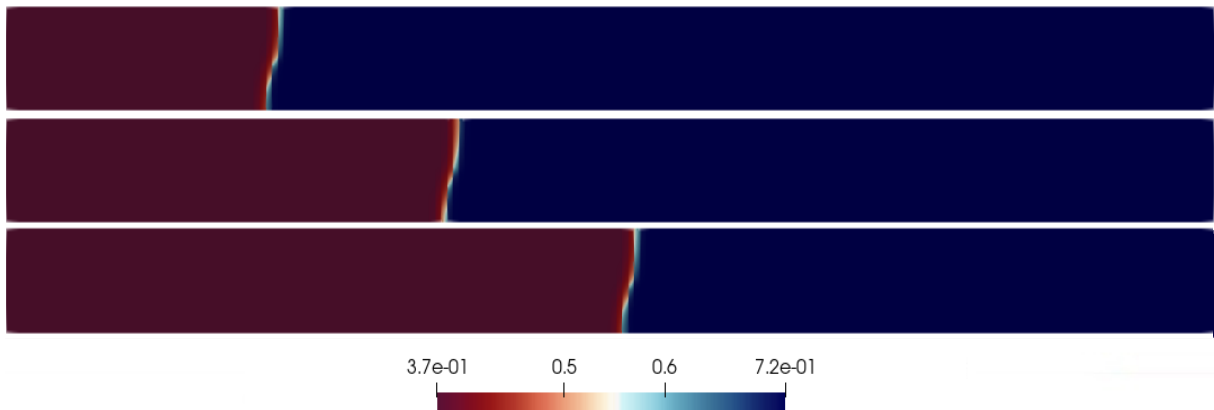


Figure 5 – Stable traveling water saturation profile obtained through two-dimensional numerical simulations at 3000s (upper plot), 4000s (middle plot) and at 5000s (lower plot).

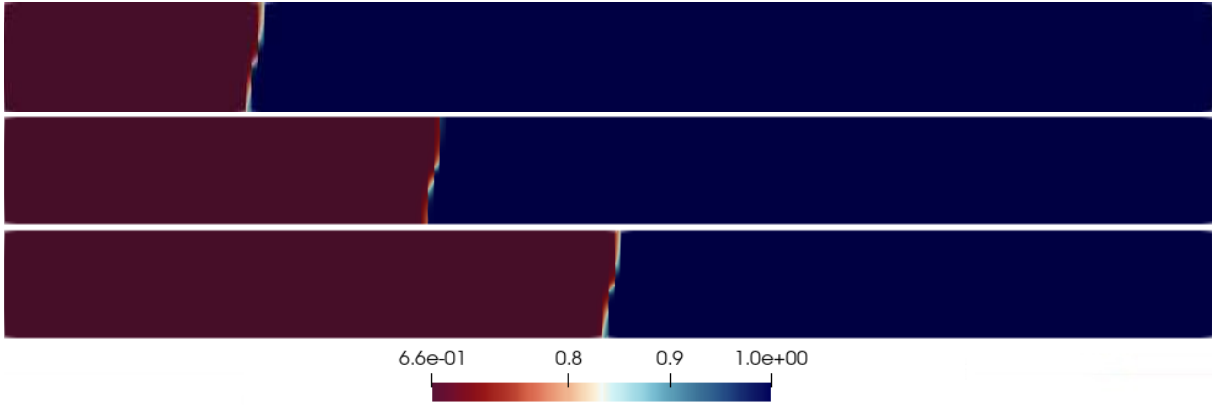


Figure 6 – Stable traveling foam texture profile obtained through two-dimensional numerical simulations at 3000s (upper plot), 4000s (middle plot) and at 5000s (lower plot).

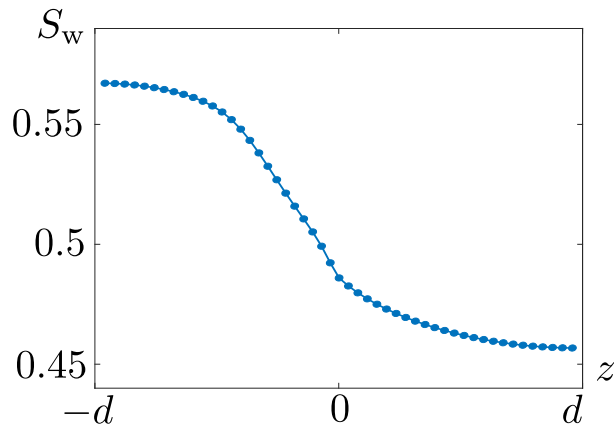


Figure 7 – Average cross-section water saturation profile inside the wave front obtained numerically for $t = 5000$ s.

4.5.2 Front velocities for 2D model

Using the average front positions in each layer (see Section 4.6.3 for details) we estimate the wave front velocity in each layer $i \in \{1, 2\}$ at each time step $k \in \{1, \dots, n_T\}$ using finite differences:

$$v_{i,k} := \frac{x_{i,k} - x_{i,k-1}}{\Delta t}. \quad (4.44)$$

Figure 8 compares the moving average of the velocity arrays v_i using samples of 45 values (0.9% of $n_T = 5000$) with the theoretical velocity (4.40). As expected, wavefronts velocities in both layers tend to the same constant value, indicating the traveling wave's existence common to both layers. Figure 9 shows the Standard Deviation (SD) of the moving average of the velocity in each layer:

$$SD(v(i)) = \sqrt{\frac{\sum_{k=i}^{i+n} (m_n(k) - \bar{v}(i))^2}{n-1}}, \quad \text{where} \quad \bar{v}(i) = (1/n) \sum_{k=i}^{i+n} m_n(k). \quad (4.45)$$

As the velocity presents significant oscillations, in order to conclude that the numerically obtained velocity is approaching the theoretical estimate, we need SD to be significantly smaller than the velocity itself. Notice that $SD(v_1)$ and $SD(v_2)$ are in the same order of magnitude as $|v_i|$ at the beginning of the simulations and decrease at least one order of magnitude along with the simulation, indicating the convergence of the foam front velocity.

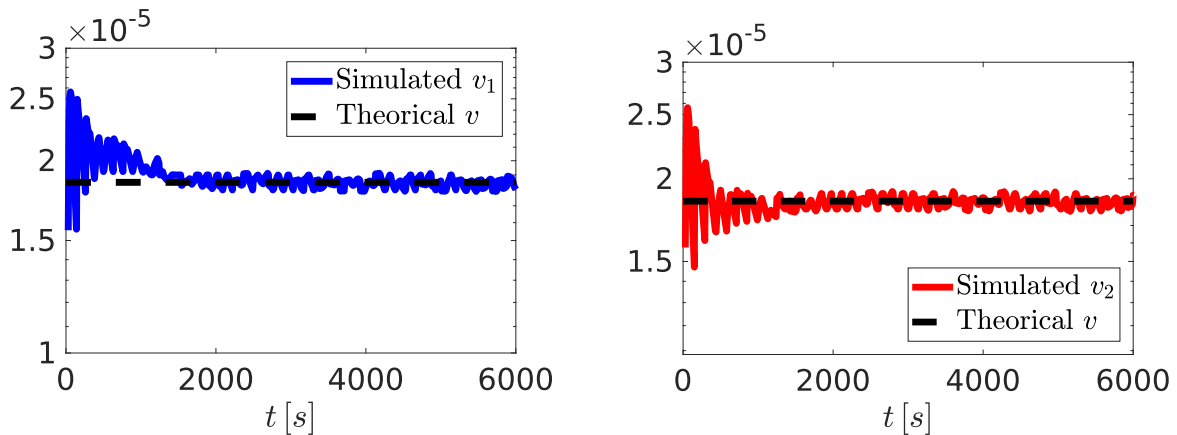


Figure 8 – Moving average of the velocities v_1 (left) and v_2 (right) of the two-dimensional model compared to the analytically estimated v from (4.40).

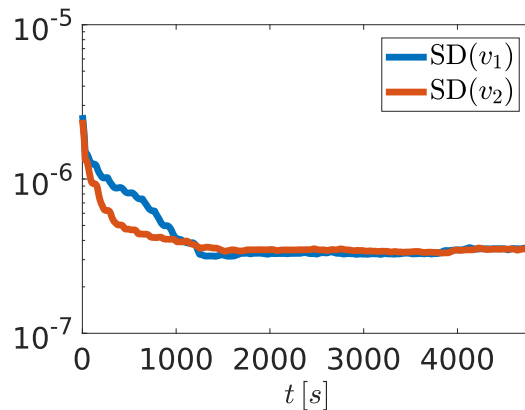


Figure 9 – The Standard Deviation $SD(v_1)$ and $SD(v_2)$ of the moving average of velocities v_1 and v_2 in two-dimensional simulation.

4.5.3 Front velocities for 1D model

In order to verify the existence of the traveling wave profile for the one-dimensional model (4.13) we simulate it directly using RCD (see 4.6.2 for details). In this case, we use finite differences as in (4.44), see the dashed line in Fig. 3. Figure 10 shows the regularized velocities v_1 and v_2 respectively using the moving average performing clustering of 250 data compared to the theoretical velocity obtained with the formula (4.40).

Figure 11 shows the standard deviation (SD) of the front velocity in each layer, which decreases in time. Significant values of $SD(v_1)$ and $SD(v_2)$ compared to $|v_i|$ at the

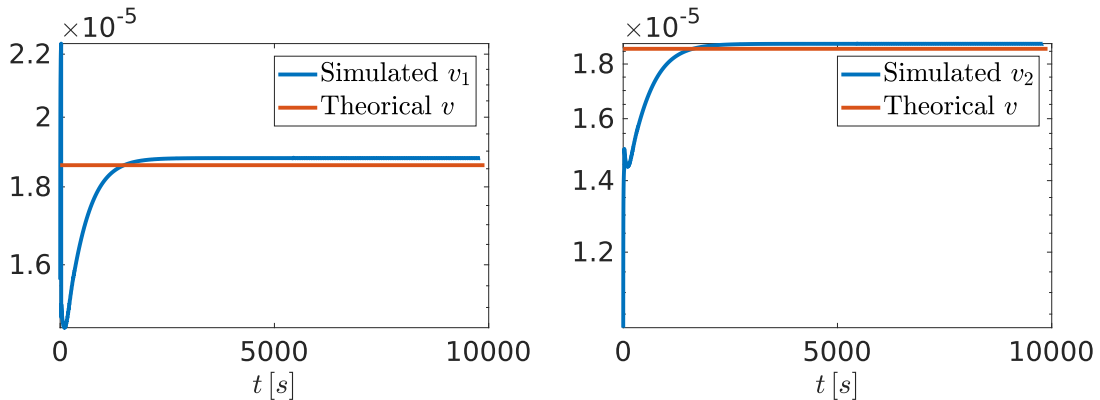


Figure 10 – Moving average of the velocities v_1 (left) and v_2 (right) of the one-dimensional model compared to the analytically estimated v from (4.40).

beginning of the simulations indicate that regularization is important to obtain high-quality measurements.

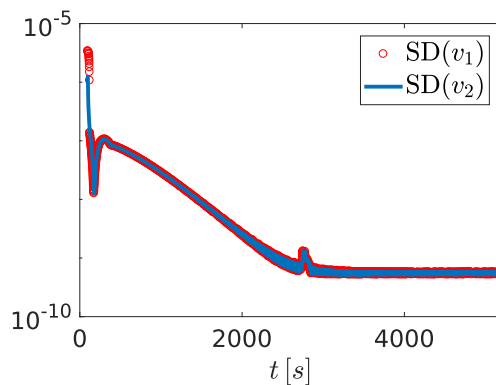


Figure 11 – The standard deviation $SD(v_1)$ and $SD(v_2)$ of the average velocities v_1 and v_2 from one-dimensional simulations.

4.5.4 Characteristic time for the traveling front stabilization

Starting with any initial conditions, it is natural to expect that the traveling wavefront takes some time to stabilize both in laboratory experiments and in computational simulations. Different phenomena influence this time; let us assume the main contribution is due to the mass exchange between layers. Assuming it is linear as in (4.13), the mass equilibrium between layers obeys exponential law with characteristic time given by the inverse of the exponent [45]. Notice that for the parameter values from Table 1, this time is $1/\theta \approx 3367\text{s}$, which is the same order of magnitude that the two-dimensional ($\approx 2500\text{s}$, see Fig. 9) and one-dimensional ($\approx 3500\text{s}$, see Fig. 11) simulations take to stabilize. Although this analysis does not apply directly to laboratory experiments, they give a rough estimate on which scale one can expect to observe the formation of stable traveling front in multiple layer reservoirs. For the parameter values from Table 1, the distance needed for the front formation is ($t_{char}u \approx 0.0049\text{m}$), which is plausible for the laboratory experiment scale.

4.5.5 Comparing front profiles

Another way to visualize and compare the front propagation in both one- and two-dimensional models are shown in Figs. 12-13, where we plot the solution profiles in layers 1 and 2, respectively. The plotted profile for the two-dimensional simulation corresponds to $d = \pm 2.5\text{mm}$ section at each layer. Because of that, there can not be an exact match between both simulations. As one can see, both profiles displace at the same traveling wave velocity, as estimated by the analysis presented in Section 4.4.

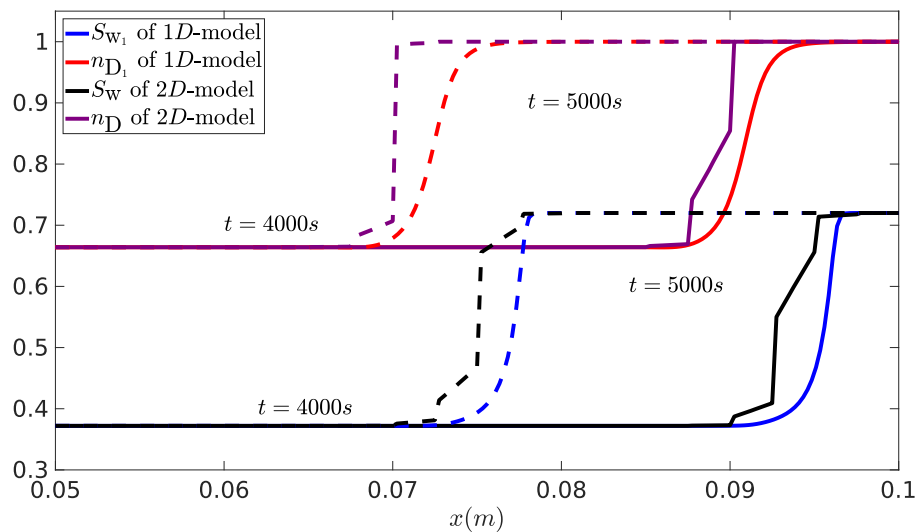


Figure 12 – Water saturation S_w and foam texture n_D profiles in the first layer, in the one-dimensional and two-dimensional models, at cross section $z = -2.5\text{mm}$. The dashed curves represent the behavior at time $t = 4000\text{s}$ and the continuous curves for $t = 5000\text{s}$.

4.6 Computational simulators and procedures

4.6.1 FOSSIL

Two-dimensional numerical simulations presented in Section 4.5.1 were obtained using Foam Displacement Simulator (FOSSIL), the in-house foam simulator developed in the Laboratory of Applied Mathematics at Federal University of Juiz de Fora (LAMAP-UFJF), whose primary goal is to be a highly extensible, reliable, and flexible software that every researcher in the laboratory could use. The main focus of the software is the simulation of multi-phase flow with foam in porous media using advanced numerical methods. The code can run simulations for problems with high heterogeneity, compressible flows, and gravitational effects.

FOSSIL's numerical methodology is based on a staggered formulation. The method splits (4.1)-(4.4) into two coupled systems: one has elliptic, and the other has a hyperbolic nature. Darcy's law directs the elliptic subsystem, where the main unknown is the

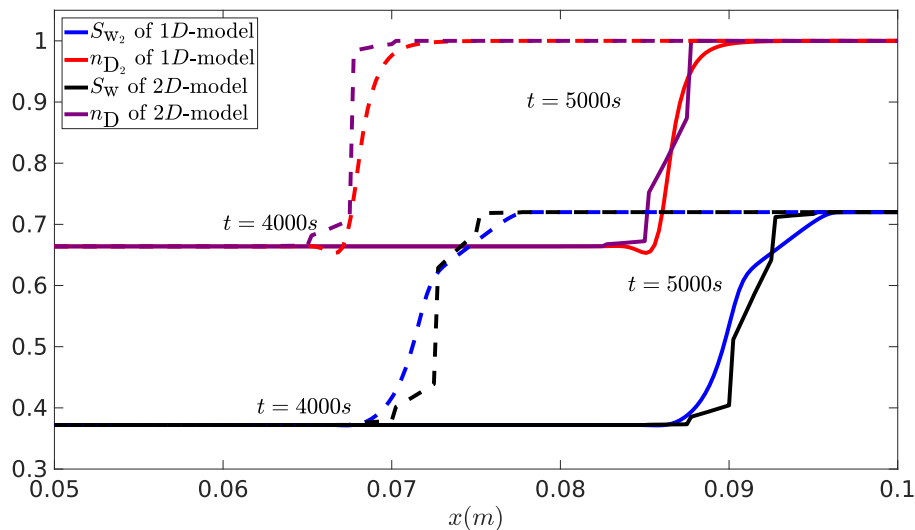


Figure 13 – Water saturation S_w and foam texture n_D profiles in the second layer, in the one-dimensional and two-dimensional models, at cross section $z = 2.5\text{mm}$. The dashed curves represent the behavior at time $t = 4000\text{s}$ and the continuous curves for $t = 5000\text{s}$.

superficial velocity u , and the remaining equations constitute the hyperbolic (or transport) subsystem. Due to this staggered methodology, one may apply two different numerical methods. A mixed hybrid finite element method [92] solves the elliptic problem, and a high-order non-oscillatory finite volume method [62] solves the transport problem. A detailed description of the solution methodology is detailed in [29]. From the computational point of view, FOSSIL is being developed on top of two open-source libraries, SUNDIALS [47] and deal.II [6].

FOSSIL uses a uniform partition of rectangles in Ω of sizes Δx and Δz , and measure approximations in time at each $t_k := k\Delta t$, for each $k \in \{0, 1, \dots, n_T\}$. At the end of the simulation, we can extract two sets of matrices $\{S_w^k\}_{k=0}^N$ and $\{n_D^k\}_{k=0}^N$, where S_w^k and n_D^k are $n_z \times n_x$ matrices, $1 \leq i \leq n_z$ and $1 \leq j \leq n_x$, approximate the average of S_w and n_D in the rectangle $K_{ij} := [(j-1)\Delta x, j\Delta x] \times [(i-1)\Delta z, i\Delta z]$ at a fixed time t_k . We choose an even n_z to have no element crossing the two layers, see Fig. 14.

4.6.2 Reaction Convection Diffusion Equations Solver

One-dimensional simulations are performed using Reaction Convection Diffusion Equations Solver (RCD). It is a C++ structured package of routines that provides a means to solve Nonlinear Balance Equation Systems numerically via finite difference methods, see [67] for details.

In order to solve the system (4.13) it was rewritten as in the following form.

$$\frac{\partial}{\partial t} G(U) + \frac{\partial}{\partial x} F(U) = \frac{\partial}{\partial x} \left(B(U) \frac{\partial U}{\partial x} \right) + R(U), \quad (4.46)$$

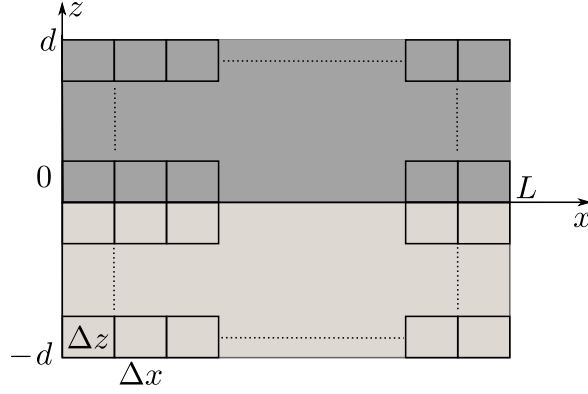
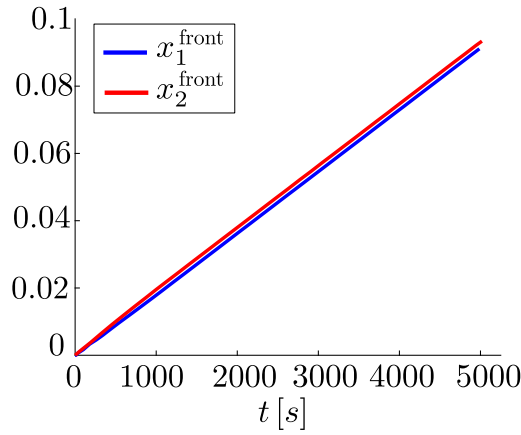


Figure 14 – Numerical domain for the two-dimensional simulation using FOSSIL.

Figure 15 – Example of front tracking vectors x_1^{front} and x_2^{front} .

where $U^T(x, t) = (S_{w_1}, n_{D_1}, S_{w_2}, n_{D_2})$ and

$$G(U) = \begin{bmatrix} \phi_1 S_{w_1} \\ \phi_1 n_{D_1} (1 - S_{w_1}) \\ \phi_2 S_{w_2} \\ \phi_2 n_{D_2} (1 - S_{w_2}) \end{bmatrix}, \quad F(U) = \begin{bmatrix} u_1 f_{w_1} \\ u_1 (1 - f_{w_1}) n_{D_1} \\ u_2 f_{w_2} \\ u_2 (1 - f_{w_2}) n_{D_2} \end{bmatrix}, \quad (4.47)$$

$$B(U) = \begin{bmatrix} -\lambda_{g_1} f_{w_1} \frac{dP_{c_1}}{dS_{w_1}} + \epsilon_{S_{w_1}} & 0 & 0 & 0 \\ n_{D_1} \lambda_{g_1} f_{w_1} \frac{dP_{c_1}}{dS_{w_1}} & \epsilon_{n_{D_1}} & 0 & 0 \\ 0 & 0 & -\lambda_{g_2} f_{w_2} \frac{dP_{c_2}}{dS_{w_2}} + \epsilon_{S_{w_2}} & 0 \\ 0 & 0 & n_{D_2} \lambda_{g_2} f_{w_2} \frac{dP_{c_2}}{dS_{w_2}} & \epsilon_{n_{D_2}} \end{bmatrix}, \quad (4.48)$$

$$R(U) = \begin{bmatrix} -\theta_{s_1} (S_{w_1} - S_{w_2}) \\ \phi_1 (1 - S_{w_1}) \Phi_1 \\ \theta_{s_2} (S_{w_1} - S_{w_2}) \\ \phi_2 (1 - S_{w_2}) \Phi_2 \end{bmatrix}. \quad (4.49)$$

The following parameters introduced small artificial diffusion improving the convergence without changing the main results: $\epsilon_{S_{w_1}} = 0$, $\epsilon_{S_{w_2}} = 0$, $\epsilon_{n_{D_1}} = 10^{-4}$, and $\epsilon_{n_{D_2}} = 10^{-4}$.

4.6.3 Post-processing the numerical solution

In order to compare one-dimensional solution profiles with two-dimensional numerical simulation, we need to track the front position in the latter. This is done by calculating the average of the front position at each horizontal strip i , see Algorithm 1. Figure 15 shows the resulting front position inside both layers for parameter values from Table 1.

Algorithm 1 Tracking the wave front

Require: $S_w^-, S_w^+, n_T > 0, n_z > 0$

Ensure: x_1^{front} and x_2^{front}

Choose a $S^* \in [S_w^-, S_w^+]$

for $k \in \{0, \dots, n_T\}$ **and** $i \in \{1, \dots, n_z\}$ **do**

if $S^* < S_{w_{i1}}^k$ **then**

$$x_{\text{strip } i}^{\text{front}} := \frac{\Delta x}{2} \frac{S^* - S_w^-}{S_{w_{i1}}^k - S_w^-}$$

else if $S_{w_{i n_x}}^k \leq S^*$ **then**

$$x_{\text{strip } i}^{\text{front}} := n_x \Delta x - \frac{\Delta x}{2} \frac{S_w^+ - S^*}{S_w^+ - S_{w_{i n_x}}^k}$$

else

 find $j \in \{1, \dots, n_x - 1\}$ such that $S_{w_{ij}}^k \leq S^* < S_{w_{i j+1}}^k$

$$x_{\text{strip } i}^{\text{front}} := \left(j - \frac{1}{2}\right) \Delta x + \Delta x \frac{S^* - S_{w_{ij}}^k}{S_{w_{i j+1}}^k - S_{w_{ij}}^k}$$

end if

$$x_{1,k}^{\text{front}} := \text{mean}_{i=1 \dots n_z/2} x_{\text{strip } i}^{\text{front}}$$

$$x_{2,k}^{\text{front}} := \text{mean}_{i=(n_z/2)+1 \dots n_z} x_{\text{strip } i}^{\text{front}}$$

end for

4.6.4 Derivation of the ODE system

In this section we derive the system of ordinary differential equations (4.29). First, we substitute (4.15) into (4.13) denoting $D_i = \lambda_{g_i} f_{g_i} dP_{c_i} / dS_{w_i}$ for $i = 1, 2$, and $\eta = x - vt$, yielding:

$$\begin{cases} -\phi_i v \frac{dS_{w_i}}{d\eta} + u_i \frac{df_{w_i}}{d\eta} = -\frac{d}{d\eta} \left(D_i \frac{dS_{w_i}}{d\eta} \right) - \theta_{s_i} (-1)^i (S_{w_1} - S_{w_2}); \\ -\phi_i v \frac{d(S_{g_i} n_{D_i})}{d\eta} + u_i \frac{d(f_{g_i} n_{D_i})}{d\eta} = \frac{d}{d\eta} \left(n_{D_i} D_i \frac{dS_{w_i}}{d\eta} \right) + \Phi_i S_{g_i} \phi_i. \end{cases} \quad (4.50)$$

In what follows, we denote $Y_i = dS_{w_i} / d\eta$ and $S = S_{w_1} - S_{w_2}$. Thus, the first equation in (4.50) can be rewritten as:

$$D_i \frac{dY_i}{d\eta} = \phi_i v Y_i - u_i \frac{\partial f_{w_i}}{\partial S_{w_i}} Y_i - u_i \frac{\partial f_{w_i}}{\partial n_{D_i}} \frac{dn_{D_i}}{d\eta} - \frac{dD_i}{d\eta} Y_i + (-1)^i \theta_{s_i} S. \quad (4.51)$$

The second equation in (4.50) can be rewritten as:

$$\begin{aligned} D_i n_{D_i} \frac{dY_i}{d\eta} &= \left[\phi_i v Y_i n_{D_i} - u_i n_{D_i} \frac{\partial f_{w_i}}{\partial S_{w_i}} - n_{D_i} \frac{dD_i}{d\eta} \right] Y_i \\ &+ \left[-\phi_i v S_{g_i} - u_i n_{D_i} \frac{\partial f_{w_i}}{\partial n_{D_i}} + u_i f_{g_i} - D_i Y_i \right] \frac{dn_{D_i}}{d\eta} + \Phi_1 S_{g_i} \phi_i. \end{aligned} \quad (4.52)$$

Multiplying (4.51) by n_{D_i} and substituting the result into (4.52) yields

$$\frac{dn_{D_i}}{d\eta} = \frac{(-1)^i \theta_{s_i} n_{D_i} S + \Phi_i S_{g_i} \phi_i}{-\phi_i v S_{g_i} + u_i f_{g_i} - D_i Y_i}. \quad (4.53)$$

Substituting (4.53) into (4.51) and using the notation

$$\Psi_i = (-1)^i \theta_{s_i} n_{D_i} S + \Phi_i S_{g_i} \phi_i, \quad F_i = -\phi_i v S_{g_i} + u_i f_{g_i} - D_i Y_i; \quad (4.54)$$

results in

$$D_i \frac{dY_i}{d\eta} = \phi_i v Y_i - u_i \frac{\partial f_{w_i}}{\partial S_{w_i}} y_i - u_i \frac{\partial f_{w_i}}{\partial n_{D_i}} \frac{\Psi}{F_i} - \frac{dD_i}{d\eta} Y_i + (-1)^i \theta_{s_i} S. \quad (4.55)$$

Applying the chain rule to $dD_i/d\eta$, we have that:

$$-\frac{dD_i}{d\eta} Y_i = -\frac{\partial D_i}{\partial S_{w_i}} Y_i^2 - \frac{\partial D_i}{\partial n_{D_i}} \frac{dn_{D_i}}{d\eta} Y_i. \quad (4.56)$$

Replacing the result into (4.55), yields

$$D_i \frac{dY_i}{d\eta} = \left[\phi_i v - u_i \frac{\partial f_{w_i}}{\partial S_{w_i}} - \frac{dD_i}{dS_{w_i}} Y_i - \frac{dD_i}{d\eta} \frac{\Psi}{F_i} \right] Y_i - u_i \frac{\partial f_{w_i}}{\partial n_{D_i}} \frac{\Psi}{F_i} + (-1)^i \theta_{s_i} S, \quad (4.57)$$

Denoting $Z_i = \phi_i v - u_i \frac{\partial f_{w_i}}{\partial S_{w_i}} - \frac{\partial D_i}{\partial S_{w_i}} Y_i - \frac{\partial D_i}{\partial n_{D_i}} \frac{\Psi_i}{F_i}$, we obtain:

$$\frac{dY_i}{d\eta} = \frac{(-1)^i \theta_{s_i} S + Z_i Y_i - u_i \frac{\partial f_{w_i}}{\partial n_{D_i}} \frac{\Psi_i}{F_i}}{D_i}. \quad (4.58)$$

The system (4.29) is composed of equations (4.53), (4.58) and $Y_i = d_\eta S_{w_i}$.

4.7 Quadratic profile

This section motivates the assumption of the quadratic shape of the water saturation profile, which is essential for the analysis presented in Section 4.3.1. We rewrite the oversimplifying water saturation equation (4.18) as

$$\frac{\partial}{\partial t}(\phi S_w) = \frac{\partial}{\partial z} \left(\epsilon \frac{\partial}{\partial z} S_w \right), \quad (4.59)$$

where we approximated capillary terms by the constant ϵ as in [75]. We assume that the water saturation profile inside the traveling wave is a linear interpolation of the equilibria. This assumption agrees with the numerical simulation results plotted in Figs. 12-13, where the water saturation presents a sharp traveling wave profile connecting two equilibria. As the traveling wave possesses a constant velocity, it means that inside the traveling wave, the time derivative of saturation for each fixed x is constant $\partial_t(S_w) = \varphi$. Substituting this approximation into (4.59) and integrating twice in z , we obtain that the water saturation can be approached as a quadratic polynomial as in (4.22).

4.8 Partial conclusions

Under some simple hypotheses, we showed that the foam displacement in two parallel layers with different permeabilities form a single traveling wavefront with velocity of when weighted average of the velocities as if both layers were isolated. These findings favor using foams as controlling agents of gas mobility in a multiple-layer porous media.

The simplified one-dimensional model was derived from the two-dimensional linear kinetic foam flow model at the cost of doubling the number of equations. The key part consisted of estimating the mass exchange coefficient between layers, using the hypothesis of parabolic front shape inspired by numerical simulations.

We verified a necessary condition for the existence of the traveling wave solution of the simplified model. We simulated this model using the Finite Difference Scheme, validating our approach. The theoretical estimates showed excellent agreement compared to numerical results obtained using the in-house code based on the staggered algorithm combining Finite Element Method and Finite Volume Method in two parallel layer configuration.

Finally, we tackled the possibility of using the proposed formula for the mass exchange between layers to estimate the time the traveling wavefront needs to stabilize, verifying its validity with numerical simulations for both one- and two-dimensional models.

5 WAVEFRONT VELOCITY FOR FOAM FLOW IN THREE-LAYER POROUS MEDIA

This chapter is a reprint of work published in CILAMCE-2022, Proceedings of the XLIII Ibero-Latin-American Congress on Computational Methods in Engineering, ABMEC [102].

In this chapter, we use a simplified bubble population balance model to describe foam displacement in porous media as this model is supported on various experimental studies [84, 118]. We approach the fractured structure of the porous medium in a three-layer configuration, where the middle layer possesses a small width and high permeability. Numerical investigation using Foam Displacement Simulator (FOSSIL) points out the existence of a stable traveling wave water saturation profile evidencing the applicability of the foam injection to control gas mobility in fractured reservoirs.

5.1 Introduction

There is a growing interest in studying the foam displacement in porous media, from an environmental (soil remediation) as shown in [11], or industrial (oil recovery) point of view as in [46]. Several models describe the behavior of foam in porous media [8], [59], [56]. Within these models are local equilibrium models and population balance models see [46]. We are interested in the latter, where the foam texture is modeled using the mass balance equation. These models are more realistic as they consider physical aspects of foam creation and destruction.

There are some studies of multiphase flow in porous media by layers; see [69], [44],[94], [19] and [61]. Some of them, i.e., [44] use Laplace transform to estimate the analytical solutions; others [61] consider fractures between the layers and study the multiphase flow when the fracture thickness tends to zero. In the case of foam displacement, one can find articles, such as [11], where artificial media with different permeabilities but the same porosity in each layer are studied for soil remediation. The behavior of multiphase flow with the presence of foam is explored in [73] in the context of microfluidics. In [95], the velocities and saturations of water in two-layer porous media with different permeabilities, but equal porosity, are analyzed from the computational point of view.

Using the linear kinetic model [8] in the previous work [104], the problem of foam flow in two-layer media is investigated using traveling waves; the velocity of this wave was found. This work proposes an extension of this study to the three-layer case using the bubble balance population foam model from [116] with simplifying hypothesis of Newtonian flow as in [111]. We use 2D simulations to show the existence of the traveling wave solution profile.

This chapter is structured as follows. Section 5.2 presents the simplified version of

the bubble population model, see [116]. In section 5.3, we describe Foam Displacement Simulator (FOSSIL) (see [29]), and the main numerical results. In section 4.8, we summarize the conclusions, highlighting the importance of the study of foam flow in porous media.

5.2 Model

Based on [29], and [104], we consider the following system of partial differential equations, which describes the two-dimensional foam displacement in porous media

$$\begin{cases} \phi \frac{\partial}{\partial t} S_w + \nabla \cdot u_w & = 0, \\ \phi \frac{\partial}{\partial t} (n_D S_g) + \nabla \cdot (u_g n_D) & = \phi S_g \Phi, \end{cases} \quad (5.1)$$

where ϕ is the porosity, S_w is the water saturation, u_w is the water velocity, n_D is the foam texture, S_g is the gas saturation, u_g is the gas velocity, and Φ represents the foam generation and coalescence. The first equation in (5.1) is a conservation law, while the second equation in (5.1) is a population balance equation considering $u = u_w + u_g$ as Darcy's velocity

$$u_w = -\lambda_w \nabla P_w, \quad (5.2)$$

where λ_w is the mobility of water phase and P_w is the pressure in the water phase. The two-dimensional domain for eq. (5.1) is the rectangle $\Omega := (0, L) \times (-d, d_3)$ (see Fig.3), where L is the maximum length in the axis x and the height z is in $(-d, d_3)$. We solve the problem in three layers of different permeability: the first $z \in (-d, d_1)$ with permeability $k = k_1$ and porosity ϕ , the second with $z \in (d_1, d_2)$ permeability $k = k_2$, porosity ϕ ; and the third with $z \in (d_2, d_3)$ $k = k_3$, porosity ϕ .

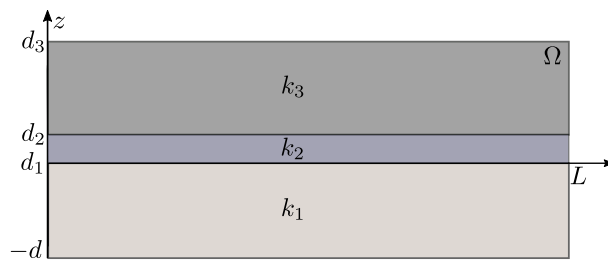


Figure 16 – Schematic representation of a three-layered porous medium as a domain $\Omega := (0, L) \times (-d, d_3)$; where, k_i is the permeabilities of the layer i , respectively.

We use the stochastic population model given in [116] with the simplification proposed in [111] to define the foam generation source term as:

$$\Phi = (K_c + K_g)(n_D^{\text{LE}} - n_D), \quad (5.3)$$

which depends on foam texture in local equilibrium $n_D^{\text{LE}}(S_w)$ given by:

$$n_D^{\text{LE}}(S_w) = \frac{K_g}{K_c + K_g}, \quad (5.4)$$

where K_g and K_c are the coalescence coefficients given in [115]. Considering the fractional flow function theory from [8], [90], [117], and [111],

$$\lambda_w = k \frac{k_{rw}}{\mu_w}, \quad \lambda_g = k \frac{k_{rg}}{\mu_g}, \quad f_w = \frac{\lambda_w}{\lambda_w + \lambda_g}, \quad f_g = \frac{\lambda_g}{\lambda_w + \lambda_g}, \quad (5.5)$$

where λ is a modified pore-size distribution parameter, λ_w and λ_g are the mobilities of water and gas phases; μ_w and μ_g are the viscosity parameters for water and gas phases, f_w and f_g are fractional flows for water and gas phases. As the system is entirely saturated we consider that $S_w + S_g = 1$ and $f_w + f_g = 1$. The relative permeabilities are:

$$k_{rw}(S_w) = \begin{cases} 0, & 0 \leq S_w \leq S_{wc}, \\ 0.75 \left(\frac{S_w - S_{wc}}{1 - S_{wc} - S_{gr}} \right)^\lambda, & S_{wc} < S_w \leq 1, \end{cases} \quad (5.6)$$

$$k_{rg}^0(S_w) = \begin{cases} 0.94 \left(\frac{1 - S_w - S_{gr}}{1 - S_{wc} - S_{gr}} \right)^{(3\lambda+2)/\lambda}, & 0 \leq S_w < 1 - S_{gr}, \\ 0, & 1 - S_{gr} \leq S_w \leq 1. \end{cases} \quad (5.7)$$

$$k_{rg}(S_w, n_D) = \frac{k_{rg}^0(S_w)}{MRF(n_D)}. \quad (5.8)$$

Here the gas mobility reduction factor is a linear function of foam texture:

$$MRF(n_D) = \beta n_{\max} n_D + 1, \quad (5.9)$$

where

$$\beta = \frac{\alpha}{(u_g/\phi S_g)^d \mu_g^0} \quad (5.10)$$

is approximated as a constant following the procedure proposed in [111] considering $S_g = 1$.

The capillary-pressure P_c is a function depending on S_w , and on the gas-water surface tension σ , on the porosity of medium ϕ and permeability k is defined as:

$$P_c = p_{c,0} \cdot \gamma \cdot \left(\frac{S_w - S_{wc}}{0.5 - S_{wc}} \right)^{-1/\lambda}, \quad (5.11)$$

considering $p_{c,0} = 2(\sigma_{gw}/r) \cos\theta$ as the entry capillarity pressure, γ is the proportionality coefficient, σ_{gw} is the surface tension between water and gas, θ is the contact angle, and r is the effective pore radius. All the parameters mentioned so here, can be seen in Table 2. The values of $n_{D_i}^-$ and $n_{D_i}^+$ are calculated using Equation (5.4).

5.3 Numerical Results

In this section, we show the results obtained for a 2D model using Foam Displacement Simulator (FOSSIL), whose detailed description can be found in [29]. To solve the

Table 2 – Parameter values for the problem of three layers.

Symbol	Value	Parameter
S_{wc}	0.1 [-]	connate water saturation
S_{gr}	0.0 [-]	residual gas saturation
μ_w	10^{-3} [Pa s]	water viscosity
μ_g^0	$2 \cdot 10^{-5}$ [Pa s]	gas viscosity in absence of foam
k_1	$1 \cdot 10^{-12}$ [m^2]	permeability of medium in layer 1
k_2	$1 \cdot 10^{-11}$ [m^2]	permeability of medium in layer 2
k_3	$1 \cdot 10^{-12}$ [m^2]	permeability of medium in layer 3
n_{max}	$2.5 \cdot 10^{11}$ [m^{-3}]	maximum foam texture
u	$2.31 \cdot 10^{-5}$ [ms^{-1}]	aweighted average total velocity
K_C	0 [s^{-1}]	bubble coalescence coefficient
K_g	0.1 [s^{-1}]	bubble generation coefficient
λ	5 [-]	pore-size distribution parameter
ϕ	0.21 [-]	porosity
S_{wi}^+	0.99[-]	inicial water saturation for the layer i , $i = 1, 2, 3$
S_{wi}^-	0.63[-]	injected water saturation for the layer i , $i = 1, 2, 3$
n_{Di}^-	1 [-]	injected foam texture for the layer i , $i = 1, 2, 3$
n_{Di}^+	1 [-]	initial foam texture for the layer i , $i = 1, 2, 3$
σ_{gw}	$30 \cdot 10^{-3}$ [N/m]	gas-water interfacial tension
α	$5.8 \cdot 10^{-16}$ [$Pa s^{2/3} m^{10/3}$]	viscosity proportionality constant
r	$5 \cdot 10^{-6}$ [m]	mean pore radius
D	0.02 [m]	constant to define the thickness of the layers

problem composed of the first equation in (5.1) and eq.(6.2), FOSSIL uses the conservative mixed finite element method proposed in [63]. To solve the second equation of (5.1) (which corresponds to the foam transport problem), FOSSIL uses the conservative method KNP introduced in [62], which is an extension of the finite volume method presented in [64].

To obtain the solutions of the problem (5.1) we use 2D simulations with the following conditions in the domain Ω (depicted in Fig. 17): At $x = 0$, we consider a constant velocity for all z , and the water saturation S_w equal to the injection condition $S_w = S_w^-$. At $x = L$, we consider the Neumann type boundary condition $\partial_x S_w = 0$. The permeability of the medium k is a matrix of dimension $m \times n_z$, where m is the number of cells on the horizontal axis, and n_z is the same on the vertical axis (we consider n_z multiple of 21). It is defined as:

$$k_{ij} = \begin{cases} k_1, & \text{if } j \in [1, (3/7)n_z] \cap \mathbb{Z}, \\ k_2, & \text{if } j \in [(10/21)n_z, (11/21)n_z] \cap \mathbb{Z}, \\ k_3, & \text{if } j \in [(4/7)n_z, n_z] \cap \mathbb{Z}. \end{cases} \quad (5.12)$$

A graphical representation of how permeability is defined over the entire domain is shown in Fig. 17, where Δz represents the cell width in z direction, Δx is the cell width in x direction. For this experiment, $|d_2 - d_3| = |-d - d_1| = D$ and $|d_2 - d_1| = (1/10)D$, where D is given in Table 4.

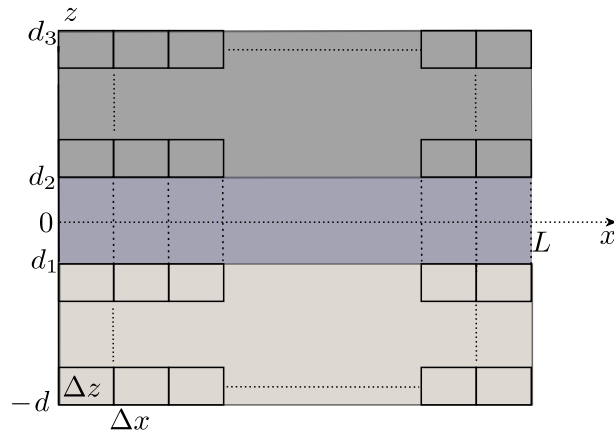


Figure 17 – Numerical domain for the three-layer problem.

Figure 18 shows the behavior of the water saturation in the whole domain at three different times. Simulation results in Fig. 18 indicate the presence of the stable traveling wave saturation profile. This behavior is similar to one described in [111] for the one-dimensional case.

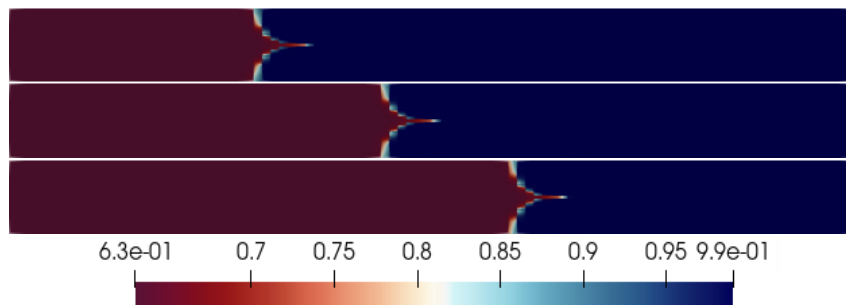


Figure 18 – Stable traveling water saturation profile obtained through two-dimensional numerical simulations at 2500 s (upper plot), 3750 s (middle plot) and 5000 s (lower plot).

To calculate the position of the water saturation wavefront, shown in Fig. 19, we modify the Algorithm 1 proposed in Section 4.6.3 given below. The position x_i^{front} with $i = 1, 2, 3$ is calculated using:

$$x_1^{front} = \text{mean}_{i=1 \dots (9/21)n_z} x_{\text{strip } i}^{front}, \quad (5.13)$$

$$x_2^{front} = \text{mean}_{i=(10/21)n_z \dots (11/21)n_z} x_{\text{strip } i}^{front}, \quad (5.14)$$

$$x_3^{front} = \text{mean}_{i=(12/21)n_z \dots n_z} x_{\text{strip } i}^{front}. \quad (5.15)$$

Using equations (5.13)-(5.15) and finite differences, we calculate the wave velocity in each layer i in a similar way as it is done in [104]:

$$v_{i,k} = \frac{x_{i,k}^{front} - x_{i,k-1}^{front}}{\Delta t}. \quad (5.16)$$

Figures 19 and 20b show that the wave in the middle layer moves faster than in the other

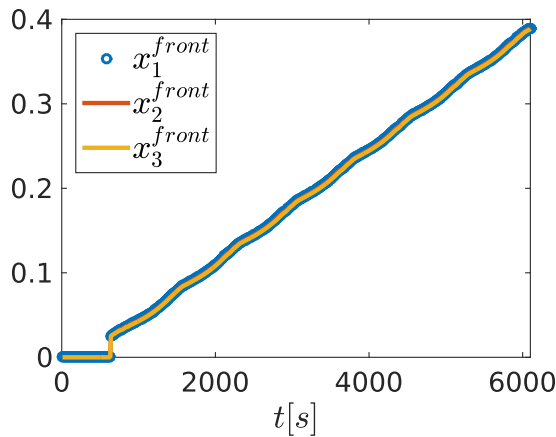
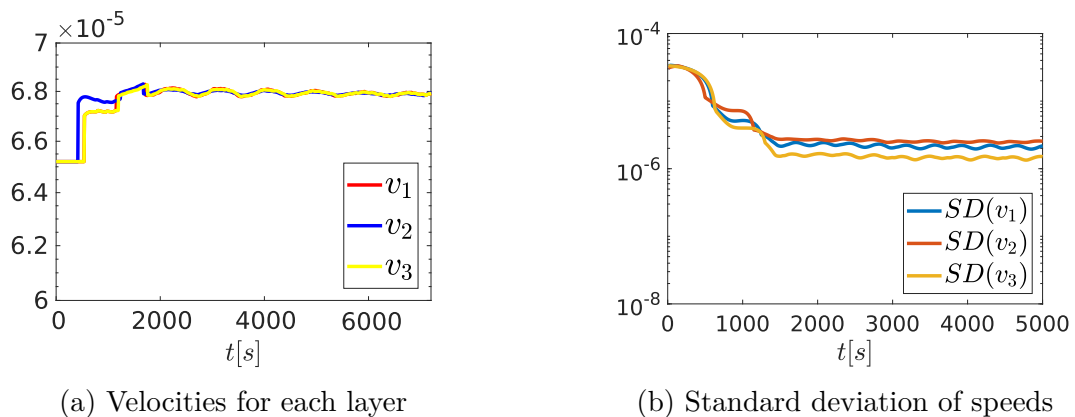


Figure 19 – Position on the horizontal axis of the water saturation front x_i^{front} in each of the i -layers.

two layers for times shorter than 2000 s. After this time, the saturation fronts move at the same velocity. Figure 21 presents saturation profiles obtained numerically at different times starting with $t = 2500$ s. In this figure, we also show the displaced initial profile comparing $S_w + v\Delta t$ with $S_w(t + \Delta t)$, where v is the stable velocity in different layers. We estimate the velocity v using the moving average with groups of 300 points obtained with a numerical approximation of the traveling wave velocity. The final value of v is the arithmetic average of the regularized velocities from $t = 3000$ s until $t = 10.000$ s. As one can observe, after the stabilization time (see Fig. 20b and 20a), the water saturation profiles move with constant velocity v without changing the wave shape.

The proximity of the curves $S_w + v\Delta t$ with $S_w(t + \Delta t)$ in Fig. 21, can be quantified using the L^2 distance, see results in Table 3. As we can observe, the distance between the profiles does not increase over time, corroborating the existence of a traveling wave solution connecting S_w^- to S_w^+ .



(a) Velocities for each layer

(b) Standard deviation of speeds

Figure 20 – Velocities v_i in the layer i ; and standard deviation of each velocity $SD(v_i)$ in the layer i . Simulated using the moving average for groups of 240 data in the 2D-model.

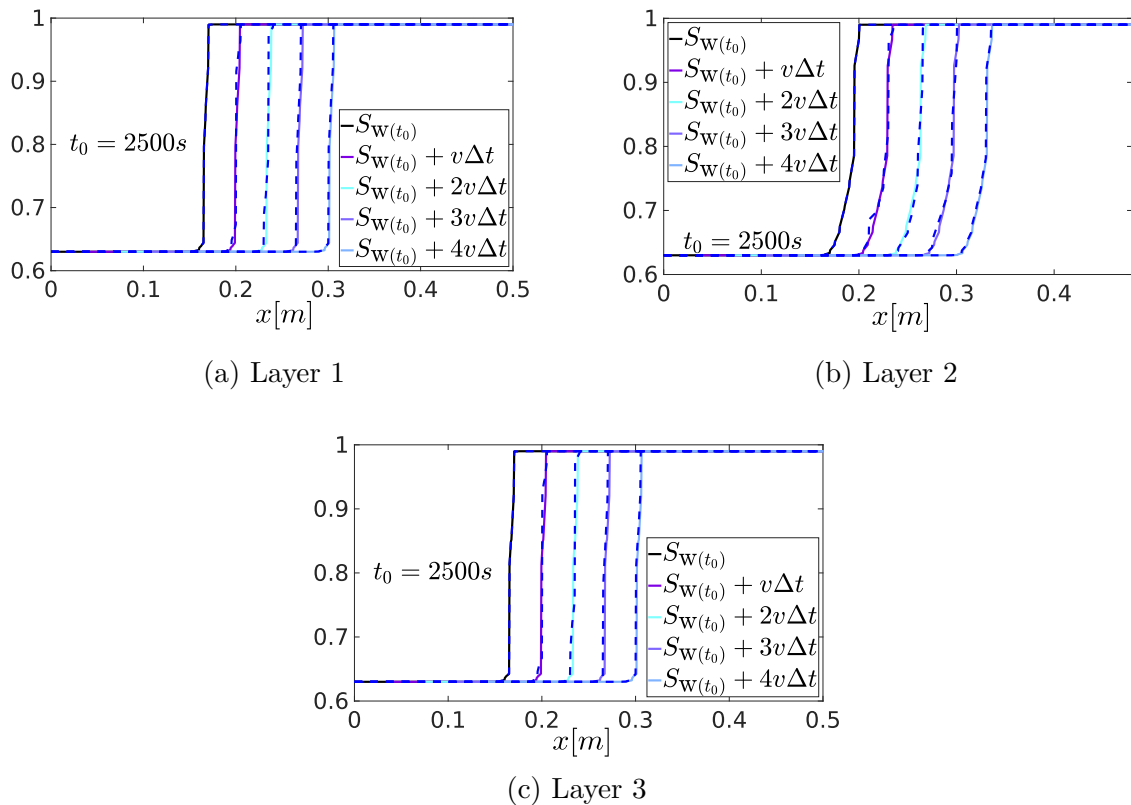


Figure 21 – Comparison of the profiles using the calculated velocity $v = 6.8e \times 10^{-5} m/s$. The dotted curves are generated by FOSSIL at times $t_0 = 2500s$, $t_1 = 3000s$, $t_2 = 3500s$, $t_3 = 4000s$, and $t_4 = 4500s$. S_{w_0} is the profile generated by FOSSIL at time 2500s. (a) In layer 1, (b) layer 2 and (c) layer 3. The distance between $S_{w_0} + v\Delta t$ and $S_w(t)$ are shown in Table 3.

Table 3 – Distance between $S_w(2500) + v\Delta t$ and $S_w(2500 + \Delta t)$ in the layer i .

Δt	Layer 1	Layer 2	Layer 3
500 s	8.3e-3	3e-3	8.3e-3
1000 s	2.02e-3	4.8e-3	2.08e-3
1500 s	1.6e-3	1.3e-3	1.7e-3
2000 s	2e-3	2.3e-3	2.02e-3

5.4 Partial conclusions

In this work, we investigated the foam displacement in three-layer stratified porous media using the bubble population model. Using the in-house numerical simulator in the two-dimensional configuration, we conclude that the water saturation profile behaves as a stable traveling wave solution. As a highly permeable middle layer can approach fracture, our results indicate that the foam displacement in the porous media containing fractures presents a behavior similar to that observed in the homogeneous case.

6 THE TRAVELING FOAM WAVEFRONT IN FRACTURED POROUS MEDIUM

This chapter is a reprint of a paper submitted in 2023 [103].

We investigate the foam injection in a fractured porous medium modeled as a thin layer surrounded by the other two. We show the formation of the single foam front using the traveling wave solution, which is characterized geometrically as a wave that moves with a constant velocity, maintaining its profile over time.

To allow this analysis, we derive a formula describing the foam front velocity in n -layered porous medium extending previously known results for two layers. All the theoretical analysis was validated through the computation simulations of the realistic model using parameter data from laboratory experiments.

6.1 Introduction

Fluid flow in porous media is a growing subject in several scientific fields involving different areas of human knowledge. For example, in environmental engineering, it is crucial for CO_2 capture and storage in both oil reservoirs and aquifers [80, 79, 97]. Other examples are related to soil remediation from subsurface contamination caused by non-aqueous liquid phases [52, 25, 46, 11, 21]. It also plays a key role in enhanced oil recovery techniques [39, 23, 97, 54, 41, 2]. One of the main challenges in this field is related to fingering formation, resulting in flow instabilities and limiting sweep efficiency, especially when dealing with gas injection. The impact of fingering is increased in the presence of fractures - a highly permeable network constituting the dominant pathway for flow in a porous medium [61, 1]. A fracture can be regarded as a part of void space in a porous medium domain with one of its dimensions being much smaller than the other two [9]. Addressing a fractured medium analytically and numerically proves to be challenging due to the domain's complex geometric shape and the fractures' relatively small thickness. Because of their thickness (or aperture), fractures are usually represented as lower dimensional objects [72]. A similar approach can be found in [38]. In [61], the authors proposed a local approach to modeling a fractured medium as a layered domain, where the fracture is treated as a layer with a smaller thickness and higher permeability than the other layers.

Over the past years, multilayered porous media were modeled in several ways [69, 44, 94, 19, 18, 61]. In [44], the authors use Laplace's transform to solve the two-phase flow in two layers. In [61], the authors utilize the ratio between porosities and absolute permeabilities of each layer to ascertain the flow behavior in the fracture, studying the water production rate considering when the fracture thickness tends to zero. Several works address the cross-flow between layers [65, 31]. In the present paper, we follow a similar approach as [61] and model the fracture as a thin porous medium layer surrounded by less

permeable layers.

One technique to control the sweep efficiency issue due to excessive gas mobility is foam injection. For example, Foam Assisted Water Alternated Gas (FAWAG) presented excellent results in Enhanced Oil Recovery [37]. This technique involves adding a surfactant solution during gas injection, which can mitigate the impact of fractures, enhance reservoir performance, improve sweep efficiency, and optimize flow dynamics in naturally fractured reservoirs [72]. In the context of multi-layered porous media, foam flow was widely studied. In [11, 83], the authors investigate foam displacement in the porous medium with two layers with different permeabilities and the same porosity aiming at soil remediation. In [73], the authors study the multi-phase foam flow using the microfluidics experimental setup. In [59, 95], the authors presented a computational analysis of the foam flow in a porous medium with two layers with different permeabilities. In [104], the authors investigate the foam flow in a two-layer medium by analytically solving the model using traveling waves. In the present work, we use the same framework to investigate the foam flow in a fractured porous medium.

Foam is an agglomeration of gas bubbles separated by a liquid film called a lamella [14]. Following [116, 8, 59, 111, 76], it can be modeled as a tracer in a gas phase described by the partial differential equation with the source term representing the foam creation and destruction [46]. In the present paper, we follow [111] and model a Newtonian foam flow based on the model proposed in [116]. Following [8, 111, 76, 26, 112] we investigate the traveling wave solutions for the foam flow in a fractured porous medium, showing the existence of a single traveling wave front in all layers. For this analysis, we extended the results from [104] from two to n layers. We presented an analytically estimated foam front velocity, which was validated by computational simulations using the two-dimensional realistic model. These simulations were carried out using FOam diSplacement SimuLator (FOSSIL) [29, 30].

The chapter is organized as follows. Section 5.2 presents the two-dimensional foam displacement model. In Section 6.3, we adapt the original model to one dimension considering n layers with different permeabilities and porosities. Section 6.4 applies the presented results to the fractured porous medium. In Section 6.5, we estimate the mass exchange coefficients between layers for the symmetric case and validate them numerically. Section 6.6 extends these results to the non-symmetric scenario. Finally, the conclusions of this work are presented in Section 6.7.

6.2 Model

In this chapter, we consider the two-phase flow of incompressible fluids, isotropic medium, and Newtonian foam as in [8, 29, 34]. The foam displacement in two dimensions is described by the water mass conservation law, the foam population balance equation,

Darcy's law, and the incompressibility condition:

$$\left\{ \begin{array}{l} \phi \frac{\partial}{\partial t} S_w + \nabla \cdot u_w = 0, \\ \phi \frac{\partial}{\partial t} (n_D S_g) + \nabla \cdot (u_g n_D) = \phi S_g \Phi, \\ u = -k \lambda \nabla P; \\ \nabla \cdot u = 0, \end{array} \right. \quad (6.1)$$

with variables $S_w(x, z, t)$ [\cdot] and $S_g(x, z, t)$ [\cdot] representing the water/gas saturations, and $n_D(x, z, t)$ [\cdot] is the dimensionless foam texture (number of bubbles per volume). Here ϕ [\cdot] is the porosity, u_w [m/s] is the water velocity, u_g [m/s] is the gas velocity, $u = u_w + u_g$, [m/s] is the total velocity, k [m²] is the absolute permeability, λ [m²(Pa·s)⁻¹] is the total mobility, P [Pa] is the total pressure (considered as the sum of all pressures [27]), and Φ is foam generation source term.

The system is saturated, *i.e.*, $S_w + S_g = 1$. The water phase velocity is given by

$$u_w = u f_w + \lambda_g f_w \nabla P_c, \quad (6.2)$$

where f_w [\cdot] is the water fractional flow function, λ_g [m²(Pa·s)⁻¹] is the gas phase mobility, and P_w [Pa] is the water phase pressure. Functions f_w , λ_g , and P_c are defined below. The two-dimensional domain for (6.1) is the rectangle $\Omega = [0, L] \times [0, D]$, where $D = d_1 + d_2 + \dots + d_n$, is the total domain thickness, $d_i \in \mathbb{R}^+$ represents the thickness of the layer i , and the length of the x -axis is L , see Fig. 22. The foam generation source term Φ is defined following [116] as

$$\Phi = (K_c + K_g)(n_D^{\text{LE}} - n_D), \quad (6.3)$$

where the foam texture in local equilibrium is

$$n_D^{\text{LE}}(S_w) = \frac{K_g}{K_c + K_g}, \quad (6.4)$$

K_g and K_c are the foam generation and coalescence coefficients.

To complete the model (6.1) we use the standard fractional flow theory [9, 27, 66] and define the relative mobilities of water and gas (λ_w and λ_g , $\lambda = \lambda_w + \lambda_g$) and fractional flow functions of water and gas (f_w and f_g) as

$$\lambda_w = k \frac{k_{rw}}{\mu_w}, \quad \lambda_g = k \frac{k_{rg}}{\mu_g}, \quad f_w = \frac{\lambda_w}{\lambda_w + \lambda_g}, \quad f_g = \frac{\lambda_g}{\lambda_w + \lambda_g}, \quad (6.5)$$

where μ_w and μ_g [Pa·s] are the viscosity parameters for water and gas phases. The water and gas relative permeabilities (k_{rw} and k_{rg}^0) are defined as in [98]:

$$k_{rw}(S_w) = \begin{cases} 0, & 0 \leq S_{wi} \leq S_{wc}, \\ 0.75 \left(\frac{S_w - S_{wc}}{1 - S_{wc} - S_{gr}} \right)^\xi, & S_{wc} < S_w \leq 1, \end{cases} \quad (6.6)$$

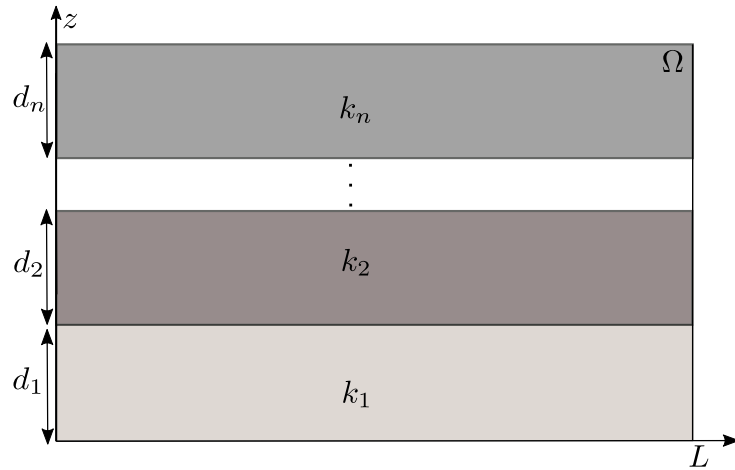


Figure 22 – Schematic representation of a n-layered porous media.

$$k_{\text{rg}}^0(S_w) = \begin{cases} 1 \left(\frac{1 - S_w - S_{\text{gr}}}{1 - S_{\text{wc}} - S_{\text{gr}}} \right)^{(3\xi+2)/\xi}, & 0 \leq S_w < 1 - S_{\text{gr}}, \\ 0, & 1 - S_{\text{gr}} \leq S_w \leq 1, \end{cases} \quad (6.7)$$

where ξ is a modified pore-size distribution parameter. The foamed gas relative permeability is:

$$k_{\text{rg}}(S_w, n_D) = \frac{k_{\text{rg}}^0(S_w)}{MRF(n_D)}, \quad (6.8)$$

where the gas mobility reduction factor (MRF) can be approximated as a linear function of foam texture [8, 111]:

$$MRF(n_D) = \beta n_{\text{max}} n_D + 1, \quad (6.9)$$

n_{max} [m^{-3}] is the maximum foam texture, β [\cdot] is proportionally coefficient.

The capillary pressure P_c [Pa] is a function of water saturation S_w as in [98]:

$$P_c = p_{c,0} \cdot \gamma \cdot \left(\frac{S_w - S_{\text{wc}}}{0.5 - S_{\text{wc}}} \right)^{-1/\xi}, \quad (6.10)$$

where $p_{c,0} = 2(\sigma_{gw}/r) \cos \theta$ is the entry capillarity pressure, γ is the proportionality coefficient, σ_{gw} is the surface tension between water and gas, θ is the contact angle, and r is the effective pore radius. Table 4 contains all parameter values used in this work.

6.3 Foam flow in n-layers

In this section, we simplify the model (6.1) to one dimension at the cost of increasing the number of equations to $2n$. This simplification allows us to investigate the traveling wave solution and estimate its velocity. In this sense, the present study extends the analysis presented in [104] to n layers.

Table 4 – Parameters values [98, 111].

Symbol	Value	Parameter
S_{wc}	0.2 [-]	connate water saturation
S_{gr}	0.0 [-]	residual gas saturation
μ_w	10^{-3} [Pa s]	water viscosity
μ_g	$2 \cdot 10^{-5}$ [Pa s]	gas viscosity in absence of foam
K_c	0 [s ⁻¹]	bubble coalescence coefficient
K_g	0.1 [s ⁻¹]	bubble generation coefficient
ξ	5 [-]	pore-size distribution parameter
ϕ	0.21 [-]	porosity
$S_{w_i}^+$	0.99[-]	initial water saturation for the layer i
$S_{w_i}^-$	0.63[-]	injected water saturation for the layer i
$n_{D_i}^-$	1 [-]	injected foam texture for the layer i
$n_{D_i}^+$	1 [-]	initial foam texture for the layer i
σ_{gm}	$30 \cdot 10^{-3}$ [N/m]	gas-water interfacial tension
θ	0 [rad]	contact angle
r	$5 \cdot 10^{-6}$ [m]	mean pore radius
β	$7.8185 \cdot 10^{-10}$ [-]	model mobility parameter
u_{w_1}	$1.446 \cdot 10^{-6}$ [ms ⁻¹]	water surface velocity in layer 1
u_{g_1}	$1.471 \cdot 10^{-5}$ [ms ⁻¹]	gas surface velocity in layer 1
c	1/20	factor for calculating fracture thickness

6.3.1 One-dimensional multi-layer simplification

Consider the domain Ω shown in Fig. 22. Assuming a constant pressure gradient as in [26, 11], we can presume that the total velocity in each layer remains constant. Consequently, the last two equations of the system (6.1) can be omitted. Thus, the system (6.1) can be expressed as a one-dimensional system of $2n$ Partial Differential Equations (**PDE**):

$$\left\{ \begin{array}{l} \phi_1 \frac{\partial}{\partial t} S_{w_1} + \frac{\partial}{\partial x} u_{w_1} = -\theta_{1\downarrow}(\phi_1 S_{w_1} - \phi_2 S_{w_2}), \\ \vdots \\ \phi_i \frac{\partial}{\partial t} S_{w_i} + \frac{\partial}{\partial x} u_{w_i} = \theta_{i\uparrow}(\phi_{i-1} S_{w_{i-1}} - \phi_i S_{w_i}) - \theta_{i\downarrow}(\phi_i S_{w_i} - \phi_{i+1} S_{w_{i+1}}), \\ \vdots \\ \phi_n \frac{\partial}{\partial t} S_{w_n} + \frac{\partial}{\partial x} u_{w_n} = \theta_{n\uparrow}(\phi_{n-1} S_{w_{n-1}} - \phi_n S_{w_n}), \\ \phi_i \frac{\partial}{\partial t} n_{D_i} S_{g_i} + \frac{\partial}{\partial x} u_{g_i} n_{D_i} = \phi_i S_{g_i} \Phi_i, \quad \text{for } i \in \{1, 2, \dots, n\}. \end{array} \right. \quad (6.11)$$

The first n equations in (6.11) represent the water mass balance in each layer, while the last n equations represent the foam texture population balance. In each Layer i , the porosity is denoted as ϕ_i , and Darcy's velocities are expressed as u_{w_i} for the water phase and u_{g_i} for the gas phase. The total velocity u_i , is given by $u_i = u_{w_i} + u_{g_i}$, which remains constant in each layer calculated using each layer's absolute permeability k_i and the same relative permeability as in (6.6)-(6.8). The coefficients $\theta_{i\uparrow}$ and $\theta_{i\downarrow}$ represent the mass

transfer from Layer i to the previous and next layers, relating one- and two-dimensional models. Variables S_{w_i} , S_{g_i} , and n_{D_i} denote the water/gas mean saturations and foam texture.

We study system (6.11) as a Riemann problem, *i.e.*, a problem with the initial conditions in the form of a step function:

$$(S_{w_1}, \dots, S_{w_n}, n_{D_1}, \dots, n_{D_n})(x, 0) = \begin{cases} (S_{w_1}^-, \dots, S_{w_n}^-, n_{D_1}^-, \dots, n_{D_n}^-), & x < 0, \\ (S_{w_1}^+, \dots, S_{w_n}^+, n_{D_1}^+, \dots, n_{D_n}^+), & x > 0. \end{cases} \quad (6.12)$$

The superscripts “ $-$ ” and “ $+$ ” mean the left and right states, which are constant values for each i . The values of $n_{D_i}^-$ and $n_{D_i}^+$ are calculated using Equation (6.4) and are reported in Table 4.

6.3.2 Traveling wave velocity

The PDE solution in the form of a traveling wave maintains its profile over time, displacing it with constant velocity. Mathematically, it can be defined in terms of the traveling variable $\eta = x - vt$ as follows; for more details, see [106, 40].

Definition 6.3.1. A solution $(S_{w_1}, \dots, S_{w_n}, n_{D_1}, \dots, n_{D_n})$ of system (6.11) is a traveling wave if it can be written as

$$S_{w_i}(x, t) = \widehat{S}_{w_i}(\eta), \quad n_{D_i}(x, t) = \widehat{n}_{D_i}(\eta), \quad (6.13)$$

where $\eta = x - vt$ ($v \in \mathbb{R}$), and there exist a left state $(S_{w_1}^-, \dots, S_{w_n}^-, n_{D_1}^-, \dots, n_{D_n}^-) \in \mathbb{R}^{2n}$ and a right state $(S_{w_1}^+, \dots, S_{w_n}^+, n_{D_1}^+, \dots, n_{D_n}^+) \in \mathbb{R}^{2n}$, such that

$$\lim_{\eta \rightarrow \pm\infty} \widehat{S}_{w_i}(\eta) = S_{w_i}^\pm, \quad \lim_{\eta \rightarrow \pm\infty} \widehat{n}_{D_i}(\eta) = n_{D_i}^\pm. \quad (6.14)$$

In this case, the limit states $(S_{w_1}^\pm, \dots, S_{w_n}^\pm, n_{D_1}^\pm, \dots, n_{D_n}^\pm)$ of the Riemann problem are α - and ω -limits of the corresponding dynamical system [106, 40, 43]. In what follows, we abuse the notation and omit hats over the variables.

Substituting the expressions (6.13) and (6.14) into Eq. (6.11), considering capillary pressure P_{c_i} as in (6.10) in each layer i , and total superficial velocity of layer i as u_i for $i = 1, 2, \dots, n$ we obtain the following ODE system:

$$\begin{cases} -\phi_1 v \frac{dS_{w_1}}{d\eta} + u_1 \frac{df_{w_1}}{d\eta} & = -\frac{d}{d\eta} \left[B_1 \frac{dS_{w_1}}{d\eta} \right] - \theta_{1\downarrow} \mathcal{D}_1, \\ & \vdots \\ -\phi_i v \frac{dS_{w_i}}{d\eta} + u_i \frac{df_{w_i}}{d\eta} & = -\frac{d}{d\eta} \left[B_i \frac{dS_{w_i}}{d\eta} \right] + \theta_{i\uparrow} \mathcal{D}_{i-1} - \theta_{i\downarrow} \mathcal{D}_i, \\ & \vdots \\ -\phi_n v \frac{dS_{w_n}}{d\eta} + u_n \frac{df_{w_n}}{d\eta} & = -\frac{d}{d\eta} \left[B_n \frac{dS_{w_n}}{d\eta} \right] + \theta_{n\uparrow} \mathcal{D}_{n-1}, \\ -\phi_i v \frac{d(n_{D_i} S_{g_i})}{d\eta} + u_n \frac{d(f_{g_i} n_{D_i})}{d\eta} & = \frac{d}{d\eta} \left[n_{D_i} B_i \frac{dS_{w_i}}{d\eta} \right] + \mathcal{R}_i, \quad i = 1, \dots, n. \end{cases} \quad (6.15)$$

$$B_i = \left(\lambda_{g_i} f_{w_i} \frac{dP_{c_i}}{dS_{w_i}} \right), \quad \mathcal{R}_i = \phi_i S_{g_i} \Phi_i, \quad \text{for } i = 1, 2, \dots, n. \quad (6.16)$$

$$\mathcal{D}_{i-1} = (\phi_{i-1} S_{w_{i-1}} - \phi_i S_{w_i}), \quad \text{for } i = 2, 3, \dots, n. \quad (6.17)$$

Proposition 6.3.1. *Considering $(S_{w_1}, \dots, S_{w_n}, n_{D_1}, \dots, n_{D_n})$ the solution of system (6.15) with $n \geq 3$, then*

$$\frac{E_n}{\theta_{n\uparrow}} = -\frac{E_{n-1}}{\theta_{(n-1)\downarrow}} - \sum_{i=1}^{n-2} \left(\theta_{i\downarrow}^{-1} \prod_{j>i}^{n-1} \theta_{j\uparrow} \theta_{j\downarrow}^{-1} \right) E_i, \quad (6.18)$$

where

$$E_i = -\phi_i v \frac{d}{d\eta} S_{w_i} + \frac{d}{d\eta} u_i f_{w_i} + \frac{d}{d\eta} \left(\lambda_{g_i} f_{w_i} \frac{dP_{c_i}}{dS_{w_i}} \frac{dS_{w_i}}{d\eta} \right), \quad i = 1, 2, \dots, n. \quad (6.19)$$

Remark 6.3.1. Notice that Proposition 6.3.1 is only valid for $n \geq 3$ since there are two mass transfer coefficients, $\theta_{i\uparrow}$ and $\theta_{i\downarrow}$, for $i = 2, \dots, n-1$. However, Proposition 6.3.1 is still valid for $n = 2$ replacing Eq. (6.18) by:

$$\frac{E_2}{\theta_{2\uparrow}} = -\frac{E_1}{\theta_{1\uparrow}}, \quad (6.20)$$

as shown in [104].

Proof of Proposition 6.3.1. The proof uses the principle of mathematical induction [99].

- In the first step, we show that (6.18) is satisfied for $m = 3$. In this case we use (6.19) and rewrite the system (6.15) as:

$$E_1 = -\theta_{1\downarrow} \mathcal{D}_1; \quad (6.21)$$

$$E_2 = \theta_{2\uparrow} \mathcal{D}_1 - \theta_{2\downarrow} \mathcal{D}_2; \quad (6.22)$$

$$E_3 = \theta_{3\uparrow} \mathcal{D}_2. \quad (6.23)$$

Substituting \mathcal{D}_1 and \mathcal{D}_2 into (6.22), we obtain:

$$\frac{E_3}{\theta_{3\uparrow}} = -\frac{E_2}{\theta_{2\downarrow}} - \frac{\theta_{2\uparrow} E_1}{\theta_{1\downarrow} \theta_{2\downarrow}}. \quad (6.24)$$

- In the next step, assuming (6.18) is satisfied for $m = n$, we prove that (6.18) is valid for $m = n + 1$. For $m = n$, the system (6.15) can be rewritten as:

$$E_1 = -\theta_{1\downarrow} \mathcal{D}_1; \quad (6.25)$$

$$E_2 = \theta_{2\uparrow} \mathcal{D}_1 - \theta_{2\downarrow} \mathcal{D}_2; \quad (6.26)$$

⋮

$$E_{n-1} = \theta_{(n-1)\uparrow} \mathcal{D}_{n-2} - \theta_{(n-1)\downarrow} \mathcal{D}_{n-1}; \quad (6.27)$$

$$E_n = \theta_{n\uparrow} \mathcal{D}_{n-1}. \quad (6.28)$$

Using Eqs. (6.25)-(6.27), we obtain for $j = 1, \dots, n-2$,

$$\mathcal{D}_{n-j} = \frac{-E_{n-j}}{\theta_{(n-j)\downarrow}} + \frac{\theta_{(n-j)\uparrow}}{\theta_{(n-j)\downarrow}} \mathcal{D}_{n-j-1}. \quad (6.29)$$

Thus, \mathcal{D}_{n-1} can be written recursively, using all values of j , as follows:

$$\mathcal{D}_{n-1} = \frac{-E_{n-1}}{\theta_{(n-1)\downarrow}} - \sum_{i=1}^{n-2} \left(\theta_{i\downarrow}^{-1} \prod_{j>i}^{n-1} \theta_{j\uparrow} \theta_{j\downarrow}^{-1} \right) E_i. \quad (6.30)$$

Replacing (6.30) into (6.28), we obtain

$$\frac{E_n}{\theta_{n\uparrow}} = -\frac{E_{n-1}}{\theta_{(n-1)\downarrow}} - \sum_{i=1}^{n-2} \left(\theta_{i\downarrow}^{-1} \prod_{j>i}^{n-1} \theta_{j\uparrow} \theta_{j\downarrow}^{-1} \right) E_i. \quad (6.31)$$

Now, let us prove (6.18) is valid for $m = n+1$. In this case, the expressions E_i are given by:

$$E_1 = -\theta_{1\downarrow} \mathcal{D}_1; \quad (6.32)$$

⋮

$$E_{n-1} = \theta_{(n-1)\uparrow} \mathcal{D}_{n-2} - \theta_{(n-1)\downarrow} \mathcal{D}_{n-1}; \quad (6.33)$$

$$E_n = \theta_{n\uparrow} \mathcal{D}_{n-1} - \theta_{n\downarrow} \mathcal{D}_n; \quad (6.34)$$

$$E_{n+1} = \theta_{(n+1)\uparrow} \mathcal{D}_n. \quad (6.35)$$

Proceeding as in Eq. (6.30), for $j = 1, \dots, n-1$, we obtain

$$\mathcal{D}_n = \frac{-E_n}{\theta_{n\downarrow}} - \sum_{i=1}^{n-1} \left(\theta_{i\downarrow}^{-1} \prod_{j>i}^n \theta_{j\uparrow} \theta_{j\downarrow}^{-1} \right) E_i. \quad (6.36)$$

Replacing (6.36) into (6.35) and dividing by $\theta_{(n+1)\uparrow}$, we obtain

$$\frac{E_{n+1}}{\theta_{(n+1)\uparrow}} = -\frac{E_n}{\theta_{n\downarrow}} - \sum_{i=1}^{n-1} \left(\theta_{i\downarrow}^{-1} \prod_{j>i}^n \theta_{j\uparrow} \theta_{j\downarrow}^{-1} \right) E_i. \quad (6.37)$$

This allows us to conclude that (6.18) is satisfied for $m = n+1$. We have proved that (6.18) is valid for all $m \geq 3$.

□

Proposition 6.3.2. *Considering $(S_{w_1}, \dots, S_{w_n}, n_{D_1}, \dots, n_{D_n})$ the solution of system (6.15) with $n \geq 3$ and v is the traveling wave velocity then,*

$$v = \frac{a_n \prod_{j=1}^{n-1} \theta_{j\downarrow} + \theta_{n\uparrow} a_{n-1} \prod_{j=1}^{n-2} \theta_{j\downarrow} + \sum_{i=1}^{n-2} \left(\prod_{j>i}^n \theta_{j\uparrow} \right) \rho_i a_i}{b_n \prod_{j=1}^{n-1} \theta_{j\downarrow} + \theta_{n\uparrow} b_{n-1} \prod_{j=1}^{n-2} \theta_{j\downarrow} + \sum_{i=1}^{n-2} \left(\prod_{j>i}^n \theta_{j\uparrow} \right) \rho_i b_i}, \quad (6.38)$$

where

$$a_i = u_i (f_{w_i}^+ - f_{w_i}^-), \quad b_i = \phi_i (S_{w_i}^+ - S_{w_i}^-), \quad f_{w_i}^\pm = f_{w_i}(S_{w_i}^\pm, n_{D_i}^\pm) \quad (6.39)$$

and

$$\rho_i = \begin{cases} \prod_{j=1}^{i-1} \theta_{j\downarrow}, & \text{if } i > 1, \\ 1, & \text{if } i \leq 1. \end{cases} \quad (6.40)$$

Proof. Considering E_i as in (6.19) from Proposition 6.3.1, we define

$$\bar{E}_i = \int_{-\infty}^{\infty} E_i d\eta = -\phi_i v S_{w_i}^+ + u_i f_{w_i}^+ + \phi_i v S_{w_i}^- - u_i f_{w_i}^- = -v b_i + a_i, \quad (6.41)$$

where we used (6.39), and $i = 1, 2, \dots, n$. Integrate (6.18) in η and substitute (6.41) for E_n, E_{n-1} , and E_i . Isolating v yields

$$v = \frac{\frac{a_n}{\theta_{n\uparrow}} + \frac{a_{n-1}}{\theta_{(n-1)\downarrow}} + \sum_{i=1}^{n-2} \left(\theta_{i\downarrow}^{-1} \prod_{j>i}^{n-1} \theta_{j\uparrow} \theta_{j\downarrow}^{-1} \right) a_i}{\frac{b_n}{\theta_{n\uparrow}} + \frac{b_{n-1}}{\theta_{(n-1)\downarrow}} + \sum_{i=1}^{n-2} \left(\theta_{i\downarrow}^{-1} \prod_{j>i}^{n-1} \theta_{j\uparrow} \theta_{j\downarrow}^{-1} \right) b_i}. \quad (6.42)$$

Multiplying the numerator and the denominator in (6.42) by $\prod_{j=1}^n \theta_{j\downarrow}$ we obtain (6.38). \square

Remark 6.3.2. In the particular case of equal mass exchange coefficients ($\theta_{i\downarrow} = \theta_{i\uparrow} = \theta_{j\uparrow} = \theta_{j\downarrow}$, $\forall i, j$), it is possible to simplify Eq. (6.38) by canceling all exchange coefficients in (6.38). In this case, the velocity v can be expressed as a weighted mean of velocities v_i :

$$v = \left(\sum_{i=1}^n a_i v_i \right) \left(\sum_{i=1}^n a_i \right)^{-1} = \frac{a_1 v_1 + \dots + a_n v_n}{a_1 + \dots + a_n}, \quad (6.43)$$

where a_i are given in (6.39), and v_i is the traveling wave velocity in isolated layer i obtained from the system (6.11) without mass exchange ($\theta_{i\uparrow} = \theta_{i\downarrow} = 0$):

$$v_i = \frac{u_i}{\phi_i} \frac{f_{w_i}^+ - f_{w_i}^-}{S_{w_i}^+ - S_{w_i}^-}. \quad (6.44)$$

6.4 Application of the presented analysis to foam flow in the fractured porous medium.

To illustrate the application of the presented analysis, we investigate the propagation of the foam flow in a fractured porous medium regarded as a three-layered matrix with a thin middle layer, see Fig. 23. Generally, estimating the mass exchange coefficients $\theta_{i\uparrow}$ and $\theta_{i\downarrow}$ between layers is challenging. In [104], this is done for a two-layer porous medium. In what follows, we estimate these coefficients for a fracture case.

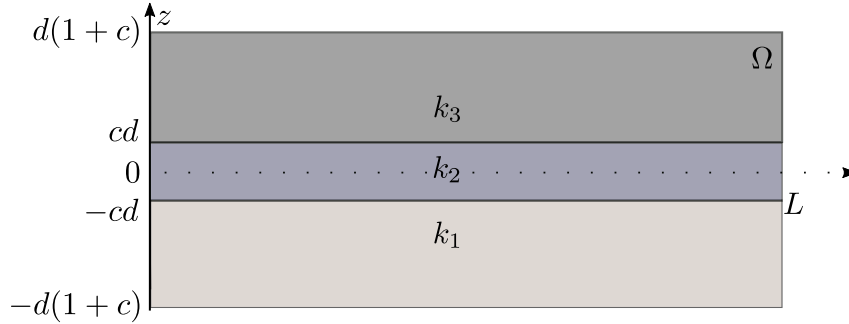


Figure 23 – Schematic representation of a three-layered porous medium as a rectangular domain Ω ; where, $c \in (0, 1)$ is constant, and k_i is the permeability of the layer i .

For a three-layered porous medium, the traveling wave velocity (6.38) can be written in a simplified way

$$v = \frac{\theta_{1\downarrow}\theta_{2\downarrow}a_3 + \theta_{1\downarrow}\theta_{3\uparrow}a_2 + \theta_{2\uparrow}\theta_{3\uparrow}a_1}{\theta_{1\downarrow}\theta_{2\downarrow}b_3 + \theta_{1\downarrow}\theta_{3\uparrow}b_2 + \theta_{2\uparrow}\theta_{3\uparrow}b_1}. \quad (6.45)$$

Next, we present two cases of a fractured porous medium represented in Fig. 23. The **symmetric case** considers the first and last layers with equal permeabilities; see Table 5. It is more straightforward to understand, and it corresponds to equal mass exchange coefficients. The **non-symmetric case** considers different permeabilities; see Table 5. Both cases consider the same porosity in all layers; see Table 4.

Table 5 – Absolute permeabilities for each of the three layers considered in this study.

Case	k_1	k_2	k_3
Symmetric	$1 \times 10^{-12} [m^2]$	$1 \times 10^{-11} [m^2]$	$1 \times 10^{-12} [m^2]$
Non-symmetric	$1 \times 10^{-12} [m^2]$	$1 \times 10^{-11} [m^2]$	$2 \times 10^{-12} [m^2]$

From the third equation of the system (6.1), we know that the total velocity of the flow in each layer i ($u_i = u_{w_i} + u_{g_i}$) is proportional to the absolute permeabilities of each layer. Since we aim to address a fractured porous medium, it is considered that the middle layer has a higher absolute permeability than the adjacent layers. Therefore, we use the values of absolute permeability in each layer as in Table 5 to calculate u_2 and u_3 based on the value of u_1 . In the symmetric case, $u_2 = 10u_1$, and $u_3 = u_1$. In the non-symmetric case, $u_2 = 10u_1$, and $u_3 = 2u_1$.

6.5 Symmetric foam front in fractured porous medium

To estimate the mass exchange coefficients $\theta_{1\downarrow}$, $\theta_{2\uparrow}$, $\theta_{2\downarrow}$, and $\theta_{3\uparrow}$ of the one-dimensional model (6.11) for $n = 3$ we follow the same procedure as in [104] detailed below. Similarly to the assumption in [104], we consider S_w to be a piece-wise quadratic function of z , symmetric with respect to the origin; see Fig. 24. It is also possible to observe this

piece-wise quadratic profile in simulations presented in Section 4.6.1. The considered water saturation is

$$S_w(z) = \begin{cases} \gamma_1 z^2 + \delta_1 z + \tau_1 & \text{in layer 1,} \\ \gamma_2 z^2 + \delta_2 z + \tau_2 & \text{in layer 2,} \\ \gamma_3 z^2 + \delta_3 z + \tau_3 & \text{in layer 3,} \end{cases} \quad (6.46)$$

with $\gamma_i, \delta_i, \tau_i$ constants for $i = 1, 2, 3$. We assume that the representative mean water saturation in each layer is given by

$$S_{w_1} = \frac{1}{d} \int_{-d(1+c)}^{-cd} S_w(z) dz, \quad S_{w_2} = \frac{1}{cd} \int_{-cd}^0 S_w(z) dz, \quad S_{w_3} = S_{w_1}, \quad (6.47)$$

see Fig 24.

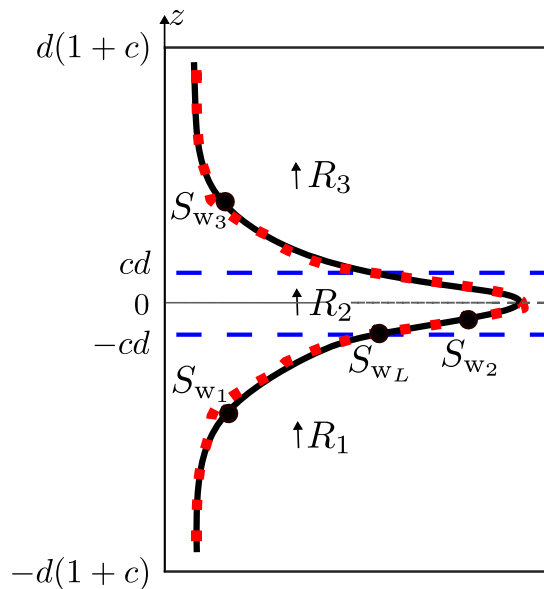


Figure 24 – Schematic representation of the water saturation S_w along the vertical cross-section of the three-layered porous medium, where $c \in (0, 1)$ is constant. The dotted red curve represents the cross-section of S_w calculated at $t = 5000$ s in the 2D simulations. The continuous black curve S_w is a quadratic approximation, symmetric with respect to the line $z = 0$. Coefficients R_i represent the total mass variation in each layer i , S_{w_L} is the saturation value at the interface, and S_{w_i} is the average value in each region of the domain i with permeability k_i .

Assuming that there is no water loss at the reservoir's edges and from the symmetry of $S_w(z)$, we obtain

$$\left. \frac{dS_w}{dz} \right|_{z=\pm d(1+c)} = 0, \quad \text{and} \quad \left. \frac{dS_w}{dz} \right|_{z=0} = 0. \quad (6.48)$$

The continuity of $S_w(z)$ function within $(-d(1+c), d(1+c))$ is guaranteed by the lateral limits (see Fig. 24)

$$\lim_{z \rightarrow -cd^-} S_w(z) = \lim_{z \rightarrow -cd^+} S_w(z) = S_{w_L}. \quad (6.49)$$

Substituting (6.46) into (6.47), we obtain that

$$S_{w_1} = \gamma_1 d^2 \left[\frac{2}{3} - 2c - 3c^2 \right] + \tau_1 \quad \text{and} \quad S_{w_2} = \frac{\gamma_2 c^2 d^2}{3} + \tau_2. \quad (6.50)$$

Substituting (6.46) into (6.48) yields

$$\delta_1 = -\delta_3 = -2\gamma_1 d(1+c), \quad \tau_1 = S_{w_L} + 2\gamma_1 d^2 c \quad \text{and} \quad \tau_2 = S_{w_L} - \gamma_2 c^2 d^2. \quad (6.51)$$

From (6.50) and (6.51), it follows that

$$S_{w_1} - S_{w_2} = \frac{d^2}{3} \left(\gamma_1(2 - 9c^2) - 4\gamma_2 c^2 \right). \quad (6.52)$$

Denoting the total mass variation in each layer as R_i :

$$R_1 = \frac{1}{d} \frac{\partial}{\partial t} \int_{-d(1+c)}^{-cd} \phi S_w dz, \quad (6.53)$$

$$R_2 = \frac{1}{2cd} \frac{\partial}{\partial t} \int_{-cd}^{cd} \phi S_w dz, \quad (6.54)$$

$$R_3 = \frac{1}{d} \frac{\partial}{\partial t} \int_{cd}^{d(1+c)} \phi S_w dz, \quad (6.55)$$

we assume that the mass is conserved in the direction z ($\phi \partial_t S_w + \partial_z u_w = 0$), which is equivalent to

$$R_1 + R_2 + R_3 = 0. \quad (6.56)$$

Using (6.46) and (6.48), we calculate the integrals (6.53), (6.54), (6.55), yielding

$$R_1 = R_3 = \frac{\bar{D}_1}{d} \frac{\partial S_w}{\partial z} \Big|_{z \rightarrow cd^-} = 2\bar{D}_1 \gamma_1, \quad (6.57)$$

$$R_2 = \frac{\bar{D}_2}{2cd} \frac{\partial S_w}{\partial z} \Big|_{z \rightarrow cd^-} - \frac{\bar{D}_2}{2cd} \frac{\partial S_w}{\partial z} \Big|_{z \rightarrow -cd^+} = 2\bar{D}_2 \gamma_2, \quad (6.58)$$

where \bar{D}_1 , \bar{D}_2 and \bar{D}_3 depend on S_{w_L} and are defined as:

$$\bar{D}_1 = - \lim_{z \rightarrow -cd^-} \lambda_{g_1} f_{w_1} \frac{\partial P_{c_1}}{\partial S_w}, \quad \bar{D}_2 = - \lim_{z \rightarrow -cd^+} \lambda_{g_2} f_{w_2} \frac{\partial P_{c_2}}{\partial S_w}, \quad \bar{D}_3 = \bar{D}_1. \quad (6.59)$$

From (6.56) we obtain $\gamma_2 = (-2\bar{D}_1/\bar{D}_2)\gamma_1$. Substituting this relation into (6.52), we obtain

$$\gamma_1 = \gamma_3 = \frac{3(S_{w_1} - S_{w_2})\bar{D}_2}{d^2[(2 - 9c^2)\bar{D}_2 + \bar{D}_1 c^2]} \quad \text{and} \quad \gamma_2 = \frac{-6(S_{w_1} - S_{w_2})\bar{D}_1}{d^2[(2 - 9c^2)\bar{D}_2 + \bar{D}_1 c^2]}. \quad (6.60)$$

On the other hand, R_i ($i = 1, 2, 3$) represent the terms on the right side of the water mass conservation equations in (6.11), where $R_1 = -\theta_{1\downarrow}(S_{w_1} - S_{w_2})$, $R_2 = [\theta_{2\uparrow} + \theta_{2\downarrow}](S_{w_1} - S_{w_2})$, and $R_3 = \theta_{3\uparrow}(S_{w_2} - S_{w_3})$. Using (6.57) and (6.58), we obtain that all mass exchange coefficients are equal:

$$\theta_{2\uparrow} = \theta_{2\downarrow} = \theta_{3\uparrow} = \theta_{1\downarrow} = \frac{6\bar{D}_1 \bar{D}_2}{d^2[(2 - 9c^2)\bar{D}_2 + 4\bar{D}_1 c^2]}. \quad (6.61)$$

This case satisfies Remark 6.3.2, allowing us to use the simplified formula (6.43) for estimating the single wavefront velocity.

Remark 6.5.1. Based on the parameter values provided in Table 4, by interpolation we find $S_{wL} = 0.78$, and using (6.61) yields $\theta_{2\uparrow} = \theta_{2\downarrow} = \theta_{3\uparrow} = \theta_{1\downarrow} = 2.1277 \times 10^4$. Notice that, the presented theory is valid for the case $c < 1/2$, *i.e.*, when the fracture thickness is at least twice thinner than the surrounding layers. Typically, it is orders of magnitude thinner. In the present work we consider $c = 0.05$, which is considered in the literature [61].

6.5.1 Numerical results

In what follows, let us verify the presented analysis simulating the two-dimensional model (6.1) using FOam DiSplacement SImuLator (FOSSIL) [29, 30]. To solve the first and second equation of (6.1) (which corresponds to the foam transport problem), FOSSIL uses the conservative method KNP introduced by Kurganov et al. [62], which is an extension of the finite volume method presented by Kurganov et al. [64]. To solve the problem composed of the third and fourth equations in (6.1), FOSSIL uses the conservative mixed finite element method proposed by Kurganov et al. [63]. The one-dimensional model (6.11) is solved using Reaction Convection Diffusion Equations Solver (RCD) [67]. In all simulations, we use the parameter values from Table 4 and also Table 5 corresponding to the symmetric case.

6.5.1.1 Two-dimensional simulations

To solve (6.1), we use the following boundary conditions in the domain Ω depicted in Fig. 23. In $x = 0$, the velocity is constant for all $z \in [0, D]$ ($u = (u_1 + u_2 + u_3)/3$), and the water saturation S_w is equal to the injection condition S_w^- . In $x = L$, we consider $\partial_x S_w = 0$.

Figure 25 shows the behavior of the water saturation front at three times. Notice that this front does not change shape, indicating that it corresponds to a traveling wave.

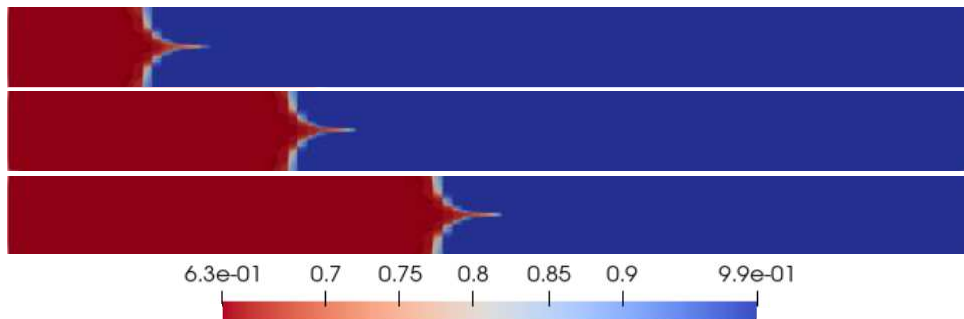


Figure 25 – Stable traveling water saturation profile (symmetric case), obtained through two-dimensional numerical simulations at 6000 s (upper plot), 12000 s (middle plot), and at 18000 s (lower plot).

To numerically verify the existence of a traveling wave solution for the two-

dimensional model (6.1), we estimate the position of the water saturation front in each layer. We evaluate the water saturation at three different heights. For Layer 1: $S_w(x, -d(1+2c)/2, t)$. For Layer 2: $S_w(x, 0, t)$, and for Layer 3: $S_w(x, d(1+2c)/2, t)$. At each time step, we estimate the x -position of the profile by calculating an average x_{S_w} front position corresponding to S_w in the range $[0.635, 0.999]$, see Fig. 26 and [104] for more details.

To estimate the average velocity of the wavefront in all layers, we use finite difference

$$v_{i,l} = \frac{x_{S_w}^{i,l} - x_{S_w}^{i,l-1}}{\Delta t}, \quad (6.62)$$

in each time step l , where $x_{S_w}^{i,l}$ represents the x -position of the front of the water saturation in Layer i . In Fig. 20(a), we compare the theoretically estimated wavefront velocity v obtained using (6.45) with the numerically evaluated moving mean velocities in each layer v_1 , v_2 and v_3 (calculated using 40 grid points around the front position). Figure 27(b) shows the standard deviation of the estimated velocities in each layer v_1 , v_2 , and v_3 evidencing that they stabilize after approximately 2000 [s] at $v_i = v_F = 1.671 \times 10^{-4} m/s$ ($i = 1, 2, 3$).

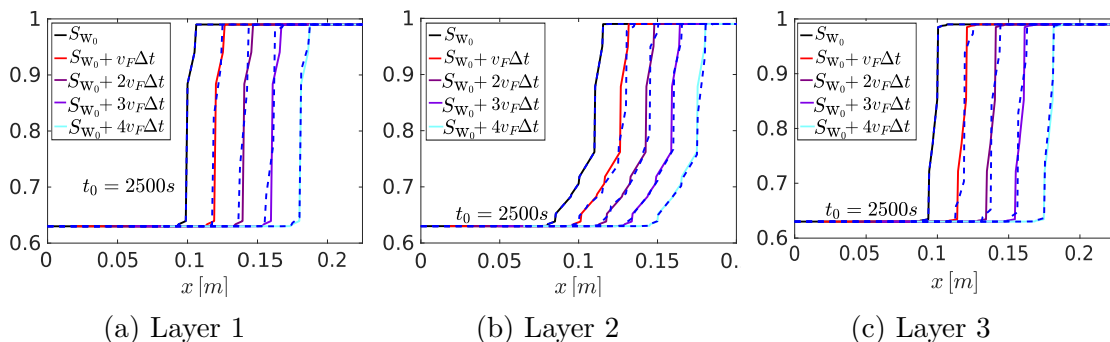


Figure 26 – Comparison of the water saturation profiles for the symmetric case. The dotted curves are obtained from FOSSIL simulations for times $t_0 = 2500s$, $t_1 = 3000s$, $t_2 = 3500s$, $t_3 = 4000s$, and $t_4 = 4500s$. Continuous curves represent the displacement of the water saturation profile at $t_0 = 2500s$ using the estimated velocity $v_F = 1.671 \times 10^{-4} m/s$.

To verify that the simulation results obtained from two-dimensional numerical simulations correspond to the traveling wave, we compare the water saturation profiles with the profile displaced using the estimated velocity $v_F = 1.671 \times 10^{-4} m/s$ ($S_{w_0} + v_F \Delta t$), see Fig. 26. Table 6 presents the L^2 distance between numerically obtained water saturation profiles and the displaced initial profile $S_{w_0} + v_F \Delta t$.

6.5.1.2 One-dimensional simulations

To calculate the x -position of the water saturation front at any time l , denoted as $x_{S_w}^{i,l}$, we employ linear interpolation with a fixed value of $S_{w_i} \in (\bar{S}_w - \epsilon, \bar{S}_w + \epsilon)$, where

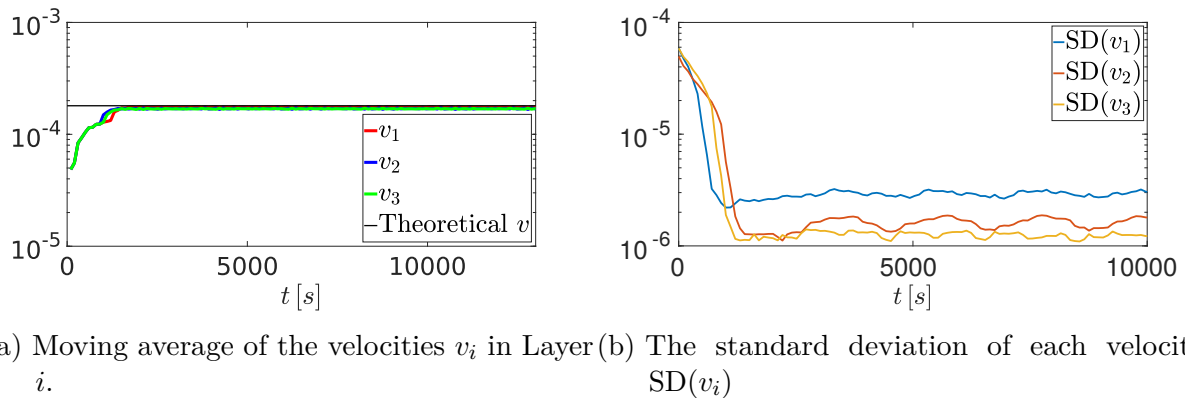


Figure 27 – Comparing velocities in the symmetric case. The theoretical velocity is estimated using Eq. (6.38).

Table 6 – Distance L^2 between $S_w(2500) + v_F \Delta t$ and $S_w(2500 + \Delta t)$, for $v_F = 1.671 \times 10^{-4} m/s$.

Δt	Layer 1	Layer 2	Layer 3
500 s	2.20×10^{-3}	1.71×10^{-3}	2.11×10^{-3}
1000 s	3.52×10^{-3}	1.70×10^{-3}	2.31×10^{-3}
1500 s	2.75×10^{-3}	3.01×10^{-3}	5.40×10^{-3}
2000 s	4.24×10^{-3}	3.00×10^{-3}	2.43×10^{-3}

$\bar{S}_w = (S_w^- + S_w^+)/2$, and $\epsilon \approx 0.1$. Then, we utilize the finite-difference formula (6.62) to compute the numerical approximation of the velocity in the one-dimensional model.

Figure 28 shows S_w and n_D profiles at three times after the wavefront stabilization. We observe that the water saturation profiles for each layer do not change shape over time. Fig. 29 shows that the distance between the profiles does not vary. The velocities v_i are estimated using finite differences as in Eq. (6.62).

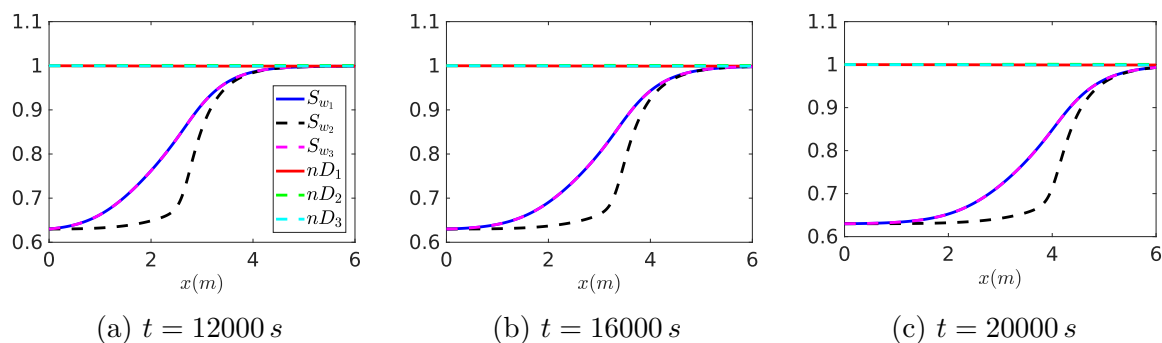


Figure 28 – Simulations in the one-dimensional model (symmetric case) for $t = 12000 s$, $t = 16000 s$ and $t = 20000 s$, using the parameters of Table 4.

From Eq. (6.38), the theoretical velocity is $v = 1.786 \times 10^{-4} m/s$. In Fig. 30(a), we compare the theoretically estimated wavefront velocity v obtained using (6.45) with the numerically evaluated moving mean velocities in each layer v_1 , v_2 and v_3 (calculated using 200 grid points around the front position). Figure 30(b) shows the standard deviation of

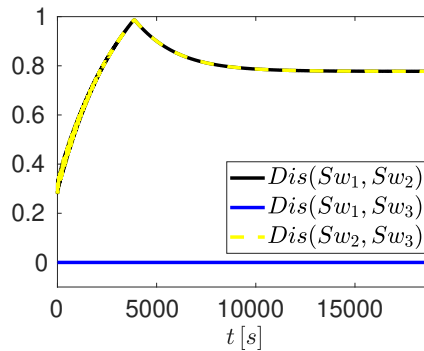
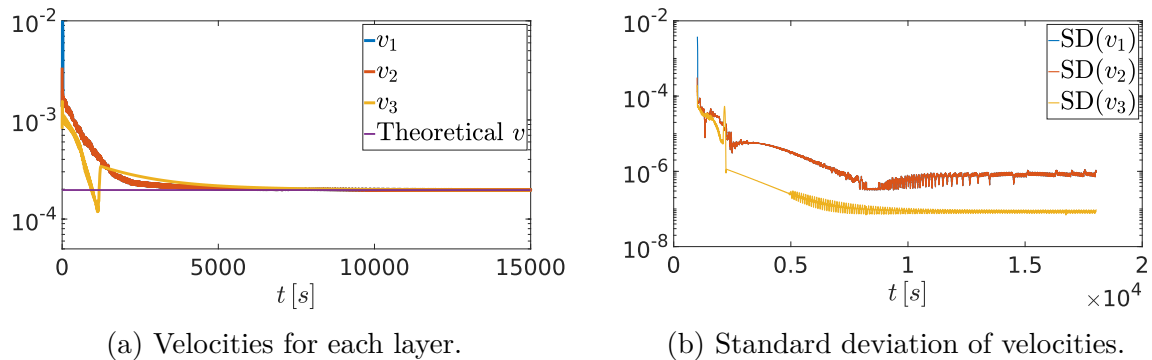


Figure 29 – Distance between the water saturation fronts S_{w_i} ($i = 1, 2, 3$), symbolized as Dis , for the symmetric case.

the estimated velocities in each layer v_1 , v_2 , and v_3 evidencing that they stabilize after approximately 2000 [s] at $v_i = v_R = 1.8024 \times 10^{-4} m/s$ ($i = 1, 2, 3$).



(a) Velocities for each layer.

(b) Standard deviation of velocities.

Figure 30 – Velocities simulated (symmetric case), using RCD and standard deviation of velocities, estimated using a moving average regularization for groups of 200 data.

Notice that the numerically obtained velocity v_F for the general model (as in Fig. 27) differs from the theoretical one v by 6.4%, while the difference between one-dimensional and theoretical velocities (v_R and v as in Fig. 30) is 0.9%. These variations are expected as the theoretical velocity was estimated for the one-dimensional model.

6.6 Non-symmetric foam front in fractured porous medium

In this section, we estimate the coefficients $\theta_{1\downarrow}$, $\theta_{2\uparrow}$, $\theta_{2\downarrow}$, and $\theta_{3\uparrow}$ of the one-dimensional model (6.11) for $n = 3$, which are explicitly used in the calculation of the velocity v in equation (6.45). Similarly to the assumption in [104], we consider S_w to be a piece-wise quadratic function of z as in (6.46). However, in this case, $S_w(z)$ is non-symmetric with respect to the origin; see Fig. 31. The mean water saturation in each

layer are

$$S_{w_1} = \frac{1}{d} \int_{-d(1+c)}^{-cd} S_w(z) dz, \quad (6.63)$$

$$S_{w_2} = \frac{1}{cd} \int_{-cd}^0 S_w(z) dz, \quad (6.64)$$

$$S_{w_3} = \frac{1}{d} \int_{cd}^{d(1+c)} S_w(z) dz, \quad (6.65)$$

As we assume that there is no water loss at the reservoir's edges, $S_w(z)$ satisfies the first equation in (6.48). The right equation in (6.48) is satisfied because $(0, S_w(0))$ is the critical point of the parabola inside the middle layer. The continuity of $S_w(z)$ function within $(-d(1+c), d(1+c))$ is guaranteed by the lateral limits (Analogous to (6.49), see Fig. 31)

$$\lim_{z \rightarrow -cd^-} S_w(z) = \lim_{z \rightarrow -cd^+} S_w(z) = S_{w_L}^1, \quad (6.66)$$

$$\lim_{z \rightarrow cd^-} S_w(z) = \lim_{z \rightarrow cd^+} S_w(z) = S_{w_L}^2, \quad (6.67)$$

with $S_w(0) = S_{w_0}$.

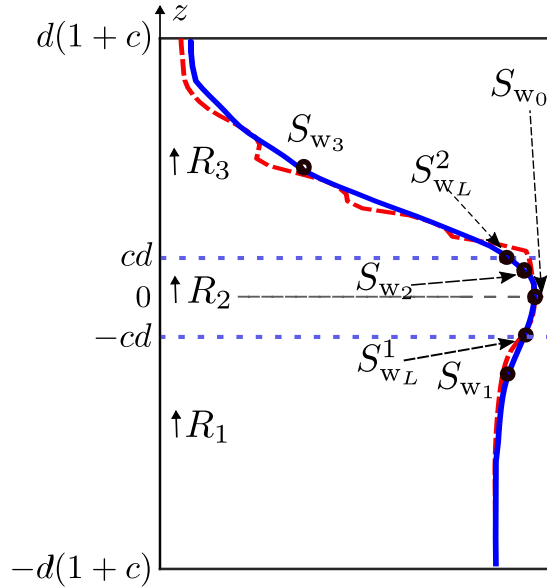


Figure 31 – Schematic representation of the saturation of water S_w along the vertical cross-section of the porous medium of three layers, where $c \in (0, 1)$ is constant. The dotted red curve is the exact representation of S_w calculated at $t = 10000$ s in the two-dimensional simulations. The continuous blue curve S_w is an approximation with respect to z . Coefficients R_i represent the total mass variation in each layer i . The saturation value at the interface between layers 1 and 2 is $S_{w_L}^1$, and, $S_{w_L}^2$, between layers 2 and 3. S_{w_i} is the average value in each region of the domain i with permeability k_i .

Using the definitions of R_i from (6.53)-(6.55) yields

$$R_1 = 2\gamma_1 \bar{D}_1, \quad R_2 = 4\gamma_2 \bar{D}_2, \quad \text{and} \quad R_3 = -2\gamma_3 \bar{D}_3, \quad (6.68)$$

where \bar{D}_1 and \bar{D}_2 are defined in (6.59), however in this case, \bar{D}_3 satisfy

$$\bar{D}_3 = - \lim_{z \rightarrow cd^-} \lambda_{g_3} f_{w_3} \frac{\partial P_{c_3}}{\partial S_w}. \quad (6.69)$$

We assume that the mass is conserved in the direction z ($\phi \partial_t S_w + \partial_z u_w = 0$); which is equivalent to $R_1 + R_2 + R_3 = 0$. From here, we obtain that

$$\gamma_2 = \frac{-\bar{D}_1 \gamma_1}{2\bar{D}_2} + \frac{\bar{D}_3 \gamma_3}{2\bar{D}_2}. \quad (6.70)$$

Calculating the integrals given in Eqs. (6.63), (6.64), and (6.65), we obtain:

$$S_{w_1} - S_{w_2} = \frac{-2}{3} \gamma_1 d^2 + \frac{2}{3} c^2 \gamma_2 d^2, \quad (6.71)$$

$$S_{w_2} - S_{w_3} = \frac{-2}{3} \gamma_2 c^2 d^2 + \frac{2}{3} \gamma_3 d^2. \quad (6.72)$$

From the system Eqs. (6.70)-(6.72) we obtain

$$\gamma_2 = \frac{3\bar{D}_1(S_{w_1} - S_{w_2})}{2d^2(\bar{D}_1 c^2 - \bar{D}_3 c^2 + 2\bar{D}_2)} + \frac{3\bar{D}_3(S_{w_2} - S_{w_3})}{2d^2(\bar{D}_1 c^2 - \bar{D}_3 c^2 + 2\bar{D}_2)}. \quad (6.73)$$

Using (6.73), together with the fact that

$$R_2 = 4\gamma_2 \bar{D}_2 = \theta_{2\uparrow}(S_{w_1} - S_{w_2}) - \theta_{2\downarrow}(S_{w_2} - S_{w_3}), \quad (6.74)$$

we obtain

$$\theta_{2\uparrow} = \frac{6\bar{D}_1 \bar{D}_2}{d^2(\bar{D}_1 c^2 - \bar{D}_3 c^2 + 2\bar{D}_2)}, \quad \theta_{2\downarrow} = \frac{6\bar{D}_2 \bar{D}_3}{d^2(\bar{D}_1 c^2 - \bar{D}_3 c^2 + 2\bar{D}_2)}. \quad (6.75)$$

As the mass is conserved in the vertical direction, and $R_1 = -\theta_{1\downarrow}(S_{w_1} - S_{w_2})$, $R_3 = \theta_{3\uparrow}(S_{w_2} - S_{w_3})$, we obtain:

$$\theta_{2\uparrow} = \theta_{1\downarrow}, \quad \text{and} \quad \theta_{2\downarrow} = \theta_{3\uparrow}. \quad (6.76)$$

Remark 6.6.1. Based on the parameter values provided in Table 4, by interpolation we found $S_{W_L}^1 = 0.8$ and $S_{W_L}^2 = 0.81$. Using (6.75) yields $\theta_{1\downarrow} = \theta_{2\uparrow} = 1.7591 \times 10^{-4}$, and $\theta_{3\uparrow} = \theta_{2\downarrow} = 2.9103 \times 10^{-4}$.

6.6.1 Numerical results

6.6.1.1 Two-dimensional simulations

As in the symmetric case, we solve system (6.1) numerically with the same boundary conditions, see Fig. 32. The corresponding water saturation profiles calculated at the middle of each layer are shown in Fig. 33. Notice that the drainage profile inside the fracture (see Fig. 26b) presents a sharper profile than the surrounding permeable layers. However, in the non-symmetric case, this effect is less pronounced (see Fig. 33b).

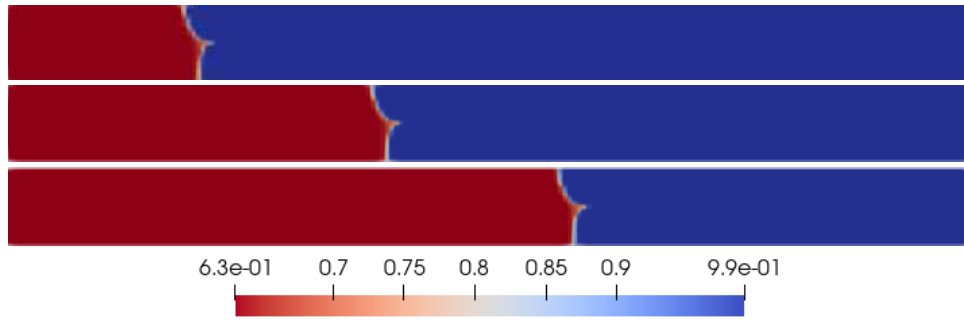


Figure 32 – Stable traveling water saturation profile (non-symmetric case), obtained through two-dimensional numerical simulations at 6000 s (upper plot), 12000 s (middle plot) and at 18000 s (lower plot).

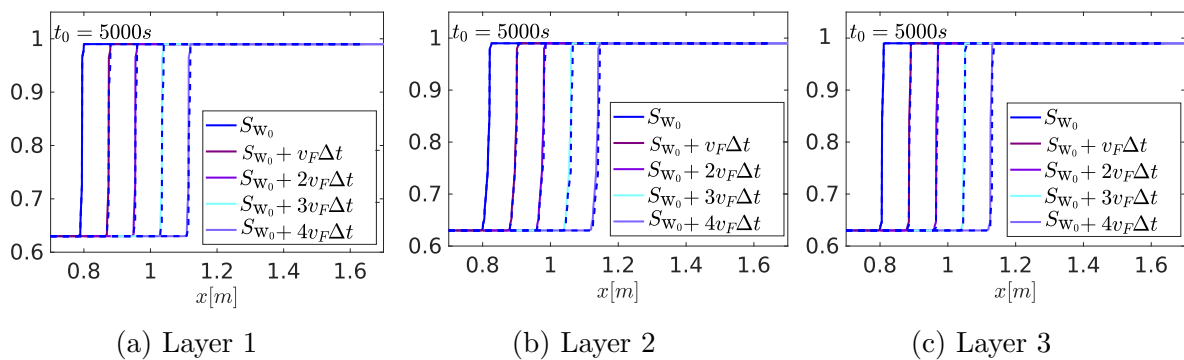


Figure 33 – Comparison of the water saturation profiles for the symmetric case. The dotted curves are obtained from FOSSIL simulations for times $t_0 = 5000s$, $t_1 = 5500s$, $t_2 = 6000s$, $t_3 = 6500s$, and $t_4 = 7000s$. Continuous curves represent the displacement of the water saturation profile at $t_0 = 5000s$ using the estimated velocity $v_F = 1.723 \times 10^{-4}m/s$.

In Fig. 34(a), we compare the theoretically estimated wavefront velocity v obtained using (6.45) with the numerically evaluated moving mean velocities in each layer v_1 , v_2 and v_3 (calculated using 50 grid points around the front position). Figure 34(b) shows the standard deviation of the estimated velocities in each layer v_1 , v_2 , and v_3 evidencing that they stabilize after approximately 5000 [s] at $v_i = v_F = 1.723 \times 10^{-4}m/s$ ($i = 1, 2, 3$).

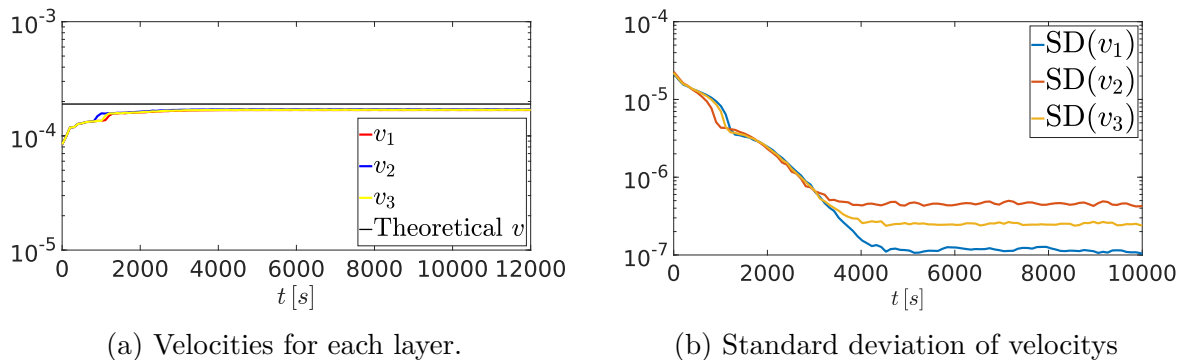


Figure 34 – Comparing velocities in the non-symmetric case. The theoretical velocity is estimated using Eq. (6.38)

To verify that the simulation results obtained from two-dimensional numerical simulations correspond to the traveling wave, we compare the water saturation profiles with the profile displaced using the estimated velocity $v_F = 1.723 \times 10^{-4} m/s$ ($S_{w_0} + v_F \Delta t$), see Fig. 33. Table 7 presents the L^2 distance between numerically obtained water saturation profiles and the displaced initial profile $S_{w_0} + v_F \Delta t$.

Table 7 – Distance L^2 between $S_w(5000) + v_F \Delta t$ and $S_w(5000 + \Delta t)$ in the layer i , considering $v_F = 1.723 \times 10^{-4} m/s$.

Δt	Layer 1	Layer 2	Layer 3
500 s	2.74×10^{-3}	1.87×10^{-4}	6.61×10^{-3}
1000 s	4.41×10^{-3}	2.41×10^{-4}	9.01×10^{-3}
1500 s	6.31×10^{-4}	8.54×10^{-4}	9.52×10^{-3}
2000 s	1.01×10^{-3}	2.61×10^{-3}	5.13×10^{-3}

6.6.1.2 One-dimensional simulations

As in Section 6.3, we solve system (6.11), see Fig. 35 for the water saturation and foam texture profiles. Figure 36 shows that the distance between the profiles in Fig. 35 does not vary in time. The velocities v_i are estimated using finite differences as in (6.62).

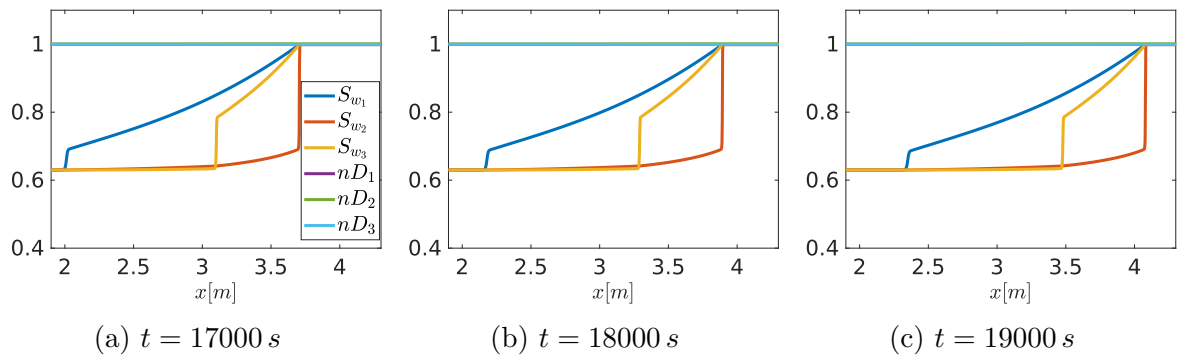


Figure 35 – Simulations in the one-dimensional model (non-symmetric case) for $t = 17000 s$, $t = 18000 s$ and $t = 19000 s$, using the parameters of Table 4.

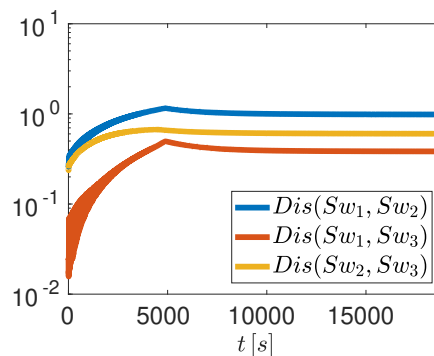


Figure 36 – Distance between the water saturation fronts S_{w_i} ($i = 1, 2, 3$), symbolized as Dis , for the non-symmetric case.

In Fig. 37(a), we compare the theoretically estimated wavefront velocity $v = 1.9063 \times 10^{-4} \text{ m/s}$ obtained using (6.45) with the numerically evaluated moving mean velocities in each layer v_1 , v_2 and v_3 (calculated using 1200 grid points around the front position). Figure 37(b) shows the standard deviation of the estimated velocities in each layer v_1 , v_2 , and v_3 evidencing that they stabilize after approximately 10000 [s] at $v_i = v_R = 1.8696 \times 10^{-4} \text{ m/s}$ ($i = 1, 2, 3$).

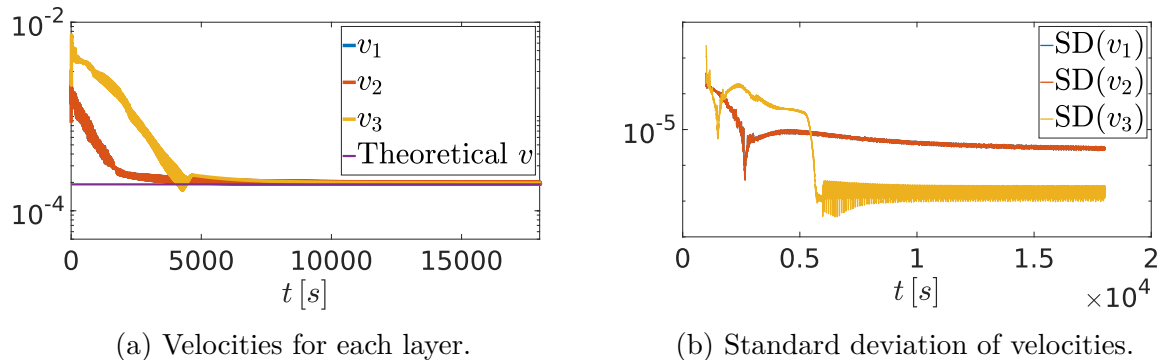


Figure 37 – Velocities simulated (non-symmetric case), using RCD and standard deviation of velocities, estimated using a moving average regularization for groups of 1200 data.

Analogously to the previous case, the difference between the numerically obtained velocity v_F for the general model (as in Fig. 34) differs from the theoretical velocity v by 9.61%. On the other hand, the difference between one-dimensional simulated velocity v_R (as in Fig. 37) and v is 1.93%.

As expected from Equation (6.45), the numerical estimates indicate that the wavefront velocity for the symmetric case is lower than in the non-symmetric case; see Table 8. In the non-symmetric case, it is observed that the time required for the wavefront velocity to stabilize is close to 5000 seconds, whereas in the symmetric case, it stabilizes at around 2000 seconds. As shown in Figs. 34 and 37, the wavefront velocity in the non-symmetric case exhibits more significant oscillations, requiring more time to stabilize and more points to regularize.

Table 8 – Velocities for symmetric and non-symmetric case.

	Symmetric	Non-symmetric
Theoretical velocity v [m/s]	1.786×10^{-4}	1.9063×10^{-4}
One-dimensional velocity v_R [m/s]	1.8024×10^{-4}	1.8696×10^{-4}
Two-dimensional velocity v_F [m/s]	1.671×10^{-4}	1.723×10^{-4}

6.7 Partial conclusions

We showed that the foam presence induces the formation of the single traveling wave front in the fractured porous medium when the fracture is modeled as a thin, highly permeable layer surrounded by two thicker layers. To evidence our findings, we explore

two scenarios: in the first one, the permeabilities of the two outer layers are equal, while the second, and more realistic one, involves different permeabilities. In both scenarios, the single traveling foam wavefront is formed, avoiding the gas dominant flow through the fracture and improving the sweep efficiency.

To conduct the analysis, we extended previous results showing the single traveling wave formation in n -layered porous medium. We derived an analytical formula for the wavefront velocity for n layers. This equation depends on the estimation of the mass exchange between the layers. To make this estimate, we approximate the water saturation front as a differentiable function in the z -direction using the shape of the traveling profile and imposing some conditions on its geometry. We validate it by simulations for a realistic two-dimensional model. We consider two cases where the imposed geometric conditions are independent.

This formula provides an estimate for the front propagation velocity in a stratified medium, allowing a gas breakthrough time preview, which is a piece of key information in many applications.

7 ON THE VISCOUS CROSSFLOW DURING THE FOAM DISPLACEMENT IN TWO-LAYERED POROUS MEDIA

This chapter is a reprint of a paper submitted in 2023 [105].

We investigate an immiscible incompressible two-phase foam flow in an internally homogeneous two-layered porous medium with different porosities and absolute permeabilities. Using the traveling wave solution, we classify the foam flow depending on the absolute permeability and the porosity ratio between layers. We show that the mass crossflow between layers is connected to the relative position of the flow front in these layers and that the porosity difference between layers impacts the mass crossflow. For our analysis, we extended the previous result, evidencing that the presence of foam induces the existence of a single flow front in both layers.

7.1 Introduction

Foam, which is an agglomeration of gas bubbles that are separated from each other by thin liquid films called *lamellae* [14, 60], is used to mitigate issues encountered in gas sweeping [46, 78]. Thus, foam is mainly used to reduce gas phase mobility. This method has already been applied to remediation of contaminated aquifers [17] and soils [14, 46, 13, 36], acid diversion during matrix stimulation [10], and hydrocarbon recovery [95, 65, 3, 93].

Natural reservoirs typically have fractured and multilayered structures [110, 4, 9, 100, 86, 107, 83, 61]. A better understanding of multiphase flow in layered porous media is required to accurately predict subsurface processes. In this work, we consider a two-layer porous medium with different porosities and absolute permeabilities. In this scenario, the viscous crossflow is common to occur due to differences in the fluid mobility between layers. For instance, if the displaced fluid presents a lower viscosity than the displacing fluid, the former tends towards a less permeable layer [110, 95]. In [12, 85], the authors performed experiments in a cylindrical annulus porous media considering foam flow with different permeabilities. In all experiments, they used the ratio between layer permeabilities significantly higher compared to the ratio between layer porosities. The authors investigated the effects of crossflow and identified that foam displaces from the higher permeability layer to the lower one. [34] considered a homogeneous medium in the first one-third of the core and two layers with different permeability and equal porosity in the last two-thirds of the core. They adopted Stochastic Population Balance model [116] to investigate the foam impact on the recovery numerically.

One of the first works highlighting crossflow between layers was performed by [110]. Later, it was mathematically formalized by [108] using regular asymptotic expansion and keeping the leading order terms, which provides the vertical equilibrium assumption,

that is, a negligible transverse pressure gradient. The crossflow between two layers was addressed in [31, 32], where the impact of varying several parameters (end-points relative permeabilities, absolute permeability, porosity) on the total recovery is investigated. Considering two-phase flow with controlled injection of low salinity water, [65] presents favorable relationships between mobility ratios for the existence of viscous crossflow and studies how this affects the oil recovery. In [69, 44], the authors presented analytical solutions to the two-phase flow model without an active tracer in layered porous media, representing the system as a one-dimensional model. [61] investigate the flow without tracer in a two-dimensional multi-layered porous medium with fracture by applying the limit in the fracture length. [104] estimated the mass exchange between layers in the presence of foam and used this information to show the formation of a single flow front in both layers using the traveling wave solution. The later used layers with equal porosities and considered the evolution of foam texture described by the linear kinetic model proposed by [8]. The present work extends [104] by considering variable porosities in different layers and shows the formation of the single flow front using traveling waves.

We consider an immiscible two-phase foam flow in a two-layered porous medium (internally homogenous) with different porosities and absolute permeabilities. We classify the resulting foam flow depending on the ratio of the layer porosities and permeabilities connecting the relative front position in each layer with the mass crossflow. For this, we use the hypotheses of vertical equilibrium (**VE**) used in [110, 108, 66] and adopt Linear Kinetic Model [8] to describe the foam dynamics.

The remainder of this chapter is structured as follows. Section 7.2 presents the mathematical model and all physical parameters. Section 7.3 presents the analytical estimate of the relative front positions. In Section 7.4, the main numerical simulations are presented. Section 7.5 discusses the main results, which are concluded in Section 7.8. In Appendix 7.6, we extend the results in [104] to the case with variable porosities. Finally, Appendix 7.7 summarizes the numerical algorithm used in our simulations.

7.2 Mathematical model

We consider a two-dimensional, two-phase (gas and water) flow in a porous medium. To emphasize the viscous forces effect, we follow [108, 31] neglecting gravity and capillary forces. As in [55, 109], we consider the water phase a surfactant solution with the corresponding concentration significantly above critical micelle concentration (CMC). As in [8, 116, 104], the model is composed of the water mass conservation equation (7.1), foam texture (n_D) population balance equation (7.2), Darcy law (7.3), and continuity

equation with the incompressibility condition (7.4):

$$\phi \frac{\partial S_w}{\partial t} + \nabla \cdot u_w = 0; \quad (7.1)$$

$$\phi \frac{\partial}{\partial t}(S_g n_D) + \nabla \cdot (u_g n_D) = \phi S_g \Phi(S_w, n_D), \quad (7.2)$$

$$u = -k\lambda \nabla P, \quad (7.3)$$

$$\nabla \cdot u = 0, \quad (7.4)$$

where ϕ is the porosity and k is the absolute permeability; S_w and S_g are water and gas saturations in a porous media filled by both fluids ($S_w + S_g = 1$); n_D is the foam texture; u_w and u_g are velocities of gas and water phases; $u = u_w + u_g$ is the total velocity; P is pressure; λ is the total mobility. The foam generation and coalescence function is

$$\Phi(S_w, n_D) = K_c(n_D^{\text{LE}}(S_w) - n_D), \quad (7.5)$$

where K_c is the linear kinetic parameter, and $n_D^{\text{LE}}(S_w)$ is the equilibrium foam texture proposed by [8]:

$$n_D^{\text{LE}}(S_w) = \begin{cases} \tanh(A(S_w - S_w^*)), & S_w > S_w^*, \\ 0, & S_w \leq S_w^*, \end{cases} \quad (7.6)$$

where A is a model parameter, and S_w^* is the critical water saturation (related to the limiting capillary pressure, see [57]).

To close the system (7.1)-(7.4), we use the standard fractional flow theory [9, 16]. Water and gas phases velocity are defined as

$$u_w = u f_w + k \lambda_g f_w \nabla P_c, \quad (7.7)$$

$$u_g = u f_g - k \lambda_w f_g \nabla P_c, \quad (7.8)$$

where the fractional flow functions of water and gas phases (f_w and f_g), water and gas relative mobilities (λ_w and λ_g), and the total mobility (λ) are given by

$$f_w = \frac{\lambda_w}{\lambda_w + \lambda_g}, \quad f_g = \frac{\lambda_g}{\lambda_w + \lambda_g}, \quad \lambda_w = \frac{k_{rw}(S_w)}{\mu_w}, \quad \lambda_g = \frac{k_{rg}^f(S_w, n_D)}{\mu_g}, \quad \lambda = \lambda_w + \lambda_g, \quad (7.9)$$

the Newtonian water relative permeability of the foamed gas is [8]

$$k_{rg}^f(S_w, n_D) = \frac{k_{rg}(S_w)}{18500 n_D + 1}, \quad (7.10)$$

the relative permeability of water is

$$k_{rw}(S_w) = \begin{cases} 0, & 0 \leq S_w \leq S_{wc}, \\ k_{rw}^0 \left(\frac{S_w - S_{wc}}{1 - S_{wc} - S_{gr}} \right)^{n_w}, & S_{wc} < S_w \leq 1, \end{cases} \quad (7.11)$$

the relative permeability of foamed gas is

$$k_{rg}(S_w) = \begin{cases} k_{rg}^0 \left(\frac{1 - S_w - S_{gr}}{1 - S_{wc} - S_{gr}} \right)^{n_g}, & 0 \leq S_w < 1 - S_{gr}, \\ 0, & 1 - S_{gr} \leq S_w \leq 1, \end{cases} \quad (7.12)$$

where k_{rw}^0 and k_{rg}^0 are end-point relative permeabilities of water and gas phases; n_w and n_g are Corey exponents. The capillary pressure is defined as [71]:

$$P_c(S_w) = \sigma \sqrt{\frac{\phi}{k}} \frac{0.022 (1 - S_w - S_{gr})^c}{(S_w - S_{wc})}, \quad (7.13)$$

where σ is the surface tension, S_{wc} is the connate water saturation, S_{gr} is the residual saturation of the gas and c is an exponent parameter.

As in [104, 95], we consider the two-layered porous medium of length L and each layer depth d (see Fig. 38) with boundary conditions given by Neumann no-flow conditions at $z = -d$, at $z = +d$, and at the right boundary ($x = L$); a prescribed constant injection velocity \bar{u}_{inj} at the inlet ($x = 0$). In addition, we consider the initial condition to be Riemann-type with injected state S_w^- and initial state S_w^+ , as reported in Table 9. In general, we consider the same model and geometry as in [104], except that constant porosity (ϕ) and absolute permeability (k) can be different between layers indicated by sub-indexes 1 and 2, see Fig. 38.

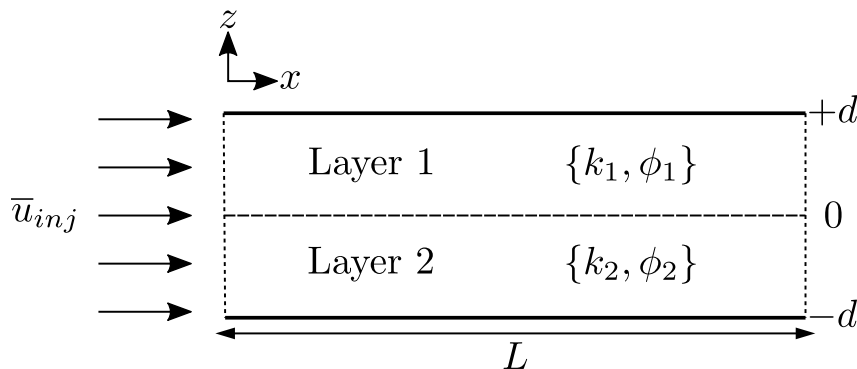


Figure 38 – Schematic representation of the two-layered communicating porous medium.

7.3 Estimating the wavefront internal structure

As shown in Appendix 7.6, the foam flow in two-layered porous media moves as a single traveling wave front. To obtain the wavefront internal structure, we use the method of characteristics (MOC) [70] to estimate the wave velocities inside each layer following a procedure similar to [31]. The common physical configuration corresponds to a situation when the reservoir's length is considerably larger than the height $L \gg 2d$, see [108]. That is why we follow [110, 108], and assume the hypotheses of vertical equilibrium (VE), *i.e.*, neglecting the transversal variation of pressure ($\partial P / \partial z = 0$). Assuming one-dimensional

approximation for each layer ($i = 1, 2$), neglecting capillary effects, and applying VE approximation, Eqs. (7.1)-(7.4) are rewritten as:

$$\phi_i \frac{\partial S_{w_i}}{\partial t} + u_{x_i} \frac{\partial f_w}{\partial x} = 0, \quad (7.14)$$

$$\frac{\partial u_{x_i}}{\partial x} = 0, \quad (7.15)$$

$$\phi_i \frac{\partial (S_{g_i} n_{D_i})}{\partial t} + u_{x_i} \frac{\partial (f_g n_{D_i})}{\partial x} = \phi_i S_{g_i} \Phi_i(S_{w_i}, n_{D_i}), \quad (7.16)$$

$$u_{x_i} = -k_i \lambda_i \frac{\partial P}{\partial x}, \quad (7.17)$$

where S_{w_i} is the representative water saturation in each layer, n_{D_i} is the foam texture, $\mathbf{u}_i = (u_{x_i}, u_{z_i})^T$ is the velocity field, ϕ_i is the porosity, k_i is the absolute permeability and Φ_i is the source term, whereas sub-index $i = 1, 2$ refers to each layer.

Note that Eqs. (7.14) and (7.16) are coupled since the water fractional flow function depends on water saturation and foam texture ($f_w = f_w(S_{w_i}, n_{D_i})$). Substituting Eqs. (7.14) and (7.15) into Eq. (7.16) and isolating the total derivative of n_{D_i} , we obtain

$$\frac{dn_{D_i}}{dt} = \frac{\partial n_{D_i}}{\partial t} + \frac{u_{x_i}}{\phi_i} \frac{(1 - f_w)}{(1 - S_{w_i})} \frac{\partial n_{D_i}}{\partial x} = \Phi_i(S_{w_i}, n_{D_i}). \quad (7.18)$$

The solution of Eq. (7.18) can be obtained through n_D -characteristic curves (see [70]):

$$\frac{dn_{D_i}}{dt} = \Phi_i(S_{w_i}, n_{D_i}), \quad (7.19)$$

$$\left(\frac{dx}{dt} \right)_{n_{D_i}} = \frac{u_{x_i}}{\phi_i} \frac{(1 - f_w)}{(1 - S_{w_i})}. \quad (7.20)$$

We solve Eq. (7.19) with Φ_i defined in (7.5) for $S_{w_i} > S_w^*$ with initial foam texture $n_{D_i}^+$:

$$n_{D_i} = n_{D_i}^+ e^{-K_c t} + K_c n_{D_i}^+ \int_0^t \tanh(A(S_{w_i} - S_w^*)) dt. \quad (7.21)$$

The first term on the right side of the last expression refers to the homogenous part of the solution of Eq. (7.19), whereas the second term refers to the non-homogenous part. When the water saturation is below critical ($S_{w_i} < S_w^*$), it follows that $n_D^{\text{LE}}(S_{w_i}) = 0$, and the solution presents only the homogeneous part.

Notice that, along the n_D -characteristic, $n_{D_i} = n_{D_i}(S_{w_i})$ as in (7.21) yielding that the fractional flow defined in (7.9) depends only on S_{w_i} ($f_w = f_w(S_{w_i})$). Thus, Eq. (7.14) becomes one-dimensional conservation law with S_w -characteristic curve associated with characteristic velocity in each (not connected) layer $v_i = (dx/dt)_{S_{w_i}}$ given by

$$v_i = \frac{u_{x_i}}{\phi_i} \frac{\partial f_w}{\partial S_{w_i}}, \quad i = 1, 2. \quad (7.22)$$

We note that the estimated characteristic velocity in the last expression depends on absolute permeability (through u_{x_i} in Eq. (7.17)) and porosity. Equation (7.22) is

calculated along the S_w -characteristic curve, (i.e., along the curve where S_w is constant), allowing us to compare both characteristic velocities for the same S_w ($S_{w_1} = S_{w_2}$) evaluating the fraction:

$$\frac{v_1}{v_2} = \frac{\mathcal{K}}{\mathcal{P}}, \quad (7.23)$$

where we define $\mathcal{K} = k_1/k_2$ and $\mathcal{P} = \phi_1/\phi_2$. Next, we show how the fraction in (7.23) reflects in the relative positions of the fronts inside layers and to the mass exchange.

7.4 Numerical simulation results

We simulate the foam flow in three cases ($\mathcal{K} < \mathcal{P}$, $\mathcal{K} = \mathcal{P}$, and $\mathcal{K} > \mathcal{P}$) using the general model (7.1)-(7.4). Simulations use software FOSSIL (see Appendix 7.7) with $N_x = 200$ horizontal cells, $N_z = 40$ vertical cells, and time mesh with $N_T = 1000$ cells until the final simulation time T_f , and parameter values from [8] (including the Riemann problem initial data S_w^- and S_w^+); the values of $n_{D_i}^-$ and $n_{D_i}^+$ are calculated using Equation (7.6) and are reported in Table 9. The total superficial velocity was estimated in [104], see Table 9. For each case, we consider different porosities and absolute permeabilities as described in Table 10.

Table 9 – Parameter values used in numerical simulations. Source: [8, 104].

Symbol	Value	Parameter
S_{wc}	0.2 [-]	Connate water saturation
S_{gr}	0.18 [-]	Residual gas saturation
μ_w	10^{-3} [Pa s]	Water viscosity
μ_g^0	$2 \cdot 10^{-5}$ [Pa s]	Gas viscosity in the absence of foam
u	$2.198 \cdot 10^{-6}$ [m s $^{-1}$]	Total superficial velocity
n_{max}	$8 \cdot 10^{13}$ [m $^{-3}$]	Maximum foam texture
S_w^*	0.37 [-]	Critical water saturation
S_w^-	0.372 [-]	Injected water saturation
S_w^+	0.72 [-]	Initial water saturation
n_D^-	0.664 [-]	Injected foam texture
n_D^+	1 [-]	Initial foam texture
K_c	200 [s $^{-1}$]	Foam creation/coalescence constant
A	400 [-]	Foam model parameter
n_w	4.5 [-]	Permeability water exponent
n_g	1.3 [-]	Permeability gas exponent
k_{rw}^0	0.2 [-]	End-point of the water relative permeability
k_{rg}^0	0.94 [-]	End-point of the gas relative permeability
c	0.01 [-]	Capillary pressure power parameter
σ	0.03 [N m $^{-1}$]	Gas-water interfacial tension
L	0.25 [m]	Reservoir length
d	$5 \cdot 10^{-3}$ [m]	Depth of Layers 1 and 2
T_f	10.000 [s]	Final simulation time

Table 10 – Porosity and absolute permeability values used to perform two-dimensional simulation. Source: [8, 104].

	k_1 [m ²]	k_2 [m ²]	ϕ_1 [-]	ϕ_2 [-]
Case I: $\mathcal{K} < \mathcal{P}$	$2 \cdot 10^{-12}$	10^{-12}	0.3	0.1
Case II: $\mathcal{K} = \mathcal{P}$	$2 \cdot 10^{-12}$	10^{-12}	0.3	0.15
Case III: $\mathcal{K} > \mathcal{P}$	$2 \cdot 10^{-12}$	10^{-12}	0.25	0.2

7.4.1 Case I: $\mathcal{K} < \mathcal{P}$

In this case, the absolute permeability and porosity of the first layer are greater than those of the second layer with the permeability ratio $\mathcal{K} = 2$ and the porosity ratio $\mathcal{P} = 3$, see Table 10. As indicated in Eq. (7.23), the characteristic velocity in layer 1 is lower than the same of layer 2 ($v_1 < v_2$).

The two-dimensional front profile obtained by simulating Eqs. (7.1)-(7.4) at times $t = 1000, 2000, 3000$ [s] (from top to bottom) is shown in Fig. 39. After stabilizing, as expected from the analysis presented in Appendix 7.6, the fronts move as a single traveling wave. We observe that the front in layer 1 stays behind the one in layer 2 aligned with the relation in (7.23).

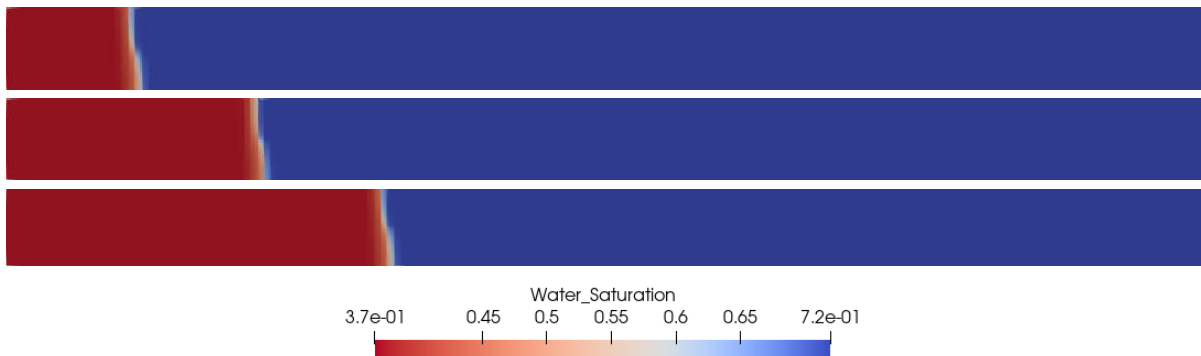


Figure 39 – The water saturation profile obtained simulating Eq. (4.1)-(7.4) for Case I: $\mathcal{K} < \mathcal{P}$ for three times: $t = 1000$ [s] (top), $t = 2000$ [s] (middle), and $t = 3000$ [s] (bottom).

The vertical velocity field around the wavefront at $t = 2000$ [s] is shown in the left panel in Fig. 40. Behind the front, we notice an increase in the velocity component pointing from Layer 2 to Layer 1. Ahead of the front, we observe the flow in the opposite direction. The right panel in Fig. 40 shows the water saturation front at $t = 2000$ [s], where we schematically indicate the mass exchange between layers. We designed the white arrows to point out the mass flux inversion, which happens from the high/lower permeability layer to the lower/high permeability layer ahead/behind the front. A similar crossflow phenomenon was reported in [31, 65, 89] for a system without an active tracer. Differently from what was reported in these works, the front in layer 2 is ahead of one in layer 1, making evident the dominant effect of different porosity on the flow fronts in the presence of an active tracer.

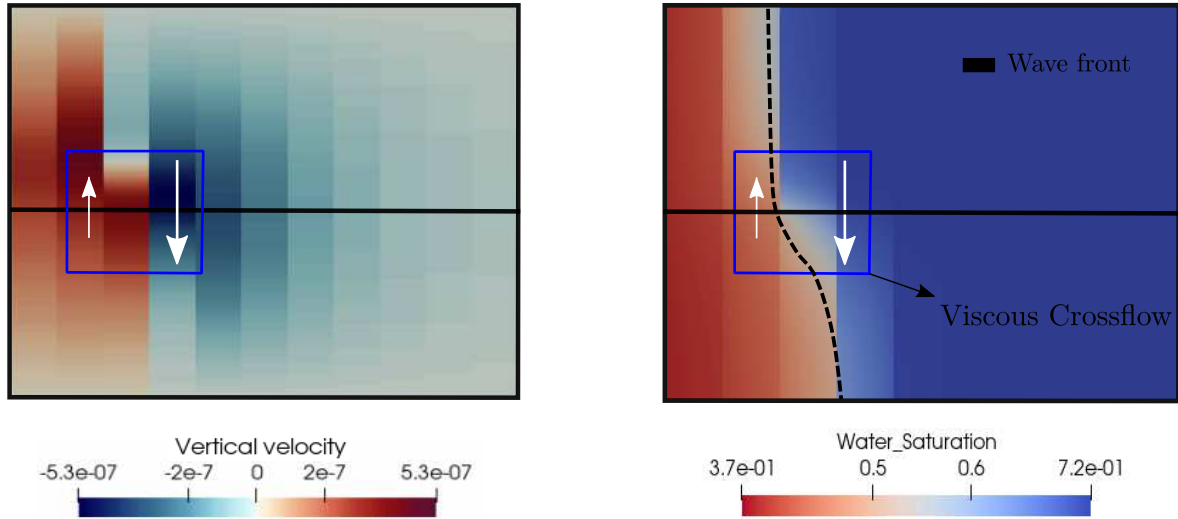


Figure 40 – Vertical velocity field (left panel) and water saturation (right panel) around the traveling wave front at $t = 2000$ [s] for Case I: $\mathcal{K} < \mathcal{P}$. White arrows indicate the mass exchange between layers. The black dashed curve represents the approximate front position.

7.4.2 Case II: $\mathcal{K} = \mathcal{P}$

We consider the permeability ratio of $\mathcal{K} = 2$ and a porosity ratio of $\mathcal{P} = 2$, see Table 10. Equation (7.23) predicts that velocities in layers 1 and 2 (if considered isolated) are equal, *i.e.*, $v_1 = v_2$. The two-dimensional front profile evolution for three different times ($t = 1000, 2000, 3000$ [s] from top to bottom) is shown in Fig. 41. As one can see, both layers present the same front velocity.

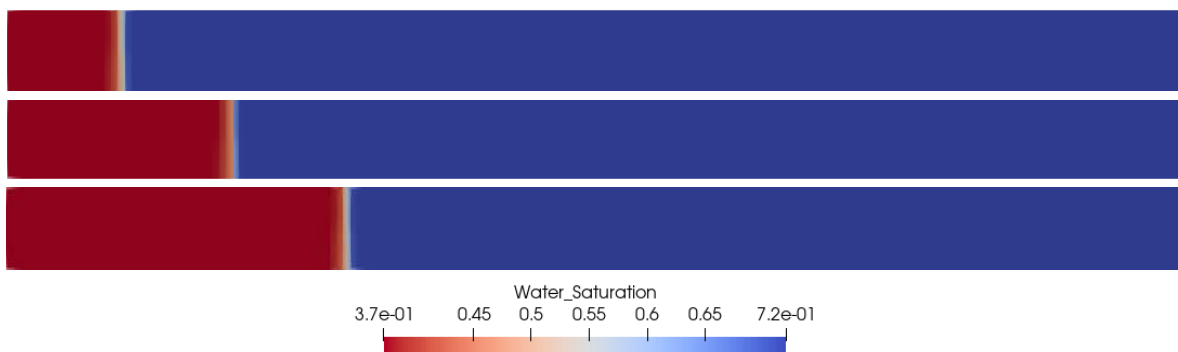


Figure 41 – The water saturation profile obtained simulating Eq. (4.1)-(7.4) for Case II: $\mathcal{K} = \mathcal{P}$ for three times: $t = 1000$ [s] (top), $t = 2000$ [s] (middle), and $t = 3000$ [s] (bottom).

The vertical velocity field around the wavefront at $t = 2000$ [s] is shown in the left panel in Fig. 42. As before, behind the front, we notice an increase in the velocity component pointing from Layer 2 to Layer 1. Ahead of the front, we observe the flow in the opposite direction. The right panel in Figure 42 shows the water saturation front at $t = 2000$ [s], where we schematically indicate the mass exchange between layers. Similar to the previous case, the vertical mass transfer from Layer 2 to Layer 1 is drawn with a

white arrow behind the front and vice versa ahead of the front.

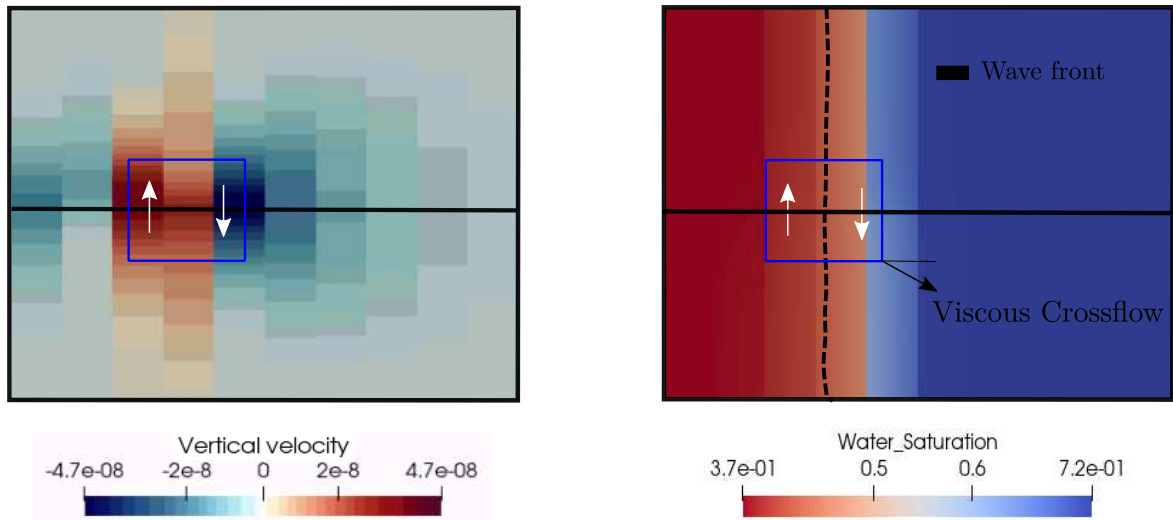


Figure 42 – Vertical velocity field (left panel) and water saturation (right panel) around the traveling wave front at $t = 2000$ [s] for Case II: $\mathcal{K} = \mathcal{P}$. White arrows indicate the mass exchange between layers. The black dashed curve represents the approximate front position.

7.4.3 Case III: $\mathcal{K} > \mathcal{P}$

For this case, we consider permeability ratio $\mathcal{K} = 2$, and porosity ratio $\mathcal{P} = 1.25$, see Table 10. Equation (7.23) suggests that the front velocity in layer 1 is lower than the same in layer 2 (if the layers are considered isolated), *i.e.*, $v_1 > v_2$. The two-dimensional front behavior is observed in Fig. 43 for three times ($t = 3000, 4000, 5000$ [s] from top to bottom). The stabilization time was calculated at $t^* \approx 4000$ [s] (See Fig. 52). Therefore, in the middle and bottom panels, the front behaves like a traveling wave. We also observe that the wavefront in the higher permeability layer is ahead of the front in the lower permeability layer, which is consistent with the predictions given by Eq. (7.23).

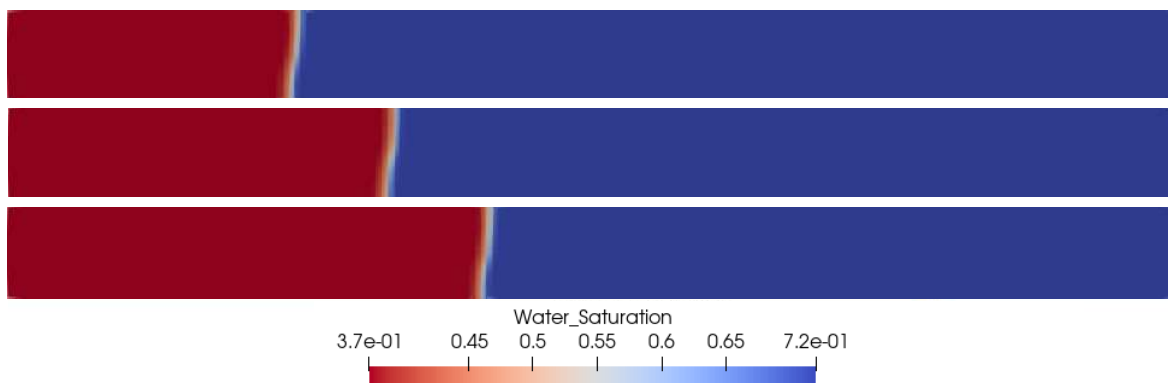


Figure 43 – The water saturation profile obtained simulating Eq. (4.1)-(7.4) for Case III: $\mathcal{K} > \mathcal{P}$ for three times: $t = 3000$ [s] (top), $t^* = 4000$ [s] (middle), and $t = 5000$ [s] (bottom).

The left panel in Fig. 44 shows a zoom of the vertical velocity field around the wavefront. Behind the front, the velocity is negative, which means a mass transfer from the higher permeable layer to the lower and in the opposite direction ahead of the front (depicted with white arrows). In this case, the front velocity in layer 1 is ahead of the same in layer 2. This scenario is similar to the one reported in [104], where the porosity ratio was equal to 1. The right panel in Fig. 44 shows the water saturation profile around the front, where the white arrows represent the mass transfer, with a mass flux from the higher permeable layer to the lower one behind the front and the opposite mass flux ahead of the front.

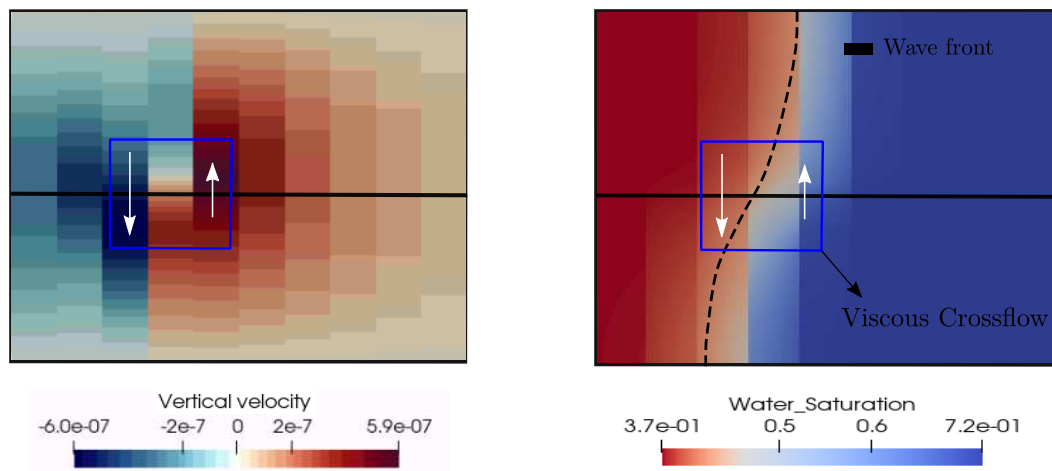


Figure 44 – Vertical velocity field (left panel) and water saturation (right panel) around the traveling wave front at $t = 4000$ [s] for Case III: $\mathcal{K} > \mathcal{P}$. White arrows indicate the mass exchange between layers. The black dashed curve represents the approximate front position.

7.5 Discussion

[31] study two-phase flow in a two-layered configuration varying porosity, absolute permeability, and end-point relative permeabilities to investigate the influence of the viscous cross-flow on the recovery efficiency. The authors classify four flow regimes according to the mobility ratios between layers 1 and 2. In the case of mobilities greater than 1, the fluid crossflow was identified as going from layer 2 to layer 1 behind the front and then from layer 1 to layer 2 ahead of the front. Similar studies were conducted by [65], where the authors investigate two-phase flow considering varying salt concentration in the wetting phase. They classify the different crossflow behaviors depending on the mobility ratios. If the ratio is greater than 1, the crossflow was identified as in [31] (from layer 2 to layer 1 behind and from layer 1 to layer 2 ahead of the front). In both works, the front position in layer 1 is ahead of the same in layer 2.

In the present study, we investigate the two-phase flow in the presence of foam described by Linear Kinetic Model proposed by [8]. As in [31] and [65], we consider the

mobility ratio between layers 1 and 2 greater than 1. We classify the flow regimes according to the ratios between absolute permeabilities and porosities in both layers. To compare our findings with those from [31] and [65], we plot the pressure profiles for each of these cases, see Fig. 45. In Cases I and II, the pressure behavior aligns with those reported in [31] and [65]; however, the saturation front positions are inverted because the porosity ratio (\mathcal{P}) is more influential to the flow than the permeability ratio (\mathcal{K}), see the schematic diagrams in Fig. 45. In Case III, the pressure gradient directions are inverted when compared with [31] and [65] (in our case, the pressure in layer 1 is higher than the one in layer 2 behind the front, and the opposite ahead of the front). In this case, the front position in layer 1 is ahead of the same in layer 2. The differences in the front position and pressure gradient direction between the current work and [31, 65] are due to the presence of foam, which increases the viscosity of the non-wetting phase yielding to the increment of the mass cross-flow. The simulations presented in [104] also correspond to this case.

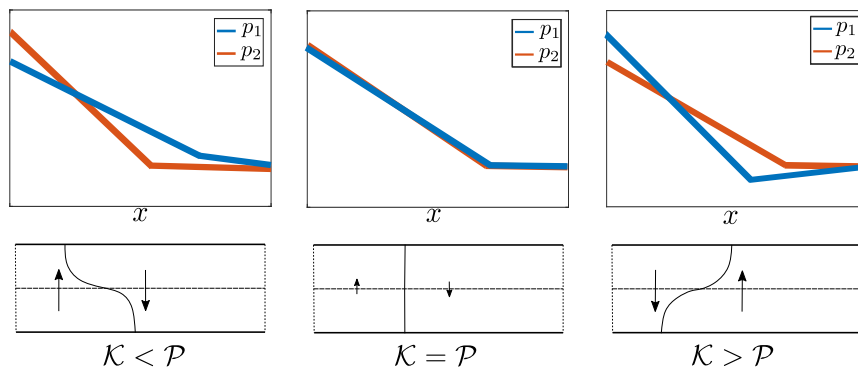


Figure 45 – Schematic representation of the pressure behavior and crossflow regime of both layers in the presence of foam. The top panels compare the total pressure in layers 1 and 2 (p_1 and p_2). In the bottom panels, the arrows represent the direction of mass exchange between the layers, and the continuous curves represent the wavefront shape.

[65] noticed that adding an active tracer could result in the single front formation in both layers, improving the recovery factor. [104] already shown that the presence of foam results in such single front formation. In the current study, we extended these results to the case of varying porosities, showing the single front formation using traveling wave analysis. It is worth noticing that few experimental studies focused on the foam displacement in a two-layer porous medium [83, 13]. None of them reported a single front displacement. In view of the results presented in this work, we argue that this happened because of a huge difference in absolute permeabilities between layers (up to 70 : 1 in [83] and 67 : 1 in [13]). It would be necessary for a several-meter sample to observe such a single front formation incompatible with the laboratory scale. Thus, to observe this phenomenon, it is necessary to consider a smaller contrast in absolute permeabilities between both layers. On the other hand, this is not necessarily a problem on a reservoir scale.

Although measuring the crossflow between layers can be challenging, the present

study shows the alternative in measuring the relative position in the flow front between layers, which is possible to do using the micro CT scan used for similar studies reported in the literature [83, 13, 55, 109].

7.6 Traveling wavefront

[104] showed that the foam displacement in two layers (different permeabilities, same porosities) described by (4.1)-(7.4) happens as a single traveling wave front. Here, we extend these to the case with different porosities in each layer (see Fig. 38). For this purpose, we follow the same steps as in [104] and simplify the two-dimensional model (7.1)-(7.4) considering each layer as a one-dimensional domain. Assuming constant pressure gradients, the simplified one-dimensional model reads:

$$\left\{ \begin{array}{l} \phi_1 \frac{\partial S_{w_1}}{\partial t} + \frac{\partial u_{w_1}}{\partial x} = -\theta_{s_1}(\phi_1 S_{w_1} - \phi_2 S_{w_2}), \\ \phi_1 \frac{\partial (S_{g_1} n_{D_1})}{\partial t} + \frac{\partial (u_{g_1} n_{D_1})}{\partial x} = \phi_1 S_{g_1} \Phi_1, \\ \phi_2 \frac{\partial S_{w_2}}{\partial t} + \frac{\partial u_{w_2}}{\partial x} = \theta_{s_2}(\phi_1 S_{w_1} - \phi_2 S_{w_2}), \\ \phi_2 \frac{\partial (S_{g_2} n_{D_2})}{\partial t} + \frac{\partial (u_{g_2} n_{D_2})}{\partial x} = \phi_2 S_{g_2} \Phi_2, \end{array} \right. \quad (7.24)$$

with constants k_i , θ_{s_i} variables S_{w_i} , S_{g_i} , n_{D_i} , and functions Φ_i , u_{w_i} , u_{g_i} P_{c_i} which are defined for each layer $i = 1, 2$, with

$$S_{w_1} = \int_0^{+d} \frac{S_w(z)}{d} dz, \quad S_{w_2} = \int_{-d}^0 \frac{S_w(z)}{d} dz. \quad (7.25)$$

The initial conditions for the problem (7.24) are in the form of a step function:

$$(S_{w_1}, n_{D_1}, S_{w_2}, n_{D_2})(x, 0) = \begin{cases} (S_{w_1}^-, n_{D_1}^-, S_{w_2}^-, n_{D_2}^-), & \text{if } x < 0 \\ (S_{w_1}^+, n_{D_1}^+, S_{w_2}^+, n_{D_2}^+), & \text{if } x \geq 0 \end{cases}, \quad i = 1, 2. \quad (7.26)$$

Notice that the two-dimensional simulation of the model (4.1)-(7.4), plotted in Figs. 39, 41, 43, suggests the existence of a traveling wave front moving with a constant velocity v . To verify this, we calculate that velocity using the simplified one-dimensional model (7.24) as follows: First, we perform a change of variable to $\eta = x - vt$ and equate the two water mass conservation in (7.24). Then, we integrate with respect to $\eta \in (-\infty, +\infty)$. Finally, isolating v yields the following expression:

$$v = s \left(\frac{u_1 \theta_{s_2} + u_2 \theta_{s_1}}{\phi_1 \theta_{s_2} + \phi_2 \theta_{s_1}} \right), \quad (7.27)$$

where $s = [f_w]/[S_w]$ is the Rankine-Hugoniot jump condition, and $u_i = u_{w_i} + u_{g_i}$ with $i = 1, 2$ and θ_{s_1} and θ_{s_2} are the coefficients describing the mass exchange between layers.

To estimate these coefficients, we follow [114, 26] and consider that mass is conserved in the vertical direction z , with the mass flux due to diffusion. Defining the total mass variation in each layer by R_1 (Layer 1) and R_2 (Layer 2), the conservation of mass translates as $R_1 = -R_2$. In the system of equations (7.24), this indicates that $R_1 = -\theta_{s_1}(\phi_1 S_{w_1} - \phi_2 S_{w_2})$ and $R_2 = \theta_{s_2}(\phi_1 S_{w_1} - \phi_2 S_{w_2})$. On the other hand, from the mass variation formula, we have:

$$R_1 = \frac{\bar{D}_1}{d} \frac{\partial S_w}{\partial z} \Big|_{z \rightarrow 0^-}, \quad R_2 = -\frac{\bar{D}_2}{d} \frac{\partial S_w}{\partial z} \Big|_{z \rightarrow 0^+}, \quad (7.28)$$

where \bar{D}_1 and \bar{D}_2 are positive constants given by

$$\bar{D}_1 = -\lim_{z \rightarrow 0^-} k_1 \lambda_{g_1} f_{w_1} \frac{\partial P_{c_1}}{\partial S_w}, \quad \bar{D}_2 = -\lim_{z \rightarrow 0^+} k_2 \lambda_{g_2} f_{w_2} \frac{\partial P_{c_2}}{\partial S_w}. \quad (7.29)$$

To estimate R_1 and R_2 in (7.28) we assume that S_w is a piecewise quadratic function dependent on z (see Fig. 46), which can be written as:

$$S_w(z) = \begin{cases} a_1 z^2 + b_1 z + c_1, & \text{if } z < 0, \\ a_2 z^2 + b_2 z + c_2, & \text{if } z \geq 0. \end{cases} \quad (7.30)$$

Coefficients a_i , b_i , and c_i can be estimated assuming continuity of $S_w(z)$ at $z = 0$, and no mass loss at the boundaries ($d_z S_w(\pm d) = 0$). For a more detailed discussion on this approximation, see [104]. Substituting (7.30) into (7.28) allows us to calculate the mass exchange coefficients:

$$\theta_{s_1} = \frac{-3\bar{D}_2 \bar{D}_1}{d^2 (\phi_1 \bar{D}_2 + \phi_2 \bar{D}_1)}, \quad \theta_{s_2} = \frac{3\bar{D}_2 \bar{D}_1}{d^2 (\phi_1 \bar{D}_2 + \phi_2 \bar{D}_1)}. \quad (7.31)$$

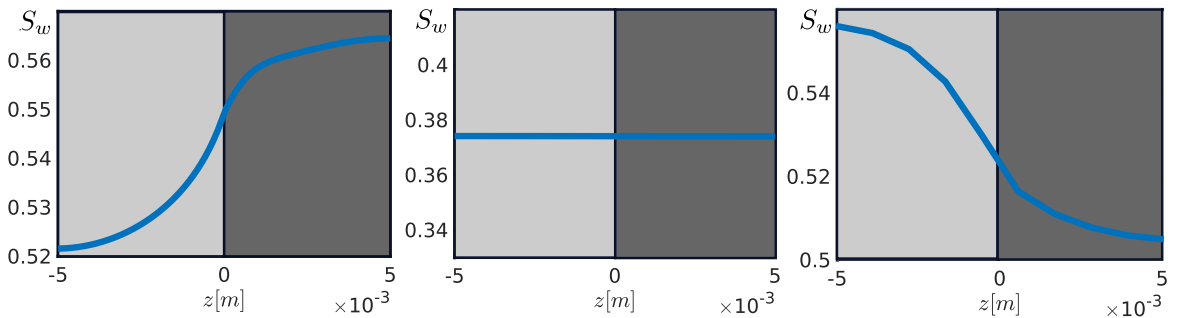


Figure 46 – Average cross-section water saturation profile inside the wavefront obtained from the two-dimensional simulation of Eqs. (4.1)-(7.4) at $t = 5000$ [s], to guarantee that the three fronts are stabilized for Case I (left panel), Case II (middle panel), Case III (right panel). Grey rectangles represent Layer 2 (on the left) and Layer 1 (on the right).

The values of the mass exchange coefficients θ_{s_i} with $i = 1, 2$ and the theoretical velocity v_T calculated from (7.27) for the three cases ($\mathcal{K} < \mathcal{P}$, $\mathcal{K} = \mathcal{P}$, and $\mathcal{K} > \mathcal{P}$) are provided in Table 11. In what follows, we simulate the two-dimensional model (7.1)-(7.4) using FOSSIL (see Appendix 7.7) for these three cases.

Table 11 – Porosity, exchange mass coefficients and theoretical velocity with $k_2 = 1 \times 10^{-12}$ and $k_1 = 2k_2$.

	ϕ_1 [-]	ϕ_2 [-]	θ_{s_i} [-] ($\theta_{s_1} = -\theta_{s_2}$)	Theoretical velocity v_T [m/s]
Case I	0.3	0.1	1.68×10^{-3}	2.31×10^{-5}
Case II	0.3	0.15	1.52×10^{-3}	2.04×10^{-5}
Case III	0.25	0.2	2.55×10^{-3}	2.02×10^{-5}

7.6.1 Case I: $\mathcal{K} < \mathcal{P}$

First, we simulate the two-dimensional model (4.1)-(7.4) using FOSSIL (see Appendix 7.7) obtaining the water saturation profile shown in Fig. 39. To obtain the water saturation front position, we consider the water saturation in each layer at $z = \pm d/2$: $S_{w_1}(x, +d/2, t)$ and $S_{w_2}(x, -d/2, t)$; see the left panel in Fig. 47 for time $t = 2000$ [s]. For each time, we estimate the x -position of the profile by calculating an average x_{S_w} front position corresponding to S_w in the interval $[0.38, 0.41]$. The right panel in Fig. 47 shows the front position evolution for both layers until time $t = 2000$ [s], where it can be observed that the wavefront in layer 2 stays ahead of the wavefront of layer 1.

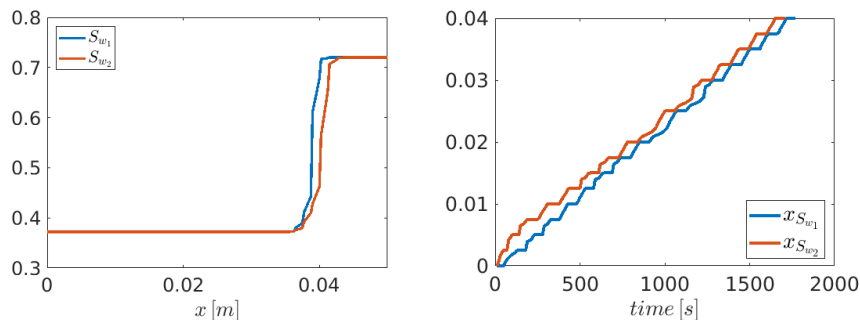


Figure 47 – Case I: $\mathcal{K} < \mathcal{P}$. The water saturation profile of each layer for a time 2000 [s] (left), and the horizontal position of the water saturation front (right).

Using the front position inside each layer, we calculate each front velocity as $v(t) = (x_{S_w}(t + \delta t) - x_{S_w}(t))/\delta t$. To control numerical oscillations, we regularize the velocity by using the mobile average as in [104]. The resulting velocities in each layer are shown in the left panel in Fig. 48. To better estimate the time ($t^* \approx 2000$ [s]) simulation takes to stabilize, we analyze the standard deviation in velocity values for each layer as plotted in the right panel in Fig. 48.

7.6.2 Case II: $\mathcal{K} = \mathcal{P}$

As in the previous case, we simulate the two-dimensional model (7.1)-(7.4) using FOSSIL (see Appendix 7.7) obtaining the water saturation profile shown in Fig. 41. As in Case I, the water saturation front position is plotted in the left panel in Fig. 49 for time $t = 2000$ [s]. The right panel in Fig. 49 shows the front position evolution for both layers until time $t = 2000$ [s], where it can be observed that both wavefronts move together.

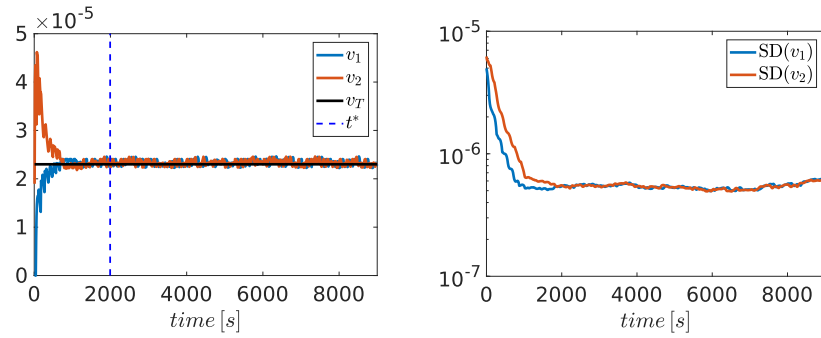


Figure 48 – Case I: $\mathcal{K} < \mathcal{P}$. Numerical estimation of the velocities v_1 and v_2 of the water saturation fronts in each layer (left). The black straight line represents the theoretical velocity v_T calculated using Eq. (7.27). The standard deviation of the velocities in each layer (right). The estimated time when these curves stabilize is t^* .

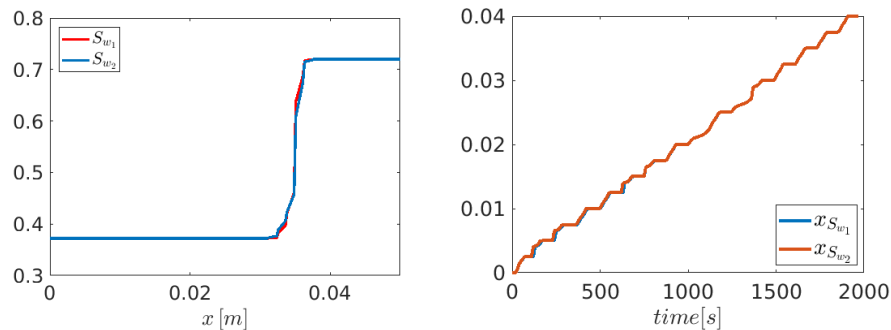


Figure 49 – Case II: $\mathcal{K} = \mathcal{P}$. The saturation profile of each layer for a time 2000 [s] (left), and the horizontal position of water saturation front (right).

The regularized velocities in each layer are shown in the left panel in Fig. 50. To better estimate the time ($t^* \approx 2000$ [s]) simulation takes to stabilize, we analyze the standard deviation in velocity values for each layer as plotted in the right panel in Fig. 50.

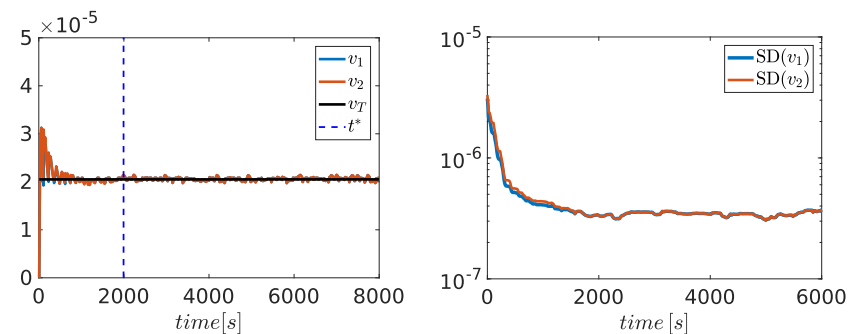


Figure 50 – Case II: $\mathcal{K} = \mathcal{P}$. Numerical estimation of the velocities v_1 and v_2 of the water saturation fronts in each layer (left). The black straight line represents the theoretical velocity v_T calculated using Eq. (7.27). The standard deviation of each of the velocities (right). The time when these curves stabilize is t^* .

7.6.3 Case III: $\mathcal{K} > \mathcal{P}$

As in the previous cases, we simulate the two-dimensional model (7.1)-(7.4) using FOSSIL (see Appendix 7.7) obtaining the water saturation profile shown in Fig. 43. The water saturation front position is plotted in the left panel in Fig. 51 for time $t = 4000$ [s]. The right panel in Fig. 51 shows the front position evolution for both layers until time $t = 4000$ [s], where it can be observed that the wavefront in layer 1 stays ahead of the wavefront of layer 2.

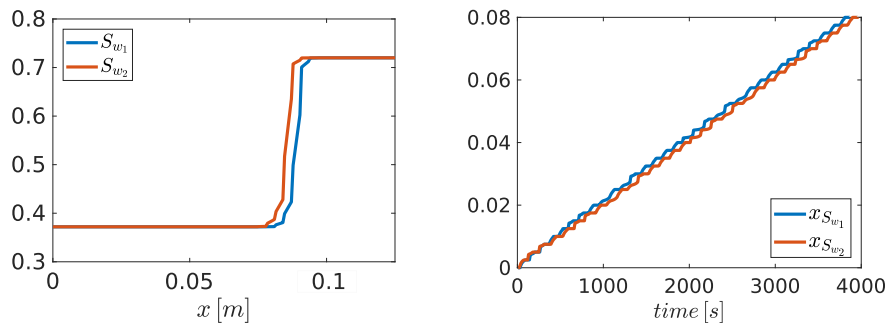


Figure 51 – Case III: $\mathcal{K} > \mathcal{P}$. The saturation profile of each layer for a time 4000 [s] (left), and horizontal position of water saturation front (right).

The regularized velocities in each layer are shown in the left panel in Fig. 52. To better estimate the time ($t^* \approx 2000$ [s]) simulation takes to stabilize, we analyze the standard deviation in velocity values for each layer as plotted in the right panel in Fig. 52.

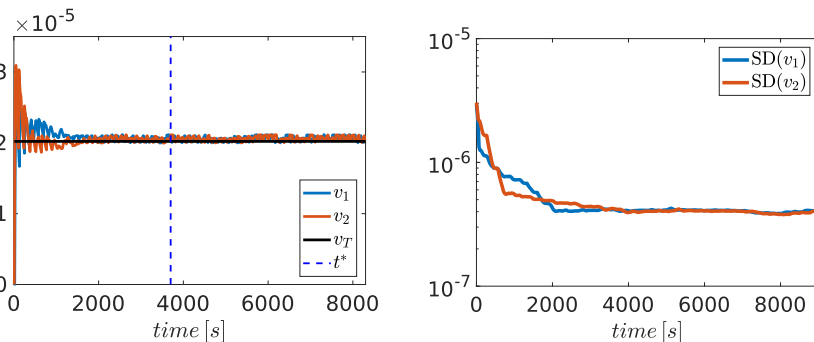


Figure 52 – Case III $\mathcal{K} > \mathcal{P}$. Numerical estimation of the velocities v_1 and v_2 of the water saturation fronts in each layer (left). The black straight line represents the theoretical velocity v_T calculated using Eq. (7.27). The standard deviation of each of the velocities (right). The time when these curves stabilize is t^* .

7.7 Foam flow simulator

The system of Eqs. (7.1)-(7.4) is solved using Foam Displacement Simulator (FOSSIL) presented by [29, 30]. This numerical solver employs the KNP conservative method to solve water mass conservation Eq. (7.1) and foam transport Eq. (7.2), see [62, 64].

Eqs. (7.3) and (7.4) are solved using the conservative finite element method proposed by [92].

We configure FOSSIL with the two communicating layer geometry, following Fig. 38. We discretize the interval $(-d, d)$ in the z -direction in N_z number of cells separated by a step size of Δz and the interval $(0, L)$ in the x -direction with N_x number of cells separated by a step size of Δx . We discretize the time domain with N_T . The coordinates of each z -point are $z^j = (j - 1)\Delta z - d$ with $j = 1, 2, \dots, N_z + 1$, and x -points are located at $x^m = (m - 1)\Delta x$ with $m = 1, 2, \dots, N_x + 1$. To avoid a mesh partition located in the boundary between two layers (see the traced line in Fig. 53), we adopt an even number N_z ; thus, a partition located in the thin layer in z -direction takes half one layer and half of another one. It should be noticed that a z -partition situated above the thin traced line layer is taken petrophysical properties k_1, ϕ_1 and that situated below is taken k_2, ϕ_2 .

Figure 53 depicts a schematic numerical domain discretization used to configure FOSSIL.

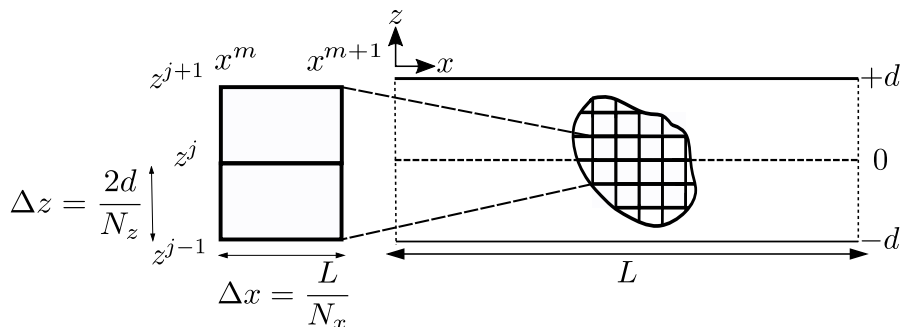


Figure 53 – Schematic discretization of the numerical domain used to configure the numerical foam flow simulator FOSSIL.

7.8 Partial conclusions

Using the traveling wave solution, we classify the flow in a two-layer porous medium in the presence of foam depending on the absolute permeability ratio between layers (\mathcal{K}) and the porosity ratio between layers (\mathcal{P}). For case I ($\mathcal{K} < \mathcal{P}$), the front position in layer 2 is ahead of the same in layer 1. In this case, ahead of the front, the mass flow direction is from the high permeability layer to the lower permeability layer and behind the front in the opposite direction. In case II ($\mathcal{K} = \mathcal{P}$), fronts in both layers displace together, and the mass cross flow between layers follows the same rule as in Case I with lower transfer rates. In case III ($\mathcal{K} > \mathcal{P}$), the front position in layer 1 is ahead of the same in layer 2. In this case, ahead of the front, the mass flow direction is from the lower permeability layer to the high permeability layer and behind the front in the opposite direction. We conclude that the porosity difference between layers impacts the mass cross-flow.

In the previous work, [104] observed that the foam presence results in a single flow front in both layers with different permeabilities and the same porosities. In the present study, we extended this result to the case of varying porosities.

8 CONCLUSIONS

In this thesis work, we study the behavior of foam injection in stratified porous media; At this time, an article has been published at a conference, one article in an international journal, and two more articles have been submitted.

In Chapter 4, we consider incompressibility and immiscibility of fluids, and layers with different permeabilities and equal porosities. The study numerically demonstrates that in a porous medium with two layers of different permeabilities, foam forms a single displacement wave with a velocity corresponding to the weighted average of front velocities in each layer, as if these layers were considered isolated. A simplified one-dimensional model was developed, verified, and validated through numerical simulations. An analytical formula for estimating mass exchange between layers was proposed, along with an estimation of the time required for wavefront stabilization, confirming its validity in one-dimensional and two-dimensional models. These findings suggest that foams can effectively control gas mobility in multilayer porous media.

In Chapter 5, we examined foam displacement in three-layer stratified porous media with a bubble population model. Using a two-dimensional in-house numerical simulator, we found that the water saturation profile forms a stable traveling wave solution. When a highly permeable middle layer approaches fracture, our results suggest that foam displacement in porous media with fractures exhibits behavior similar to that in homogeneous conditions.

In Chapter 6, we demonstrated that the foam presence induces the formation of a single traveling wavefront in a fractured porous medium, where the fracture is modeled as a thin, highly permeable layer surrounded by two thicker layers. To support our findings, we explored two scenarios: in the first, the permeabilities of the two outer layers are equal, while the second, more realistic scenario involves different permeabilities. In both scenarios, a single traveling foam wavefront is formed, avoiding the dominant gas flow through the fracture and improving sweep efficiency. To conduct the analysis, we extended previous results that showed the formation of a single traveling wave in a two-layer porous medium to that of an n -layer porous medium. We derived an analytical formula for the wavefront velocity for n layers and validated it through simulations in a realistic two-dimensional model. This formula provides an estimate of the front propagation velocity in a stratified medium, allowing a preview of gas breakthrough time, which is crucial information in many applications. Notice that, in the absence of foam, it is not possible to observe the formation of such a traveling wave on the laboratory scale due to large flow velocities.

In Chapter 7, using the traveling wave solution, we classify flow in a two-layer porous medium in the presence of foam based on the absolute permeability ratio between layers (\mathcal{K}) and the porosity ratio between layers (\mathcal{P}). In Case I ($\mathcal{K} < \mathcal{P}$), the front in layer

2 advances ahead of layer 1, with mass flow from high permeability to low permeability in front of the front and in the opposite direction behind it. In Case II ($\mathcal{K} = \mathcal{P}$), both fronts progress together, with mass crossflow following a similar rule to Case I but at lower transfer rates. In Case III ($\mathcal{K} > \mathcal{P}$), the front in layer 1 is ahead of layer 2, with mass flow from low permeability to high permeability in front of the front and in the opposite direction behind it. We conclude that the difference in porosity between layers impacts mass crossflow. In previous studies, it was observed that the presence of foam results in a single flow front in both layers with different permeabilities and the same porosities. In this study, we extended this result to the case of varying porosities.

In general, the results obtained in this thesis provide simple analytical estimates for foam flow in a multi-layered porous medium. They can be used as a starting point for further investigations including sensitivity analysis and uncertainty quantification.

Finally, it is important to note that the major limitation of our analysis is the assumption that mass exchange between layers is only due to viscous crossflow.

8.1 Academic contributions

During the development of the present thesis, different academic contributions were realized.

- . Articles published in conference proceedings, [102].
 - A. J. Castrillón Vasquez and G. Chapiro. Wavefront velocity for foam flow in three-layer porous media. Proceedings of the XLIII Ibero-Latin-American Congress on Computational Methods in Engineering CILAMCE, ABMEC Foz do Iguaçu, Brazil, November 21-25, 2022.
- . Complete articles published in journals, [104].
 - A. J. Castrillon Vasquez, L. F. Lozano, W. Pereira, J. B. Cedro, and G. Chapiro. The traveling wavefront for foam flow in two-layer porous media. COMG, 2022.
- . Submitted articles in journals, [103, 105].
 - A. J. Castrillon Vasquez, L. F. Lozano, and G. Chapiro. The traveling foam wavefront in fractured porous medium. Submitted, 2023.
 - A. J. Castrillon Vasquez, P. Z. S. Paz, and G. Chapiro. On the viscous crossflow during the foam displacement in two-layered porous media. Submitted, 2023.
- . Presentations:

- “Wavefront velocity for foam flow in three-layer porous media”. November 21-25, 2022. Presented by A. J. Castrillón Vásquez. XLIII Ibero-Latin-American Congress on Computational Methods in Engineering CILAMCE, ABMEC Foz do Iguaçu, Brazil.

REFERENCES

- [1] Pierre M Adler and J-F Thovert. *Fractures and fracture networks*, volume 15. Springer, Haifa, 1999.
- [2] Shokufe Afzali, Nima Rezaei, and Sohrab Zendehboudi. A comprehensive review on enhanced oil recovery by water alternating gas (wag) injection. *Fuel*, 227:218–246, 2018.
- [3] Emad W Al-Shalabi and B Ghosh. Effect of pore-scale heterogeneity and capillary-viscous fingering on commingled waterflood oil recovery in stratified porous media. *Journal of Petroleum Engineering*, 2016, 2016.
- [4] M.R. Alhamdan, Y. Cinar, V.S. Suicmez, and B. Dindoruk. Experimental and numerical study of compositional two-phase displacements in layered porous media. *Journal of Petroleum Science and Engineering*, 98:107–121, 2012.
- [5] B. I. AlQuaimi and W. R. Rossen. Foam generation and rheology in a variety of model fractures. *Energy & Fuels*, 33(1):68–80, 2019.
- [6] D. Arndt, W. Bangerth, B. Blais, T. C. Clevenger, M. Fehling, A. V. Grayver, T. Heister, L. Heltai, M. Kronbichler, M. Maier, P. Munch, J.-P. Pelteret, R. Rastak, I. Thomas, B. Turcksin, Z. Wang, and D. Wells. The deal.II library, version 9.2. *Journal of Numerical Mathematics*, 2020.
- [7] E. Ashoori, D. Marchesin, and W. R. Rossen. Dynamic foam behavior in the entrance region of a porous medium. *Colloids and Surfaces A: Physicochemical and Engineering Aspects*, 377:217–227, 2011.
- [8] E. Ashoori, D. Marchesin, and W. R. Rossen. Roles of transient and local equilibrium foam behavior in porous media: traveling wave. *Colloids and Surfaces A: Physicochemical and Engineering Aspects*, 377:228–242, 2011.
- [9] J. Bear. *Modeling Phenomena of Flow and Transport in Porous Media*. Theory and Applications of Transport in Porous Media. Springer International Publishing, 2018.
- [10] F. R. Behenna. Acid diversion from an undamaged to a damaged core using multiple foam slugs. In *SPE - European Formation Damage Conference, Proceedings, EFDC*, volume 1995-May, pages 441–452. Society of Petroleum Engineers, 1995.
- [11] H. Bertin, E. Estrada, and O. Atteia. Foam placement for soil remediation. *Environ. Chem.*, 14:338–343, 2017.
- [12] H. J. Bertin, O. G. Apaydin, L. M. Castanier, and A. R. Kovscek. Foam flow in heterogeneous porous media: Effect of cross flow. *SPE Journal*, 4(02):75–82, 06 1999.
- [13] Henri Bertin, Estefania Del Campo Estrada, and Olivier Atteia. Foam placement for soil remediation. *Environmental Chemistry*, 14(5):338–343, 2017.
- [14] J.J. Bikerman. *Foams*. Springer-Verlag, New York, 1973.
- [15] C. S. Boeiije and W. R. Rossen. SAG foam flooding in carbonate rocks. *Journal of Petroleum Science and Engineering*, 171:843 – 853, 2018.

- [16] Johannes Bruining. *Upscaling of Single- and Two-Phase Flow in Reservoir Engineering*. CRC Press, Delft, The Netherlands, 2021.
- [17] J. W. Burman and B. E. Hall. Foam as a diverting technique for matrix sandstone stimulation. In *Society of Petroleum Engineers of AIME, (Paper) SPE*, pages SPE–15575. Society of Petroleum Engineers, 1986.
- [18] E. J. Carr. New semi-analytical solutions for advection–dispersion equations in multilayer porous media. *Transport in Porous Media*, 135:39–58, 2020.
- [19] E. J. Carr and I. W. Turner. A semi-analytical solution for multilayer diffusion in a composite medium consisting of a large number of layers. *Appl. Math. Model.*, 40:7034–7050, 2016.
- [20] J. B. Cedro, R. V. Quispe, M. C. Coaquira, L. F. Lozano, and G. Chapiro. Estudo de um modelo cinético para escoamento de espuma em meios porosos. In *XL Ibero-Latin-American Congress on Computational Methods in Engineering (CILAMCE)*, pages 1–13, Natal, Brazil, 2019.
- [21] B Cepeda-Salgado, GS Lee, I Gupta, C Willson, and SI Kam. Surfactant/foam processes in shallow subsurface remediation: Evaluation of foams as a blocking agent. *Transport in Porous Media*, pages 709–732, 2023.
- [22] Q. Chen, A. Kovscek, and M. Gerritsen. Modeling foam displacement with the local-equilibrium approximation: theory and experimental verification. *SPE Journal*, 15(01):171–183, 2010.
- [23] Z. Chen, G. Huan, and Y. Ma. *Computational Methods for Multiphase Flows in Porous Media*. SIAM, Dallas, 2006.
- [24] A. T. Corey. The interrelation between gas and oil relative permeabilities. *Producers monthly*, 19(1):38–41, 1954.
- [25] John H Cushman. *The physics of fluids in hierarchical porous media: Angstroms to miles*, volume 10. Springer Science & Business Media, Indiana, 2013.
- [26] Wesley da Silva Pereira and Grigori Chapiro. Traveling wave solutions for non-newtonian foam flow in porous media. *Transport in Porous Media*, 148:247–265, 2023.
- [27] L. P. Dake. *Fundamentals of reservoir engineering*. Elsevier, Amsterdam, 1983.
- [28] Yohan Davit, Christopher G. Bell, Helen M. Byrne, Lloyd A.C. Chapman, Laura S. Kimpton, Georgina E. Lang, Katherine H.L. Leonard, James M. Oliver, Natalie C. Pearson, Rebecca J. Shipley, Sarah L. Waters, Jonathan P. Whiteley, Brian D. Wood, and Michel Quintard. Homogenization via formal multiscale asymptotics and volume averaging: How do the two techniques compare? *Advances in Water Resources*, 62:178–206, 2013.
- [29] F. F. de Paula, T. Quinelato, I. Igreja, and G. Chapiro. A numerical algorithm to solve the two-phase flow in porous media including foam displacement. *Lecture Notes in Computer Science*, 12143:18–31, 2020.

- [30] Filipe F. de Paula, Iury Igreja, Thiago Quinelato, and Grigori Chapiro. A numerical investigation into the influence of the surfactant injection technique on the foam flow in heterogeneous porous media. *Advances in Water Resources*, 171:104358, 2023.
- [31] Y. Debbabi, M. Jackson, G. Hampson, P. Fitch, and P. Salinas. Viscous crossflow in layered porous media. *Transport in Porous Media*, 117:1573–1634, 2017.
- [32] Yacine Debbabi, Matthew D Jackson, Gary J Hampson, and Pablo Salinas. Capillary heterogeneity trapping and crossflow in layered porous media. *Transport in Porous Media*, 120:183–206, 2017.
- [33] P. Dietrich, R. Helmig, M. Sauter, H. Hötzl J. Köngeter, and G. Teutsch. *Flow and Transport in Fractured Porous Media.*, volume 1. Springer, Berlin, 2005.
- [34] Dongxing Du, Na Zhang, Yingge Li, Rui Sun, and Chengcheng Wang. Parametric studies on foam displacement behavior in a layered heterogeneous porous media based on the stochastic population balance model. *Journal of Natural Gas Science and Engineering*, 48:1–12, 2017.
- [35] A. A. Eftekhari and R. Farajzadeh. Effect of foam on liquid phase mobility in porous media. *Scientific reports*, 7:43870, 2017.
- [36] E. Campo Estrada, Henri Bertin, and Olivier Atteia. Experimental study of foam flow in sand columns: Surfactant choice and resistance factor measurement. *Transport in Porous Media*, 108:335–354, 2015.
- [37] R. Farajzadeh, A. Andrianov, R. Krastev, G. Hirasaki, and W. Rossen. Foam–oil interaction in porous media: implications for foam assisted enhanced oil recovery. *Advances in colloid and interface science*, 183:1–13, 2012.
- [38] Alessio Fumagalli and Anna Scotti. A mathematical model for thermal single-phase flow and reactive transport in fractured porous media. *Journal of Computational Physics*, 434:110–205, 2021.
- [39] Margot G. Gerritsen and Louis J. Durlofsky. Modeling fluid flow in oil reservoirs. *Annual Review of Fluid Mechanics*, 37(1):211–238, 2005.
- [40] A.R. Ghazaryan, S. Lafortune, and V. Manukian. *Introduction to Traveling Waves*. A Chapman & Hall book. CRC Press, Boca Raton, 2022.
- [41] D. W. Green and G. P. Willhite. *Enhanced oil recovery*, volume 6. Henry L. Doherty Memorial Fund of AIME, Society of Petroleum Engineers, Columbia, 1998.
- [42] J. Guckenheimer and P. Holmes. *Nonlinear Oscillations, Dynamical Systems, and Bifurcations of Vector Fields*. Springer-Verlag, New York, 1986.
- [43] J. Guckenheimer and P. Holmes. *Dynamical systems and bifurcations of vector fields.*, volume 1. Springer, 2002.
- [44] J. S. P. Guerrero, L. C. G. Pimentel, and T. H. Skaggs. Analytical solution for the advection-dispersion transport equation in layered media. *Heat Mass Transf*, 56:274–282, 2013.

- [45] Willi Gujer. *Systems analysis for water technology*. Springer Science & Business Media, Zurich, 2008.
- [46] H. Hematpur, S. M. Mahmood, N. H. Nasr, and K. A. Elraies. Foam flow in porous media: Concepts, models and challenges. *Journal of Natural Gas Science and Engineering*, 53:163–180, 2018.
- [47] A. C. Hindmarsh, P. N. Brown, K. E. Grant, S. L. Lee, R. Serban, D. E. Shumaker, and C. S. Woodward. SUNDIALS: Suite of nonlinear and differential/algebraic equation solvers. *ACM Trans. on Math. Software*, 31(3):363–396, 2005.
- [48] G. J. Hirasaki. A review of the steam foam process mechanisms, 1989. Paper SPE 19518.
- [49] G. J. Hirasaki and J. B. Lawson. Mechanisms of foam flow in porous media: apparent viscosity in smooth capillaries. *SPE Journal*, 25(02):176–190, 1985.
- [50] G. J. Hirasaki, C. A. Miller, R. Szafranski, J. B. Lawson, and N. Akiya. Surfactant/foam process for aquifer remediation. In *International symposium on oilfield chemistry*, pages SPE–37257–MS. Society of Petroleum Engineers, 1997.
- [51] Helge Holden and Nils Henrik Risebro. *Front Tracking for Hyperbolic Conservation Laws*. Springer, Berlin, 2015.
- [52] Randi Holm, Marinus IJ van Dijke, and Sebastian Geiger. Three-phase flow modelling using pore-scale capillary pressures and relative permeabilities for mixed-wet media at the continuum-scale. *Transport in porous media*, 81(3):423–442, 2010.
- [53] M. T. G. Janssen, R. M. Pilus, and P. L. J. Zitha. A comparative study of gas flooding and foam-assisted chemical flooding in Bentheimer sandstones. *Transport in Porous Media*, 131(1):101–134, 2020.
- [54] M. T. G. Janssen, F. A. Torres Mendez, and P. L. J. Zitha. Mechanistic modeling of water-alternating-gas injection and foam-assisted chemical flooding for enhanced oil recovery. *Industrial & Engineering Chemistry Research*, 59(8):3606–3616, 2020.
- [55] S. A. Jones, G. Laskaris, S. Vincent-Bonnieu, R. Farajzadeh, and W. R. Rossen. Effect of surfactant concentration on foam: From coreflood experiments to implicit-texture foam-model parameters. *Journal of Industrial and Engineering Chemistry*, 37:268–276, 2016.
- [56] S. I. Kam, Q. P. Nguyen, Q. Li, and W. R. Rossen. Dynamic simulations with an improved model for foam generation. *SPE Journal*, 12(1):35–48, 2007.
- [57] Z. I. Khatib, G. J. Hirasaki, and A. H. Falls. Effects of capillary pressure on coalescence and phase mobilities in foams flowing through porous media. *SPE Reservoir Engineering*, 3(3):919–926, 1988.
- [58] A. R. Kovscek and H. J. Bertin. Verification of roof snap off as a foam-generation mechanism in porous media at steady state. *Colloids Surf. A Physicochem. Eng. Asp.*, 302(1):251–260, 2007.

- [59] A. R. Kavscek, T. W. Patzek, and C. J. Radke. A mechanistic population balance model for transient and steady-state foam flow in Boise sandstone. *Chemical Engineering Science*, 50(23):3783–3799, 1995.
- [60] A. R. Kavscek, H. Wong, and C. J. Radke. A pore-level scenario for the development of mixed wettability in oil reservoirs. *AIChE Journal*, 39(6):1072–1085, 1993.
- [61] Kundan Kumar, Florian List, Iuliu Sorin Pop, and Florin Adrian Radu. Formal upscaling and numerical validation of unsaturated flow models in fractured porous media. *Journal of Computational Physics*, 407:109138, 2020.
- [62] A. Kurganov, S. Noelle, and G. Petrova. Semidiscrete central-upwind schemes for hyperbolic conservation laws and Hamilton-Jacobi equations. *SIAM Journal on Scientific Computing*, 23(3):707–740, 2001.
- [63] A. Kurganov, Z. Qu, O. S. Rozanova, and T. Wu. Adaptive moving mesh central-upwind schemes for hyperbolic system of PDEs: Applications to compressible Euler equations and granular hydrodynamics. *Communications on Applied Mathematics and Computation*, 3(3):445–479, 2021.
- [64] A. Kurganov and E. Tadmor. New high-resolution central schemes for nonlinear conservation laws and convection-diffusion equations. *Journal of Computational Physics*, 160(1):241–282, 2000.
- [65] Lekan Ladipo, Martin J Blunt, and Peter R King. Crossflow effects on low salinity displacement in stratified heterogeneity. *Journal of Petroleum Science and Engineering*, 208:109565, 2022.
- [66] L. Lake. *Enhanced oil recovery*. Prentice Hall, New Jersey, 1989.
- [67] W. Lambert, A. Alvarez, I. Ledoino, D. Tadeu, D. Marchesin, and J. Bruining. Mathematics and numerics for balance partial differential-algebraic equations (PDAEs). *Journal of Scientific Computing*, 84(2):1–56, 2020.
- [68] Brodie A.J. Lawson, Rodrigo Weber dos Santos, Ian W. Turner, Alfonso Bueno-Orovio, Pamela Burrage, and Kevin Burrage. Homogenisation for the monodomain model in the presence of microscopic fibrotic structures. *Communications in Nonlinear Science and Numerical Simulation*, 116:106794, 2023.
- [69] F. J. Leij and M. Th. Van Genuchten. Approximate analytical solutions for solute transport in two-layer porous media. *Transport in Porous Media*, 18(1):65–85, jan 1995.
- [70] R. J. LeVeque. *Numerical Methods for Conservation Laws*. Birkhäuser Basel, Basel, 1990.
- [71] M. C. Leverett. Capillary behavior in porous solids. *Trans. AIME*, 142(01):152–169, 1941.
- [72] Kai Li, Karl-Heinz AA Wolf, and William R Rossen. Effects of gas trapping on foam mobility in a model fracture. *Transport in Porous Media*, 138(1):185–200, 2021.

- [73] Q. Li and W. R. Rossen. Injection strategies for foam generation in homogeneous and layered porous media. In *SPE Annual Technical Conference and Exhibition*, pages 1–18. SPE, 2005.
- [74] C. Liu, W.P. Ball, and J.H. Ellis. An analytical solution to the one-dimensional solute advection-dispersion equation in multi-layer porous media. *Transp. Porous Med.*, 30:25–43, 1998.
- [75] L. F. Lozano, J. B. Cedro, R. Q. Zavala, and G. Chapiro. How simplifying capillary effects can affect the traveling wave solution profiles of the foam flow in porous media. *International Journal of Non-Linear Mechanics*, 139:103867, 2022.
- [76] L. F. Lozano, R. Q. Zavala, and G. Chapiro. Mathematical properties of the foam flow in porous media. *Computational Geosciences*, 25(1):515–527, 2021.
- [77] K. Ma, G. Ren, K. Mateen, D. Morel, and P. Cordelier. Modeling techniques for foam flow in porous media. *SPE Journal*, 20(3):453–470, 2015.
- [78] Kun Ma, Khalid Mateen, Guangwei Ren, Haishan Luo, Gilles Bourdarot, and Danielle Morel. Mechanistic modeling of foam flow through porous media in the presence of oil: Review of foam-oil interactions and an improved bubble population-balance model. In *SPE Annual Technical Conference and Exhibition*, page D031S031R004. Society of Petroleum Engineers, 2018.
- [79] Simon A Mathias, Paul E Hardisty, Mark R Trudell, and Robert W Zimmerman. Approximate solutions for pressure buildup during CO₂ injection in brine aquifers. *Transport in Porous Media*, 79(2):265–284, 2009.
- [80] Bert Metz, Ogunlade Davidson, HC De Coninck, Manuela Loos, and Leo Meyer. *IPCC special report on carbon dioxide capture and storage*. Cambridge: University press, New York, 2005.
- [81] JC Da Mota and Stephen Schechter. Combustion fronts in a porous medium with two layers. *Journal of dynamics and differential equations*, 18:615–665, 2006.
- [82] C.N. Mulligan. Recent advances in the environmental applications of biosurfactants. *Current Opinion in Colloid & Interface Science*, 14(5):372–378, 2009.
- [83] Quoc P. Nguyen, Alexander V. Alexandrov, Pacelli L. Zitha, and Peter K. Currie. Experimental and modeling studies on foam in porous media: A review. *SPE Journal*, 2000. SPE-58799-MS.
- [84] Quoc P. Nguyen, Peter K. Currie, Marten Buijse, and Pacelli L.J. Zitha. Mapping of foam mobility in porous media. *Journal of Petroleum Science and Engineering*, 58(1):119–132, 2007.
- [85] Quoc P. Nguyen, Peter K. Currie, and Pacelli L. J. Zitha. Effect of crossflow on foam-induced diversion in layered formations. *SPE Journal*, 10(01):54–65, 03 2005.
- [86] GG Pereira. Fluid flow, relative permeabilities and capillary pressure curves through heterogeneous porous media. *Applied Mathematical Modelling*, 75:481–493, 2019.

- [87] W.S. Pereira and Grigori Chapiro. Numerical validation of analytical estimates for propagation of thermal waves generated by gas-solid combustion. *Geofluids*, 2017, 2017.
- [88] L. Perko. *Differential equations and dynamical system*. Springer, Pasadena, 2015.
- [89] AK Permadi, IP Yuwono, and AJS Simanjuntak. Effects of vertical heterogeneity on waterflood performance in stratified reservoirs: a case study in bangko field, indonesia. In *SPE Asia pacific conference on integrated modelling for asset management*, pages SPE–87016, 2004.
- [90] P. Persoff, C. J. Radke, K. Pruess, S. M. Benson, and P. A. Witherspoon. A laboratory investigation of foam flow in sandstone at elevated pressure. In *SPE California Regional Meeting*, pages SPE–18781. Society of Petroleum Engineers, 1989.
- [91] J. L. Randall. Numerical methods for conservation laws. *Lectures in Mathematics ETH Zürich*, 1992.
- [92] P. A. Raviart and J. M. Thomas. A mixed finite element method for 2-nd order elliptic problems. In I. Galligani and E. Magenes, editors, *Mathematical Aspects of Finite Element Methods*, volume 606, pages 292–315. Springer, 1977.
- [93] WJ Renkema and WR Rossen. Success of sag foam processes in heterogeneous reservoirs. In *SPE annual technical conference and exhibition*, pages cp–147. OnePetro, 2007.
- [94] M. R. Rodrigo and A. L. Worthy. Solution of multilayer diffusion problems via the laplace transform. *J. Math. Anal. Appl*, 444:475–502, 2016.
- [95] A. Rosman and S. I. Kam. Modeling foam-diversion process using three-phase fractional flow analysis in a layered system. *Energy Sources, Part A: Recovery, Utilization, and Environmental Effects*, 31(11):936–955, 2009.
- [96] W. R. Rossen. Numerical challenges in foam simulation: A review. In *Proceedings - SPE Annual Technical Conference and Exhibition*, pages 1–10. Society of Petroleum Engineers, 2013.
- [97] Hamidreza Salimi, Karl-Heinz Wolf, and Johannes Bruining. The influence of capillary pressure on the phase equilibrium of the CO₂–water system: Application to carbon sequestration combined with geothermal energy. *International Journal of Greenhouse Gas Control*, 11:S47–S66, 2012.
- [98] M. Simjoo and P. L. J. Zitha. Modeling of foam flow using stochastic bubble population model and experimental validation. *Transport in Porous Media*, 107(3):799–820, 2015.
- [99] I. S. Sominskii. *The method of mathematical induction*. Popular lectures in mathematics series. Blaisdell publishing company, New York, 1961.
- [100] D. Tanzil, G. J. Hirasaki, and C. A. Miller. Mobility of foam in heterogeneous media: Flow parallel and perpendicular to stratification. *SPE Journal*, 7:203–212, 2002.

- [101] C. J. van Duijin. *An introduction to conservation laws: theory and applications to multi-phase flow*. Eindhoven University of Technology, Eindhoven, 2003.
- [102] A. J. Castrillon Vasquez and G. Chapiro. Wavefront velocity for foam flow in three-layer porous media. *XLIII Ibero- Latin-American Congress on Computational Methods in Engineering (CILAMCE)*, 2022.
- [103] A. J. Castrillon Vasquez, L. F. Lozano, and G. Chapiro. The traveling foam wavefront in fractured porous medium. *Submitted*, 2023.
- [104] A. J. Castrillon Vasquez, L. F. Lozano, W. Pereira, J. B. Cedro, and G. Chapiro. The traveling wavefront for foam flow in two-layer porous media. *COMG*, 2022.
- [105] A. J. Castrillon Vasquez, P. Z. S. Paz, and G. Chapiro. On the viscous crossflow during the foam displacement in two-layered porous media. *Submitted*, 2023.
- [106] A. I. Volpert, V. A. Volpert, and V. A. Volpert. *Traveling Wave Solutions of Parabolic Systems*. AMS, Providence, RI, 2000.
- [107] HU Wenrui, WEI Yi, and BAO Jingwei. Development of the theory and technology for low permeability reservoirs in china. *Petroleum Exploration and Development*, 45(4):685–697, 2018.
- [108] Yannis C Yortsos. A theoretical analysis of vertical flow equilibrium. *Transport in Porous Media*, 18(2):107–129, 1995.
- [109] G. Yu, W. R. Rossen, and S. Vincent-Bonnieu. Coreflood study of effect of surfactant concentration on foam generation in porous media. *Industrial & engineering chemistry research*, 58(1):420–427, 2018.
- [110] Vito J Zapata and Larry W Lake. A theoretical analysis of viscous crossflow. In *SPE Annual Technical Conference and Exhibition*, pages 1–11. OnePetro, 1981.
- [111] R. Q. Zavala, L. F. Lozano, P. L. J. Zitha, and G. Chapiro. Analytical solution for the population-balance model describing foam displacement. *Transport in Porous Media*, 144:211–227, 2021.
- [112] Rosmery Q Zavala, Luis F Lozano, and Grigori Chapiro. Traveling wave solutions describing the foam flow in porous media for low surfactant concentration. *Computational Geosciences*, pages 1–18, 2023.
- [113] Z. H. Zhou and W. R. Rossen. Applying fractional-flow theory to foams for diversion in matrix acidization. *SPE Production & Facilities*, 9(01):29–35, 1994.
- [114] Robert Zimmerman and Gudmundur S. Bodvarsson. Hydraulic conductivity of rock fractures. *Transport porous media*, 21(23):1–30, 1996.
- [115] P. L. J. Zitha. A new stochastic bubble population model for foam in porous media. In *SPE/DOE Symposium on Improved Oil Recovery*, pages SPE–98976. Society of Petroleum Engineers, 2006.
- [116] P. L. J. Zitha and D. X. Du. A new stochastic bubble population model for foam flow in porous media. *Transport in Porous Media*, 83(3):603–621, 2010.

- [117] P. L. J. Zitha, Q. P. Nguyen, P. K. Currie, and M. A. Buijse. Coupling of foam drainage and viscous fingering in porous media revealed by x-ray computed tomography. *Transport in Porous Media*, 64(3):301–313, 2006.
- [118] Pacelli LJ Zitha, Quoc P Nguyen, and Peter K Currie. Effect of flow velocity and rock layering on foam flow: an x-ray computed tomography study. In *SPE Asia Pacific Oil and Gas Conference and Exhibition*, pages SPE–80530. SPE, 2003.

APPENDIX A - Effect of permeabilities on the nose size

Figure 54, shows two simulations in FOSSIL using a three-layer domain as Fig 16, considering permeabilities $k_1 = k_3$ and varying k_2 . The upper figure shows $k_1/k_2 = 10$ and the lower figure shows $k_1/k_2 = 20$. We observe that the x-position of the water saturation front increases proportionally to the contrast of permeabilities.

When performing numerical or laboratory experiments, one of the circumstances that most hinders the rapid obtaining of results is the knowledge of the appropriate length of the domain ($x = L$). This is especially important when studying the existence of traveling waves in a domain of the type Fig. 16; since the stable behavior of the wave often occurs beyond the maximum value of L . By determining this result, we can determine the value of L based on the contrast of porosities between the layers, as can see in Fig 55.

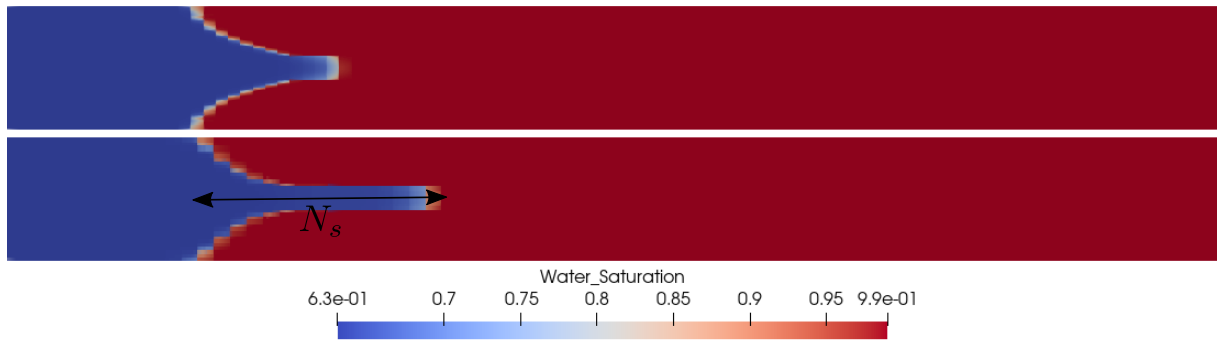


Figure 54 – Nose size (N_s tip of water saturation front) in the most permeable layer, depending on the ratio of permeabilities of each layer.

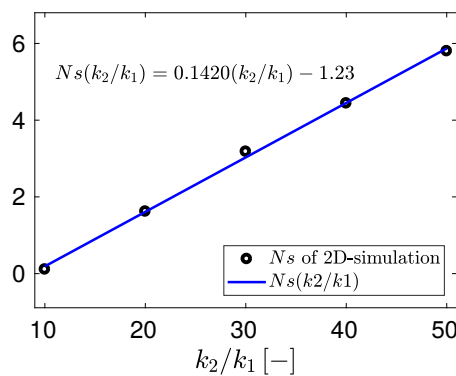


Figure 55 – Nose size N_s (tip of water saturation front) in the most permeable layer, depending on the ratio of permeabilities of each layer.